REPORT DOCUMENTATION PAGE

AFRL-SR-AR-TR-02-

0408

1. REPORT DATE *(DD-MM-YYYY)*	2. REPORT TYPE	3. DATES COVERED *(From - To)*
04/11/2002	Phase I Final Report	30 Sep 2001 - 29 Sep 2002

4. TITLE AND SUBTITLE	5a. CONTRACT NUMBER
Development of High Frequency Numerical Simulation Tools for Electromagnrtic Scattering and Radiation Problems in Frequency and Time Domain	F49620-01-C-0045

5b. GRANT NUMBER

5c. PROGRAM ELEMENT NUMBER

6. AUTHOR(S)	5d. PROJECT NUMBER
Elizabeth H. Bleszynski Marek K. Bleszynski Thomas Jaroszewicz	

5e. TASK NUMBER

5f. WORK UNIT NUMBER

7. PERFORMING ORGANIZATION NAME(S) AND ADDRESS(ES)	8. PERFORMING ORGANIZATION REPORT NUMBER
Monopole Research 739 Calle Sequoia Thousand Oaks, CA 91360	MON-02-19

9. SPONSORING/MONITORING AGENCY NAME(S) AND ADDRESS(ES)	10. SPONSOR/MONITOR'S ACRONYM(S)
Dr. Arje Nachman AFOSR/NM 4015 Wilson Blvd., Ste 800 Arlington, VA 22203	

11. SPONSOR/MONITOR'S REPORT NUMBER(S)

12. DISTRIBUTION/AVAILABILITY STATEMENT

Approved for public release, distribution unlimited

13. SUPPLEMENTARY NOTES

None

20030107 034

14. ABSTRACT

Report developed under STTR contract for topic AF01T009. The main objective of the Phase I effort was to set up a framework for the wavefront (WF) evolution technique and to investigate the feasibility of incorporating, in a fashion consistent with reciprocity, of the edge diffraction effects into the WF approach. A wavefront is defined as a surface on which the propagating fields have a constant phase. Main advantages of the WF evolution approach, compared to the conventional ray tracing, are that (i) it maintains an approximately constant ray-ray spacing, h, even in processes involving multiple reflection and diffraction; this is achieved due to the dynamic adjustment of the number of rays; (ii) it allows for a precise, second order in h, determination of shadow and reflection boundaries; and, (iii) it allows, in a natural way, for the consistent inclusion of multiple diffraction mechanisms and diffraction occuring in combination with reflection processes. In Phase I we initiated the implementation of the geometrical construction of the reflected and diffracted WFs and the corresponding evaluation of the associated fields.

15. SUBJECT TERMS

STTR report	wavefront evolution	multiple edge diffraction
computational electromagnetics	uniform theory of diffraction	
high frequency methods	multiple scattering	

16. SECURITY CLASSIFICATION OF:			17. LIMITATION OF ABSTRACT	18. NUMBER OF PAGES	19a. NAME OF RESPONSIBLE PERSON
a. REPORT	b. ABSTRACT	c. THIS PAGE			Elizabeth H. Bleszynski
unclassified	unclassified	unclassified	unclassified unlimited	47+39	19b. TELEPHONE NUMBER *(Include area code)* (805) 375-0318

Standard Form 298 (Rev. 8/98)
Prescribed by ANSI Std. Z39.18

TABLE OF CONTENTS

1. Summary

The main purpose of the Phase I effort was to set up the general framework for the wavefront (WF) evolution technique and its initial implementation The framework we developed includes algorithms for evolution of WFs and fields associated with them, as well as algorithms for computation of the scattered fields (either directly, or through the prior computation of surface currents). An emphasis was put on incorporating, in a fashion consistent with reciprocity, *edge diffraction effects* into the WF approach. A UTD formulation, modified to reproduce rigorously the canonical solution in the near and transition regions, has been constructed [1] to describe the "non-optical" character of diffracted rays, and to evaluate diffracted fields.

An additional benefit of our development of the WF method is that it will provide an essential element, *a general parametric representation of the Ansatz*, to the *asymptotic high frequency integral equation formulations* [2, 3] based on the stationary point method. In other words, the HF code we plan to construct may, as a byproduct, provide an input, for *a general geometry*, to an asymptotic high-frequency integral equation solver.

Phase I results may form the basis for the further development of an efficient high-frequency scattering code.

2. Development of the WF evolution framework

2.1. Main features of WF propagation approach

In the context of high-frequency asymptotic expansions the WF (or a phasefront) is defined mathematically as a surface on which the considered propagating fields have a constant phase. The set of all WFs forms a one-parameter family of surfaces, characterized by the phase or, equivalently, by the length of the path measured from the wave source. In the following we use the path length as the evolution parameter of the WF.

Most of the recent activity in the development WF evolution techniques occurred in the area of geophysical (seismic) problems [4, 5, 6, 7, 8]. In such application the main interest lies in describing wave propagation through penetrable inhomogeneous media, i.e., in the wave refraction. In electromagnetics, on the other hand, the more relevant phenomena are reflection and diffraction. Correspondingly, our WF evolution algorithms concentrate primarily on these processes.

Wavefront evolution may be considered as an *improved ray-tracing method*, in which the number of rays is *dynamically adjusted*, while the WF expands or shrinks. New rays are also created at shadow and reflection boundaries, and in diffraction processes.

The advantage of the WF evolution approach, compared to the conventional ray tracing, is that it maintains an approximately *constant ray-ray spacing h*, even in processes involving multiple reflection and diffraction; this is achieved due to the dynamic adjustment of the number of rays. In our implementation the WF is represented as a meshed (triangulated) surface with well defined boundaries; consequently, adjustment of the number of rays is realized as mesh simplification or complexification. The new rays maintain a precise WF definition, due to the use of the local second-order curvature-based surface representations.

3

Another advantage of our implementation of the WF evolution algorithms is that they allow a precise, *second order in h determination of shadow and reflection boundaries*; this is also achieved by creating additional rays located precisely at these boundaries.

Probably the most significant benefit of the WF evolution methods is that they allow, in a natural way, for the consistent inclusion of multiple *diffraction mechanisms* and diffraction occurring in combination with reflection processes. As we describe below in more detail, in our Phase I work we initiated the implementation of the geometrical construction of diffracted WFs due to edge diffraction, and the corresponding evaluation, according to the UTD asymptotic expansion, of the fields associated with the diffracted WFs.

Our WF evolution algorithms are currently implemented for scatterers defined by some selected analytically defined surfaces, or by facetized (triangulated) surfaces. They can be, however, extended in a relatively straightforward way to general parametric surfaces, defined, e.g., in terms of bicubic patches. The only new element required for such a generalization is a set of functions providing information on the normals and curvatures of the scatterer surface, and computing intersections of lines with the surface.

We note that our developments are based on the *"Lagrangian"* formulation of the WF theory, in which WF are characterized by geometrical and field parameters associated with a set of vertices ("markers") moving in space with the changing evolution parameter. There have been recent developments in the alternative *"Eulerian"* methods (Refs. [9, 10, 11] and private communications), in which the WF parameters are associated with points of a *fixed spatial grid* (possibly in the higher number of dimensions). These methods have certain advantages in terms of simplicity of formulation, and provide a natural way of defining WF with an approximately constant spatial resolution (equal to the Eulerian grid spacing). The latter feature, however, may become a hindrance in describing the WF behavior near caustics, because the Eulerian formulation naturally provides only storage for a limited amount of information per unit volume. Therefore, situations where rays converge require special treatments, such as using higher dimensions or "extension" in the evolution parameter. We note that the WF behavior near caustics is also relevant in describing diffraction, since diffraction sources are always caustics of the diffracted WF.

It should be noted that neither Lagrangian nor Eulerian formulations provide, *per se*, any new physical mechanism or any new mathematical apparatus for describing GO evolution or diffraction of waves. These processes have to modeled, in both approaches, using the asymptotic high frequency methods. Also, geometrical problems associated with the field propagation, such as detection of a scatterer or identification diffraction sources on the scatterer, have to be resolved independently of the use of a Lagrangian or an Eulerian approach.

For all the reasons listed above we decided to stay, in our developments, with the more conventional Lagrangian formulation; we present its details below.

4

2.2. WF propagation

We implement the notion of a WF as a collection of points (vertices) forming a well-defined triangulated surface, specified by a mesh (a set of faces). With each vertex $\mathbf{r}$ we associate a ray, which carries with itself information on the main curvature values $\kappa_1 = 1/\rho_1$ and $\kappa_2 = 1/\rho_2$ and on a triad of vectors: the normal $\mathbf{n}$ to the WF, and the directions $\mathbf{a}_1$ and $\mathbf{a}_2$ of the main curvatures. Thus, each vertex on the WF provides a local definition of a second-order surface (Fig. 1).
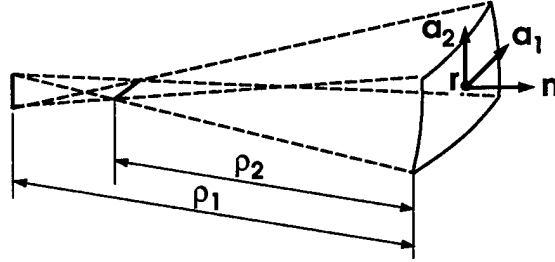
Fig. 1: A local quadratic surface representation associated with a ray.

The crucial element of our WF implementation is that the number of vertices (rays) on the WF is not fixed, but may change during its evolution, i.e., some rays may be removed and some new rays created. The essence of the algorithm is that the ray-ray distances are kept in a certain range $[h_{\min}, h_{\max}]$, controlled by two parameters: a fixed default ray-ray spacing h_0 and a local WF mean curvature radius (defined as $\rho = 2/(|\kappa_1| + |\kappa_2|)$). Using these parameters, our evolution algorithm defines, at each point of the WF, minimum and maximum values of the ray-ray spacing as

$$h_{\min} = \gamma^{-1} \min\{h_0, \beta^{-1}\rho\} \, , \tag{2.1a}$$

$$h_{\max} = \gamma \quad \min\{h_0, \beta^{-1}\rho\} \, , \tag{2.1b}$$

where $\beta \gtrsim 1$ and $\gamma \gtrsim 1$ are constants.[1] Eqs. (2.1) imply that, as long as the curvature radius ρ is not too small compared to h_0 ($\rho \geq \beta h_0$), the range of the ray-ray distances is determined by the parameter h_0; whereas for smaller curvature radii, the required values of ray-ray spacing are reduced to values proportional to ρ. This prescription helps to maintain a sufficient resolution when the WF shrinks in the neighborhood of caustics. The value of the default resolution h_0 should be determined on the basis of the scale of the geometrical details of the scattering object.

As the two mesh modification mechanisms that allow us to maintain the required ray-ray spacing we use the well-known *edge contraction* and *edge splitting* algorithms (Figs. 2a and 2b); these operations enable us to realize *mesh simplification* and *mesh "complexification"* operations. Similar operations (and particularly mesh simplification) have been much studied and are well known in computer graphics. However, our algorithm differs from those methods in one important aspect: in creating new rays (vertices) we are using information on the local *second-order surfaces* associated with the existing rays. This enables us to maintain accuracy in the WF definition of the *second*

---

[1] In the current implementation we take $\beta = 4$ and $\gamma = 2$.

order in the ray-ray spacing. Another difference between our mesh simplification/complexification algorithm and those algorithms commonly used in computer graphics is that, at each contraction or splitting step, we sort the edges according tho their lengths and apply contraction/splitting to the currently shortest/longest edge. This prescription contributes greatly to the good quality of the generated meshes (favorable aspect ratios of the triangles).
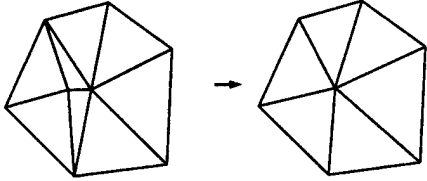
Fig. 2a: Contraction of a short edge to a single vertex in a WF mesh.
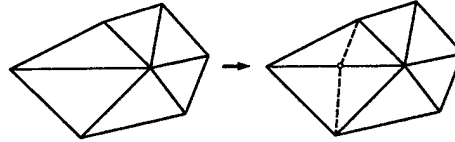
Fig. 2b: Splitting of a long edge in a WF mesh.

As an example, we show in Fig. 3 the free-space evolution of a hemispherical WF, of initial radius $R_0 = 1$, discretized with the resolution $h_0 = 0.1$. The WF first shrinks, and then expands, with the evolution step 0.3 (in the length units). Three stages are shown: step 0 (the initial shrinking WF), with the radius 1.0 and 931 rays; step 4 (just after the beginning of the expansion), with the radius 0.2 and 241 rays; and step 20, with the radius 5.0 and 12,213 rays. A visual inspection of Fig. 3 suggests that a good quality of the mesh defining the WFs is maintained in spite of the wide range of variation in the number of rays.

A more quantitative assessment of the algorithm accuracy is presented in Figs. 4 and 5, where deviations of the WFs from the ideal spherical shape are shown, as r.m.s. errors. Fig. 4 shows that, in the later evolution steps, the errors remain practically constant. They also decrease with the decreasing resolution h_0, although slower than proportionally to h_0^2. The latter feature is due to some loss of accuracy associated with the WF shrinkage and the decrease in the number of rays. In a steady WF expansion, however, the error is, in fact, of the order $O(h_0^2)$. This is demonstrated in Fig. 5, where we plot and the r.m.s. error in the surface definition for a hemispherical WF expanding in 13 steps from the radius 1.0 to the radius 4.9. Fig. 5 shows, in particular, that with decreasing the resolution h_0 by the factor of 2, the error in WF definition decreases approximately by the factor of 4.
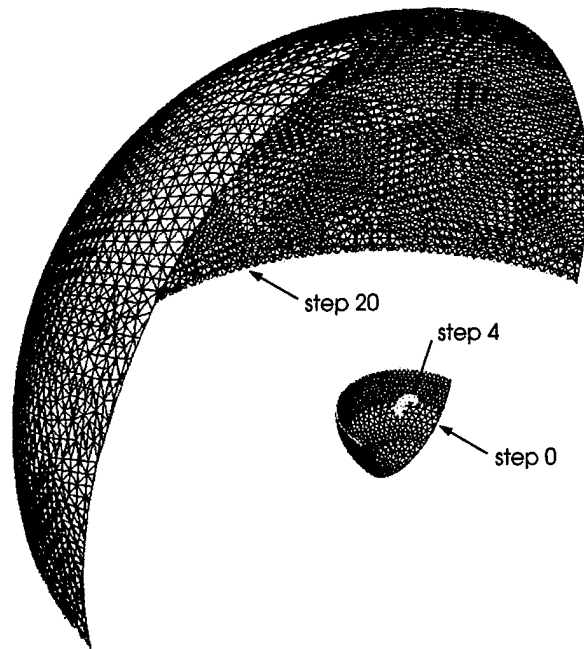
Fig. 3: Propagation of a hemispherical WF, first shrinking (steps 0 – 3) and then expanding (steps 4 – 20). For clarity, only halves of the hemispherical surfaces are shown.
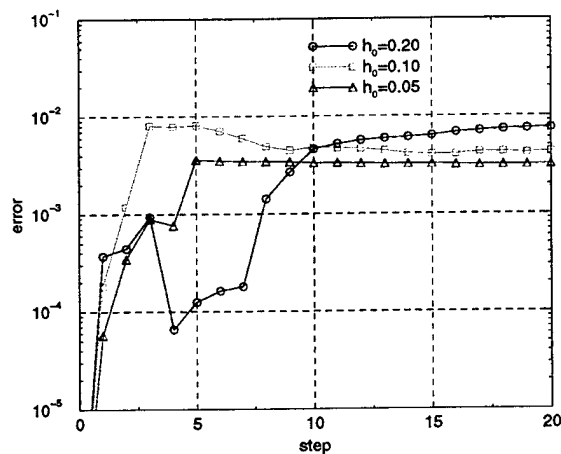
Fig. 4: R.m.s. error in the WF surface as a function of the evolution step for a shrinking and subsequently expanding WF, for three resolutions $h_0 = 0.2, 0.1, 0.05$.
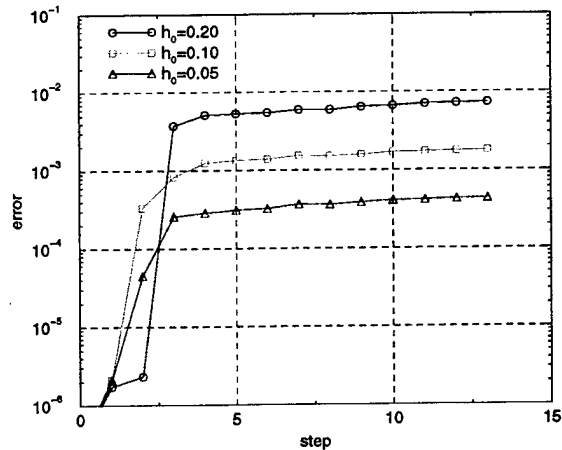
Fig. 5: R.m.s. error in the WF surface as a function of the evolution step, for a steadily expanding WF, for three resolutions $h_0 = 0.2, 0.1, 0.05$.

The results shown above indicate that we are able to change, in a wide range, the number of rays in contracting and expanding WFs while keeping WF definition errors under control. Such a precise interpolation of WF surfaces is possible only because in mesh simplification and complexification steps we are using information on the local second-order surfaces associated with rays.

We stress that, as already suggested by the results of Figs3 and 4, our WF discretization criteria allow for WFs passing through caustics with virtually no loss of accuracy.

A similar example (Fig. 6) shows an ellipsoidal WF shrinking and then expanding, and assuming intermediate shapes of "swallow-tail" type.
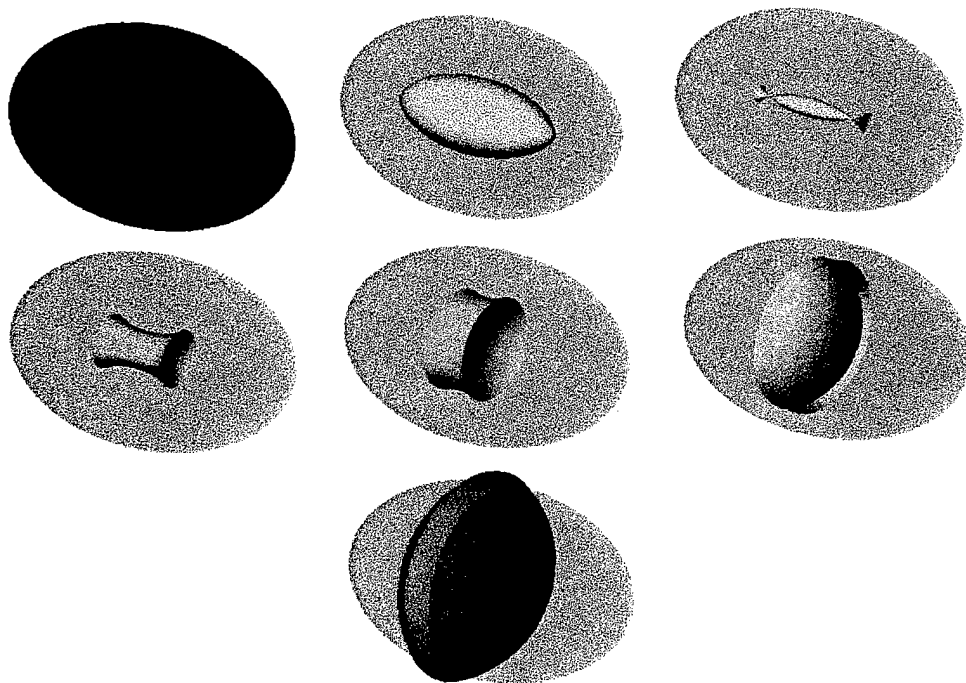
Fig. 6: Evolution of a WF of ellipsoidal shape, first shrinking and then expanding, showing creation of "swallow-tail" shapes. (The semitransparent ellipsoid in every evolution step shows the initial WF.)

2.3. WF reflection processes

We first describe our WF reflection algorithm for *smooth scatterer surfaces*. In this case the WF is generally a non-smooth surface, i.e., the tangentials to the WF may be discontinuous. However, the WF remains *connected*, and does not separate into disjoint components.

We consider reflection of an incident WF ϕ on an obstacle formed by a closed smooth surface S, as visualized in Figs. 7a and 7b. In this configuration the initial WF ϕ, shown in Fig. 7a as the dashed line, approaches the scatterer's surface.
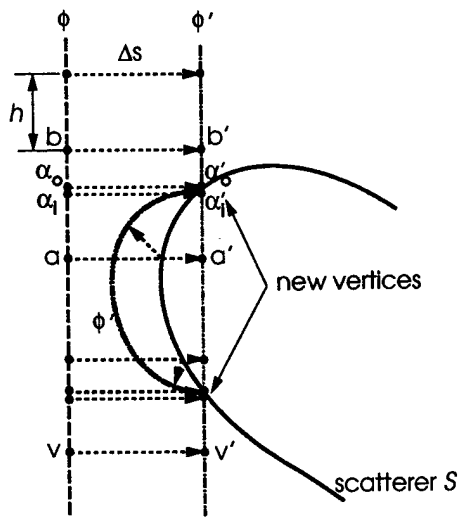
Fig. 7a: A schematic representation of one evolution step of a WF ϕ reflecting off a closed impenetrable surface S, and forming a new WF ϕ'.
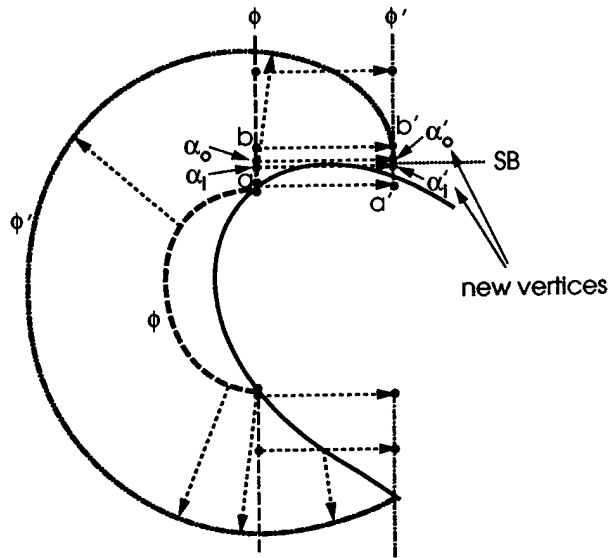
Fig. 7b: A schematic representation of an evolution step following that shown in Fig. 7a. SB stands for the shadow boundary.

The steps of the algorithm for the WF evolution are then as follows:

1. We initially evolve the WF *ignoring the scatterer*, i.e., we move each vertex v on the WF ϕ by the distance Δs in the direction normal to the WF surface.

2. We then examine all vertices v' on the evolved WF, and classify them into "inner" and "outer" ones: inner vertices v' are such that the ray segment $(v\,v')$ intersects the surface, and outer vertices are the remaining ones. In Fig. 7a we marked inner vertices with red dots, and outer vertices with black dots.

3. Next, we examine all edges of the evolved WF. If an edge connects an inner vertex and an outer vertex, such as the vertices a' and b' in Fig. 7a, we find, by performing a binary search, the point where it intersects the surface S. At this point of the edge we create *two new vertices*, an "inner" and an "outer" one. Such vertices in Fig. 7a are α'_i and α'_o. They share the same spatial location, but will follow different evolution paths.

4. We examine in turn all faces (triangles) of the evolved WF mesh, and process *"divided" faces*, i.e., those faces whose some vertices are inner and others are outer. An example of such a face is shown in Fig. 8. We partition such a face into a triangle (an outer triangle in Fig. 8) and a quadrilateral, and split further the quadrilateral into two triangles.

5. Finally, we reprocess all the inner vertices (the original evolved vertices and the new ones). We evolve them back to the original WF ϕ, and evolve them again forward *in the presence of the scatterer*, i.e., taking reflections into account. In this way the inner vertices form a part of the reflected WF ϕ' (the red dash-dotted line in Fig. 7a), while the previously found outer vertices form the forward-propagating part of the WF ϕ' (the black dash-dotted line in Fig. 7).

9
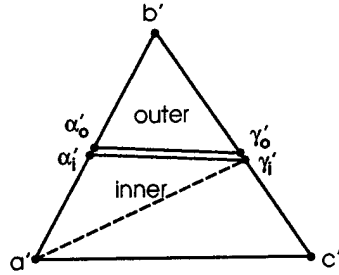
Fig. 8: Partition of a WF face having two inner vertices (a' and c') and one outer vertex (b').

We stress an important element of our algorithm: The mesh faces such as shown in Fig. 8 are divided into parts belonging to the forward-propagating and reflected segments of the WF. The algorithm is able to locate the division points (new vertices α_i', α_o', γ_i', and γ_o' in Fig. 8) with an *arbitrary accuracy*, unrelated to the ray-ray spacing h. Therefore, the location rays on the boundary between the forward-propagating and reflected parts of the WF can be considered *exact*; the only approximation made is the considered boundary consists of straight line segments, rather than curved lines. For typical segment length of order h_0, the resulting error is $O(h_0^2/R)$, where R is the curvature radius of the surface S.

The algorithm described above can be generalized to scatterers formed by non-smooth surfaces, both closed and open. The generalization is, however, somewhat more involved, for two main reasons:

(i) the WF usually separates into several disconnected pieces; and

(ii) in general, it is necessary to consider more complex cases of the scatterer surface intersecting the WF mesh; in particular, triangles forming the WF mesh may be intersected in ways more complicated than that shown in Fig. 7 (in the analysis of smooth surfaces we assumed that the surface's radii of curvature R were much larger than the ray-ray spacing h).

If we attempt to reproduce GO shadow and reflection boundaries with an arbitrary accuracy, the second of these problems causes a significant complication of the algorithm. Therefore, at the present stage of the algorithm development, we concentrated on the first problem, that is, splitting of the WF due to reflection on "sharp" edges of the scatterer.

We give below a brief description of the WF reflection algorithm for a practically important case of a scatterer with a facetized (typically triangulated) surface representation. We consider a scatterer whose part is represented schematically in Fig. 9. The initial incident WF, denoted by ϕ, approaches a wedge-type element of the scatterer surface S. The edge of the wedge shown in the figure is assumed to be "sharp", i.e., the angle between the normals to the faces exceeds some predefined, critical angle θ_0.

As before, we first evolve the rays associated with the WF ϕ as if the scatterer were absent; subsequently, we examine intersections of rays with the scatterer surface, and then create some additional rays, and reflect ray segments penetrating the scatterer surface.
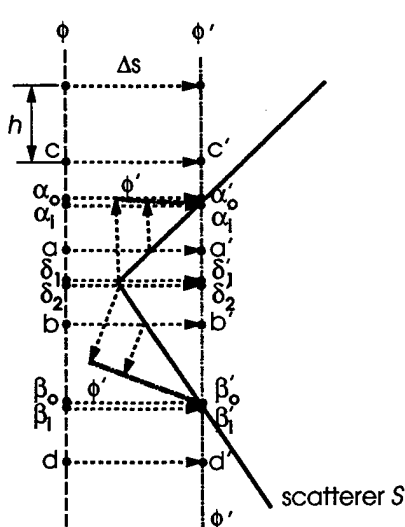
Fig. 9a: A schematic representation of one evolution step of a WF ϕ reflecting off a non-smooth impenetrable surface S, and forming a new WF ϕ'.
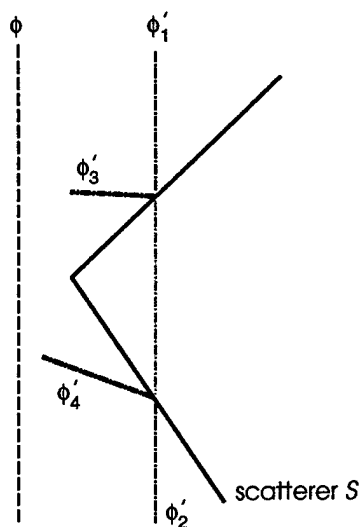
Fig. 9b: The same WF configuration as in Fig. 9a, with the rays and vertices removed for clarity.

More specifically, the main steps of the algorithm are as follows:

1. We evolve the WF *ignoring the scatterer*, i.e., we move each vertex on the WF ϕ by the distance Δs in the direction normal to the WF surface; thus the vertices $a, b, \ldots$ become $a', b', \ldots$.

2. We locate sharp edges on the surface S – in our example the tip of the wedge. This task is carried out as follows:

   2.1. For each ray segment intersecting the surface S we find the normal to the surface at the intersection point.

   2.2. For each edge on the WF mesh we compare normals at the two ends. For example, for the original WF mesh edge $(a\,b)$ we compare the normals at points where the ray segments $(a\,a')$ and $(b\,b')$ intersect S.

   2.3. If the angle between the normals at the end vertices of an edge exceeds the critical angle, we examine the edge in more detail: we subdivide it in a binary fashion until we find two ray segments intersecting the surface S very near the edge (this can be done with any predefined accuracy). In Fig. 9 these rays are $(\delta_1\,\delta_1')$, and $(\delta_2\,\delta_2')$.

3. As in the previous algorithm, we identify then pairs of rays with end slightly outside and slightly inside the scatterer (again with some predefined accuracy). Such ray pairs in Fig. 9 are $\{(\alpha_1\,\alpha_1'), (\alpha_2\,\alpha_2')\}$ and $\{(\beta_1\,\beta_1'), (\beta_2\,\beta_2')\}$.

4. We split (partition) faces whose edges contain the additional vertices associated with ray segments created in the previous step.

5. Finally, as before, we reflect the rays which have penetrated the scatterer surface S.

In the example illustrated in Figs. 9 the resulting reflected WF consists of several segments (Fig. 9b): the parts ϕ_1' and ϕ_2' of the incident WF which have not yet reached the scatterer's

surface, and the parts ϕ_3' and ϕ_4' which have been reflected from the two facets forming the wedge. Reflection on a surface with an edge creates thus a "hole" in the WF, unlike reflection on a smooth surface (Figs. 7a and 7b), where the WF remains a connected surface. (We note that, as we will see, such "holes" are filled in by WF due to diffraction.)

As an example of WF evolution in the presence of smooth scatterers, we consider a process of multiple reflection on a system of two spheres, S_1 and S_2 (Fig. 10). The radii of the spheres are equal 1, and the wavefront resolution is $h_0 = 0.1$. The initial planar wavefront travels upward at at angle of approximately 45°. The consecutive evolution steps show reflections from the first, second, and again from the first sphere.
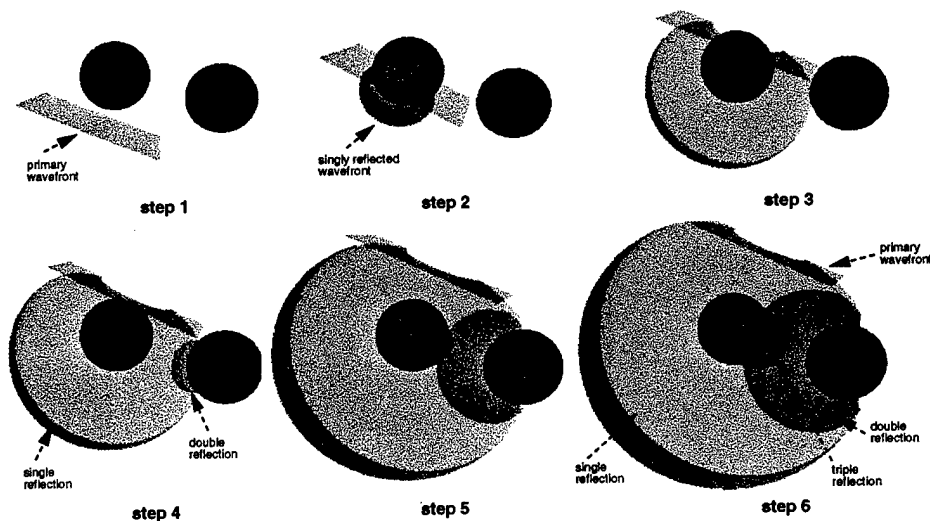
Fig. 10: Reflection of a planar WF on a system of two spheres.

In Fig. 11a we show an evolution stage for the same system of two spheres arrived at after several reflections. (In this example, the initial planar wavefront travels downward in the vertical direction.)
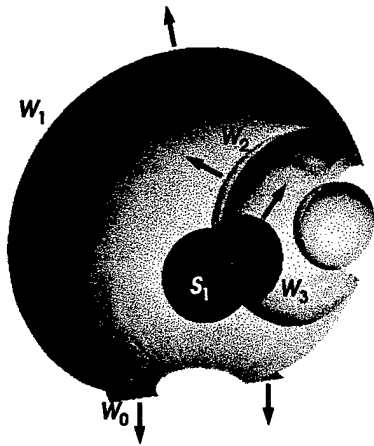
Fig. 11a: Reflection of a planar WF on a system of two spheres, for the resolution $h_0 = 0.1$, and the number of rays increasing from 1,681 to 22,962. Various colors show the parts of the WF $W_0, \dots, W_3$ due to 0, 1, 2, and 3 reflections.
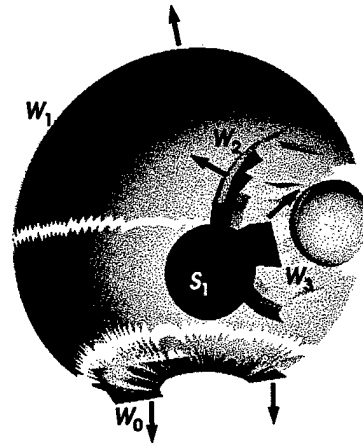
Fig. 11b: The same final WF as shown in Fig. 11a, but obtained using the conventional ray-tracing algorithm with a *much higher resolution* $h_0 = 0.02$ and a fixed number of rays 40,401.

Parts of the wavefront due to 0, 1, 2, and 3 reflections are shown in various colors. All these wavefront parts are equally well defined, due to the dynamical ray number adjustment. In the considered process of wavefront scattering and expansion the number of rays increases from $N = 1,681$ to $N = 22,962$.

For comparison, we show in Fig. 11b the analogous final wavefront constructed using the conventional ray-tracing algorithm with a much higher resolution, $h_0 = 0.02$, and the corresponding fixed number of rays $N_{RT} = 40,401$. This Figure clearly shows the rapid deterioration of the wavefront definition with the increasing reflection order and the associated wavefront expansion. In particular, the last wavefront W_3, due to triple reflection, is barely existent. The comparison indicates that, due to the dynamic ray number adjustment, our wavefront evolution algorithm provides a much *superior resolution* at all reflection orders with an overall *much smaller number of rays*.

2.4. WF edge diffraction processes

We describe now our WF algorithm for edge diffraction processes. While the algorithm is already complete, we are currently in the process of its numerical implementation, and thus the results presented here are preliminary.

The geometrical construction of edge diffracted WFs is based on the original Geometrical Theory of Diffraction (GTD) [12, 13], which in turn follows from the generalized Fermat's principle, and ultimately from the stationary-point asymptotics of the high-frequency scattering processes. The associated field amplitudes, however, are computed using the Uniform Geometrical Theory of Diffraction (UTD) [14, 15].

The main steps of the algorithm for construction of edge-diffracted WFs are as follows:

1. Identify scatterer edges constituting source of diffraction (we refer to these as "diffraction edges").

13

2. Generate diffracted rays emanating from the diffraction edges.

3. Assign WF curvature parameters and field values to the created diffracted rays.

4. Construct triangulation mesh (connectivity) for the diffracted rays.

Although the above steps may seem straightforward, their implementation is rather complex. We discuss them now in turn.

Step 1 requires implementing an algorithm with elements of the previously discussed procedures for (1) detecting "sharp edges" (in the context of WF splitting associated with reflection), and (2) detecting the shadow boundary (described in the context of the smooth-surface reflection algorithm). If the edge-diffraction algorithm is applied to a facetized scatterer surface, we assume that the "sharp edges" are sources of diffraction, while "smooth edges" have to the treated by a separate algorithm for smooth-surface diffraction.

An important element of the algorithm is that the identified "diffraction edges" are associated with and accessed through the *WF mesh edges*. As indicated in Fig. 12, new rays ($\alpha_1, \alpha_2, \dots$) hitting the sharp edge E on the scatterer emerge from the edges of the WF mesh ($e_1, e_2, \dots$). Indeed, these rays are created by interpolating rays at end vertices of the WF edges.
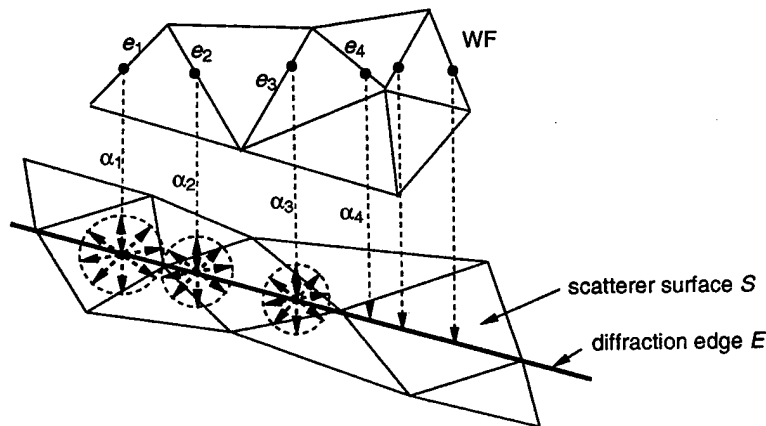
Fig. 12: A schematic view of the procedure of generating diffracted rays emerging from the points of a diffraction edge E hit by newly created rays $\alpha_1, \alpha_2, \dots$.

Step 2 is performed in a loop through the edges e of the WF. From some of these edges there emerges a pair of new rays α, terminating at a diffraction edge. At the termination point we create a set of new rays (of length equal to the evolution step decreased by the length of the ray segments α), on the surface of a cone (the "Keller cone"), whose axis is the diffraction edge (Fig. 12). The number of diffracted rays is fixed, and is determined on the basis of the required WF resolution (this element of the algorithm is not critical, since the number of rays will adjust itself during the subsequent evolution of the diffracted WF).

Finally, **step 3** is executed as a loop over the faces F of the WF. We consider here such faces F from two edges of which emerge new rays α (Fig. 13a.) Through these rays we access two consecutive sets of diffracted rays, and create edges connecting the corresponding rays in the two sets, forming a surface consisting of quadrilateral facets. By triangulating that surface (Fig. 13b), we arrive at a meshed diffracted WF.

14
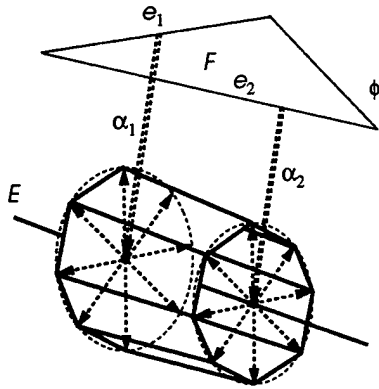
Fig. 13a: Building connectivity for the diffracted rays.
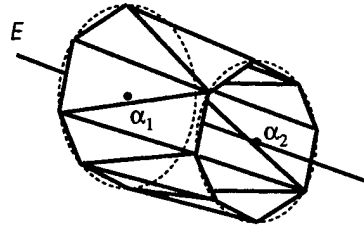
Fig. 13b: Triangulation of the diffracted WF.

The overall picture of the newly created diffracted WF may be as shown in Fig. 14. In this Figure a plane WF ϕ is approaching a smooth edge of a screen S, moving in a direction nearly tangential to the screen plane. As the incident WF advances to the position ϕ', it generates a reflected WF (not shown), and a diffracted WF, according to the algorithm described above.
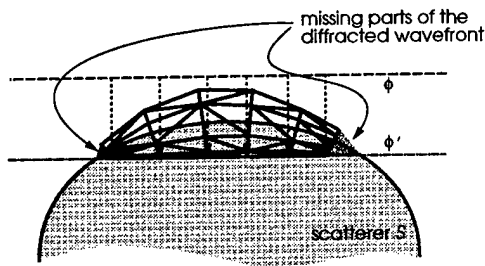
Fig. 14a: A schematic view of a new diffracted WF generated along a smooth edge of a screen S by a plane WF incident nearly tangentially to the screen.
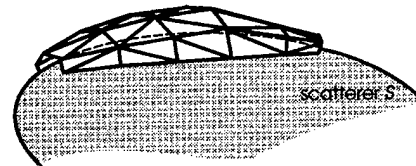
Fig. 14b: A perspective view of the diffracted WF shown in Fig. 14a.

We note that the diffracted WF algorithm, as described above, may not reproduce correctly the end (cone-shaped) parts of the new WF; this effect is indicated in Fig. 15, which shows the actual process of diffracted WF creation, as modeled by our code. The reason for this deficiency is that we use only WF *edges* to detect WF intersections with diffraction edges. In other words, the pairs of new rays α, terminating at the diffraction edge E, may emerge only from the WF edges e. This feature of our procedure affects also the GO reflection algorithm, where some parts of the reflected WF may be missing. In both cases the defects in the WFs are only due to the present implementation of the algorithm, and will be corrected as the algorithm is further refined.

15
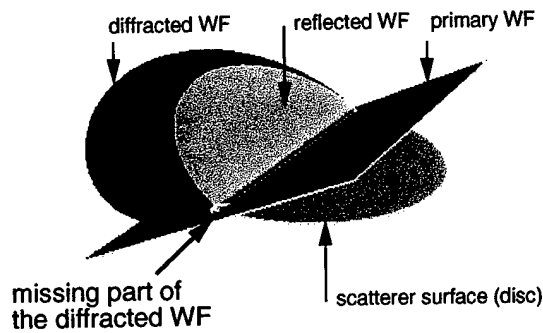
Fig. 15: A defect of the created WF – a missing end of the cone-shaped WF part, pointed to by the arrow.
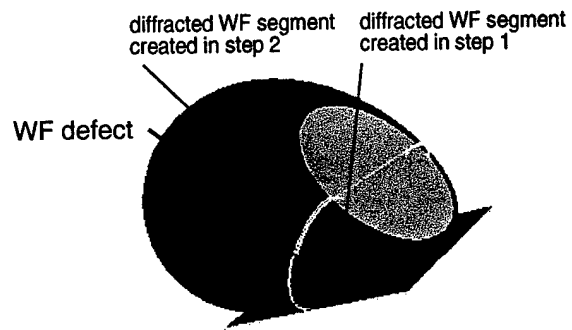
Fig. 16: A gap between the diffracted WF segments created in two consecutive evolution steps.

Another, related, defect in the present algorithm for diffracted WF creation manifests itself in gaps between the segments of the diffracted WF generated in consecutive evolution steps. A situation of this type is shown for diffraction on a disc in Fig. 16. These deficiencies can be corrected by extending the "memory" of the algorithm, i.e., increasing the amount of information preserved from one to the next evolution step.

The present version of our code includes only edge diffraction as an asymptotic expansion scattering mechanism of order $1/\sqrt{k}$. Another diffraction mechanism not implemented in the current version of our code is diffraction from corners, inevitably arising for diffraction edges consisting of straight line segments. As an example, we show in Fig. 17 several steps of creating diffracted WFs due to a plane WF incident on a rectangular plate. The WF diffracted on the individual edges of the plate form either cylinders of cut-off cones. These WFs should be connected by the four spherical WFs due to diffraction on the four corners of the plate.
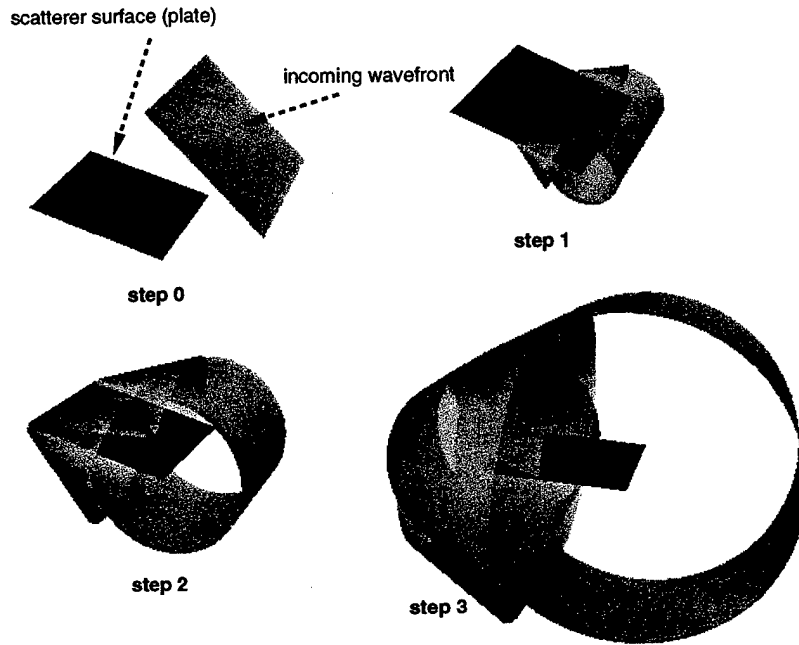
Fig. 17: Three evolution steps in creating diffracted WFs due to a plane WF incident on a rectangular plate. For clarity, the primary and reflected WFs are not shown in evolution steps other than the initial configuration ("step 0").

3. Field computation

3.1. Behavior of edge diffracted fields

The final outcome of the WF algorithm should be in the form of the observable quantities – typically the scattered fields, and the related scattering cross-section. Various approaches to this goal are possible, and we consider two of them:

1. The scattered fields can be determined directly from the fields associated with the sufficiently evolved WFs, i.e. WFs leaving the scattering region.

Alternatively,

2. The scattered fields can be computed as Kirchhoff integrals of the currents induced on the scatterer surface (more generally, effective currents on an appropriately defined aperture).

The two approaches are equivalent, provided all terms to the given order in $1/k$ in the asymptotic expansion are consistently taken into account, both in computation of the currents and computation of the field. In both cases we utilize fields associated with rays constituting WFs. In particular, the second approach requires the electric induced current

$$\mathbf{J} = -2\mathbf{n} \times \Delta\mathbf{H} , \qquad (3.1)$$

17

where $\Delta \mathbf{H}$ is the discontinuity of the magnetic field across the scatterer surface, and $\mathbf{n}$ is the normal to the surface. Because of this fact, we find it more convenient to use the magnetic rather than electric field as the basic field associated with rays.

Thus, to each point of a WF we ascribe a magnetic field value $\mathbf{H}$; a field value is also associated with every point on a ray connecting two consecutive WFs. For a WF propagating in free space, knowing the field value $\mathbf{H}(s_0)$ at a certain evolution parameter s_0, we can obtain (according to the laws of GO) the field value $\mathbf{H}(s)$ at another value s of the evolution parameter as

$$\widetilde{\mathbf{H}}(s) = \sqrt{\frac{\rho_1 \, \rho_2}{(\rho_1 + s - s_0)\,(\rho_2 + s - s_0)}} \; \widetilde{\mathbf{H}}(s_0) \,, \tag{3.2}$$

where the curvature radii ρ_i refer to the WF at the reference evolution parameter s_0. Here the fields $\widetilde{\mathbf{H}}$ are defined so as to exclude the common phase factor $\exp(iks)$ associated with the evolution parameter s.

When creating new rays due to mesh complexification or simplification, we associate with them field values obtained by interpolation of the field values of the neighboring rays. In the present implementation, when creating new ray in edge contraction (Fig. 2a) or edge splitting (Fig. 2b) we use simple linear interpolation of field values between the end vertices of the considered edge.

When creating diffracted rays, we ascribe to them fields calculated according to UTD [14, 15], or rather to its modification [1], which we present below. Our modification of UTD was originally motivated by the need of calculating induced currents near the diffraction sources (edges); we thus refer to it as *nUTD*, or the *"near-field UTD"*. We also discuss it mostly in the context of currents, although similar considerations apply to the general problem of field computation.

It is important to stress that, in the "transition regions" (i.e. near the diffraction source and near the optical shadow and reflection boundaries), the fields provided by UTD or nUTD are *not ray-optical*, i.e., they do not evolve according to Eq. (3.2), but are given by more complex expressions involving appropriate transition functions. Only at large distances from the diffraction source, and outside the transition regions, do they reduce to ray-optical fields of GTD.

During Phase I, we addressed the problem of modifying fields near the diffraction sources only for diffraction on a flat polygonal screen with straight edges, illuminated with a plane wave. Near the edges of a polygonal screen, the fields are given, asymptotically, by the solution of the corresponding canonical problem – in this case, a half-plane. Hence, we first examine the behavior of the fields and currents obtained form the exact half-plane solution. Then, assuming the exact half plane solution for the field diffracted by the edges of the screen, we compute the current induced on the screen.

Behavior of the fields and currents near diffraction edges

Consider a half-plane defined by $0 \le x < \infty$, $y = 0$, $-\infty < z < \infty$ (Fig. 18). We assume an incident plane wave with the wave vector

$$\mathbf{k}_{\mathrm{i}} = -k \, (\sin \beta_0 \, \cos \phi_0 \, \hat{\mathbf{x}} + \sin \beta_0 \, \sin \phi_0 \, \hat{\mathbf{y}} + \cos \beta_0 \, \hat{\mathbf{z}}) \tag{3.3}$$

(incidence normal to the edge would correspond to $\beta_0 = \pi/2$).

18
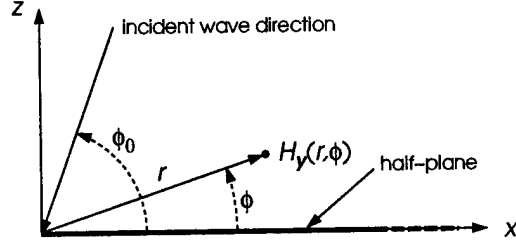
Fig. 18: The half-plane geometry and the field configuration for the "H-polarization" problem.

The exact solution for the canonical problem is well known (see, e.g., Ref. 16]). The Maxwell equations separate in this case into independent Helmholtz equations for the z-components of the electric and magnetic fields, with appropriate boundary conditions.

We first consider the "H-polarization" problem for the magnetic field H_z (the component along the edge of the half-plane). The solution contains the incident, reflected, and diffracted fields, the latter being

$$H_z^{\mathrm{d}}(\rho, \phi) = -e^{i\pi/4}\, e^{ik\rho/\sin\beta_0}\, \frac{\sqrt{\sin\beta_0}}{2\sqrt{2\pi k\rho}}\, \left\{ \sec\frac{\phi-\phi_0}{2}\, F\left(2\,k\rho\,\sin\beta_0\,\cos^2\frac{\phi-\phi_0}{2}\right) \right.$$
$$\left. + \sec\frac{\phi+\phi_0}{2}\, F\left(2\,k\rho\,\sin\beta_0\,\cos^2\frac{\phi+\phi_0}{2}\right) \right\}\, H_z^{\mathrm{i}}\, ,$$

$$(3.4)$$

where the function F, related to the Fresnel integral,

$$F(x) = -2i\,\sqrt{x}\,e^{-ix}\int\limits_{\sqrt{x}}^{\infty} dt\, e^{it^2}\, ,$$

$$(3.5)$$

is normalized so that

$$F(x) \propto 1 - \frac{i}{2x} + \cdots \quad \text{for } x \to \infty\, ,$$

$$(3.6)$$

and

$$F(x) = \left[\sqrt{\pi x} - 2\,x\,e^{-i\pi/4} + \cdots\right] e^{-i(x+\pi/4)} \quad \text{for } x \to 0\, ,$$

$$(3.7)$$

and satisfies the relation

$$F'(x) = i + \left(\frac{1}{2x} - i\right) F(x)\, .$$

$$(3.8)$$

The discontinuity of the magnetic field across the screen is then

$$\Delta H_z^{\mathrm{d}}(\rho) = H_z^{\mathrm{d}}(\rho, 0) - H_z^{\mathrm{d}}(\rho, 2\pi)$$
$$= -e^{i\pi/4}\, e^{ik\rho/\sin\beta_0}\, \frac{2\sqrt{\sin\beta_0}}{\sqrt{2\pi k\rho}}\, \sec\frac{\phi_0}{2}\, F\left(2\,k\rho\,\sin\beta_0\,\cos^2\frac{\phi_0}{2}\right)\, ,$$

$$(3.9)$$

and, according to Eq.(3.1) (with $\mathbf{n} = \hat{\mathbf{y}}$), the electric current due to diffraction is

$$J_x^d(\rho) = -2\,\Delta H_z^d(\rho)\ .\tag{3.10}$$

As follows from Eq.(3.6), for large distances from the edge (i.e., $k\rho\,\cos^2(\phi_0/2) \gg 1$), the current behaves like $\mathrm{const}/\sqrt{k\rho}$, which is a reflection of the cylindrical-wave nature of the diffracted fields. Near the edge, on the other hand, Eq.(3.7) implies that $J_x^d(\rho)$ tends to a constant, which, actually, cancels the PO contribution from the current terms $J_x^i(\rho)$ and $J_x^r(\rho)$ due to the incident and reflected waves. A more detailed analysis (using the expansion (3.7) for $x \to 0$) shows that the total current exhibits the correct edge behavior, $J_x(\rho) \sim \sqrt{\rho}$ for $\rho \to 0$.

Similar analysis applies to the "E-polarization" problem, in which the z-component of the diffracted electric is

$$E_z^d(\rho, \phi) = -e^{i\pi/4}\,e^{ik\rho/\sin\beta_0}\,\frac{\sqrt{\sin\beta_0}}{2\sqrt{2\pi k\rho}}\left\{\sec\frac{\phi - \phi_0}{2}\,F\left(2\,k\rho\,\sin\beta_0\,\cos^2\frac{\phi - \phi_0}{2}\right)\right.$$
$$\left. - \sec\frac{\phi + \phi_0}{2}\,F\left(2\,k\rho\,\sin\beta_0\,\cos^2\frac{\phi + \phi_0}{2}\right)\right\}E_z^i\ .$$

$$\tag{3.11}$$

Here, after calculating the magnetic field and its discontinuity, we find that the total current (now directed along the z-axis) is $J_z(\rho) \sim 1/\sqrt{\rho}$ for $r \to 0$, again in agreement with the expected edge behavior.

Behavior of conventional UTD fields and currents near diffraction edges

Having established the behavior of the exact solution for the canonical problem, we can now compare them with the fields predicted by UTD [14] (converted to our conventions, and specialized to the case of a screen with a straight edge illuminated by a plane wave). As we will see, these expressions will require some *modification of the conventional UTD formulation* in order to correctly reproduce fields and currents in the vicinity of the diffraction edge.

To specify the UTD diffraction coefficients, we first have to define the relevant geometrical quantities. Thus, in the reference system of Fig. 18, the edge direction is

$$\hat{\mathbf{e}} = \hat{\mathbf{z}}\tag{3.12}$$

and the directions of the incident and diffracted rays are given by

$$\hat{\mathbf{s}}^i = -\sin\beta_0\,\cos\phi_0\,\hat{\mathbf{x}} - \sin\beta_0\,\sin\phi_0\,\hat{\mathbf{y}} - \cos\beta_0\,\hat{\mathbf{z}}\ ,\quad \hat{\mathbf{s}}^d = \sin\beta\,\cos\phi\,\hat{\mathbf{x}} + \sin\beta\,\sin\phi\,\hat{\mathbf{y}} - \cos\beta\,\hat{\mathbf{z}}\ ,$$
$$\tag{3.13}$$

where the diffracted ray is required to lie on the diffraction cone, i.e., $\hat{\mathbf{e}} \cdot \hat{\mathbf{s}}^d = \hat{\mathbf{e}} \cdot \hat{\mathbf{s}}^i$, or $\beta = \beta_0$. These two vectors and the vector $\hat{\mathbf{e}}$ define two planes: the *edge-fixed plane of incidence* $(\hat{\mathbf{e}}, \hat{\mathbf{s}}^i)$, and

the *edge-fixed plane of diffraction* $(\hat{\mathbf{e}}, \hat{\mathbf{s}}^d)$. The unit directional vectors associated with the angles ϕ_0, ϕ, β_0, and β are then

$$\hat{\boldsymbol{\phi}}_0 = -\sin\phi_0\,\hat{\mathbf{x}} + \cos\phi_0\,\hat{\mathbf{y}}\;, \tag{3.14a}$$

$$\hat{\boldsymbol{\phi}} = -\sin\phi\,\hat{\mathbf{x}} + \cos\phi\,\hat{\mathbf{y}}\;, \tag{3.14b}$$

$$\hat{\boldsymbol{\beta}}_0 = \cos\beta_0\,\cos\phi_0\,\hat{\mathbf{x}} + \cos\beta_0\,\sin\phi_0\,\hat{\mathbf{y}} - \sin\beta_0\,\hat{\mathbf{z}}\;, \tag{3.14c}$$

$$\hat{\boldsymbol{\beta}} = \cos\beta_0\,\cos\phi\,\hat{\mathbf{x}} + \cos\beta_0\,\sin\phi\,\hat{\mathbf{y}} + \sin\beta_0\,\hat{\mathbf{z}}\;. \tag{3.14d}$$

It is now convenient to express the incident and diffracted fields in terms of the triads of unit vectors $(\hat{\mathbf{s}}^i, \hat{\boldsymbol{\phi}}_0, \hat{\boldsymbol{\beta}}_0)$ and $(\hat{\mathbf{s}}^d, \hat{\boldsymbol{\phi}}, \hat{\boldsymbol{\beta}})$ associated with the incident and diffracted rays. The diffracted field $\mathbf{E}^d$ at the observation point $\mathbf{r}$ is then

$$\mathbf{E}^{d\,(\mathrm{UTD})}(\mathbf{r}) = -\frac{1}{\sqrt{s^d}}\,e^{i\,k\,s^d}\left\{ D_{\mathrm{s}}(\beta_0, \phi_0, \phi, k, s^d)\,\hat{\boldsymbol{\beta}}\,\hat{\boldsymbol{\beta}}_0 \cdot \mathbf{E}^i(\mathbf{r}_0) \right.$$
$$\left. + D_{\mathrm{h}}(\beta_0, \phi_0, \phi, k, s^d)\,\hat{\boldsymbol{\phi}}\,\hat{\boldsymbol{\phi}}_0 \cdot \mathbf{E}^i(\mathbf{r}_0) \right\}\;, \tag{3.15}$$

in terms of the incident field $\mathbf{E}^i$ at the corresponding diffraction point $\mathbf{r}_0$ (located on the edge), the path length of the diffracted ray $s^d = |\mathbf{r} - \mathbf{r}_0|$, and the "soft" and "hard" UTD diffraction coefficients D_{s} and D_{h}. The latter are given by

$$D_{\substack{\mathrm{s}\\\mathrm{h}}}(\beta_0, \phi_0, \phi, k, s^d) = -\frac{e^{i\pi/4}}{2\sqrt{2\pi k}\,\sin\beta_0}\left\{ \sec\frac{\phi - \phi_0}{2}\,F\left(2\,k\,s^d\,\sin^2\beta_0\,\cos^2\frac{\phi - \phi_0}{2}\right) \right.$$
$$\left. \mp \sec\frac{\phi + \phi_0}{2}\,F\left(2\,k\,s^d\,\sin^2\beta_0\,\cos^2\frac{\phi + \phi_0}{2}\right) \right\}\;, \tag{3.16}$$

where the function F is, as before, defined by Eq.(3.5).

Since $\rho = s^d\,\sin\beta_0$, we can see that the arguments of the functions F in Eq.(3.16) are exactly the same as in Eqs. (3.4) and (3.11). Verification of Eq.(3.11) for the E-polarization problem is now straightforward. By taking the z-component of the diffracted electric field (3.15) we find that only the soft diffraction coefficient contributes, because $\hat{\mathbf{z}} \cdot \hat{\boldsymbol{\phi}} = 0$. Since the E-polarization implies incident unit field $\mathbf{E}^i = -\hat{\boldsymbol{\beta}}_0$, we have $\hat{\boldsymbol{\beta}}_0 \cdot \mathbf{E}^i = -1$, and substituting D_{s} of Eq.(3.16) into Eq.(3.15), we immediately reproduce Eq.(3.11), i.e.,

$$E_z^{d\,(\mathrm{UTD})}(\mathbf{r}) = E_z^d(\mathbf{r})\;. \tag{3.17}$$

In order to compare the UTD expression with the exact solution (3.4) for the H-polarization, we first use the *exact relation* (following from the Maxwell equations)

$$\mathbf{H}^{d\,(\mathrm{UTD})} = -\frac{i}{k}\,\nabla \times \mathbf{E}^{d\,(\mathrm{UTD})}\;, \tag{3.18}$$

expressing the magnetic field in terms of the diffracted electric field (3.16).

To simplify the result, we specialize now to normal incidence, $\beta_0 = \pi/2$. In this case we have

$$H_z^{d\,(\mathrm{UTD})}(\rho, \phi) = -\frac{\mathrm{i}}{k} \, \partial_s \, E_\phi^{d\,(\mathrm{UTD})}(\rho, \phi)$$

$$= \mathrm{e}^{\mathrm{i}\pi/4} \, \mathrm{e}^{\mathrm{i}k\rho} \, \frac{1}{2\sqrt{2\pi k\rho}}$$

$$\left\{ \sec\frac{\phi - \phi_0}{2} \left[1 + \cos(\phi - \phi_0) \left[1 - F\left(2\,k\rho \, \cos^2 \frac{\phi - \phi_0}{2} \right) \right] \right] \right.$$

$$\left. + \sec\frac{\phi + \phi_0}{2} \left[1 + \cos(\phi + \phi_0) \left[1 - F\left(2\,k\rho \, \cos^2 \frac{\phi + \phi_0}{2} \right) \right] \right] \right\} H_z^{\mathrm{i}} \; .$$

$$(3.19)$$

Eq.(3.6) implies that Eq.(3.19) approaches the exact result (3.4) for large $k\rho$. To assess the significance of the differences for small values of $k\rho$ for the computation of the current (Eq.(3.10)), we evaluate the discontinuity of the magnetic field across the screen,

$$\Delta H_z^{d\,(\mathrm{UTD})}(\rho) = H_z^{d\,(\mathrm{UTD})}(\rho, 0) - H_z^{d\,(\mathrm{UTD})}(\rho, 2\pi)$$

$$= \mathrm{e}^{\mathrm{i}\pi/4} \, \mathrm{e}^{\mathrm{i}k\rho} \, \frac{2}{\sqrt{2\pi k\rho}} \, \sec\frac{\phi_0}{2} \left\{ 1 + \cos\phi_0 \left[1 - F\left(2\,k\rho \, \cos^2 \frac{\phi_0}{2} \right) \right] \right\} H_z^{\mathrm{i}} \; .$$

$$(3.20)$$

This results agrees with the exact Eq.(3.9) (for $\beta_0 = \pi/2$) only for large arguments of the transition function F, but not for small arguments. For $\rho \to 0$ the UTD result is actually singular ($\sim 1/\sqrt{\rho}$), while the exact expression (3.9) tends to a constant.

We have thus found that if we use the UTD formula (3.15) to calculate the electric field, and then evaluate the magnetic field using the *exact relation* following from Maxwell's equations, the result is *incorrect*. On the other hand, we obtain a *correct* result if we express the magnetic field in terms of the electric field using the *approximate relation*

$$\mathbf{H}^{d\,(\mathrm{UTD})} \simeq \hat{\mathbf{s}}^d \times \mathbf{E}^{d\,(\mathrm{UTD})} \; , \qquad (3.21)$$

valid only asymptotically, and assuming the ray-optical nature of the electric field. Eq.(3.21) implies now

$$H_z^{d\,(\mathrm{UTD})}(\mathbf{r}) \simeq \hat{\mathbf{z}} \cdot (\hat{\mathbf{s}}^d \times \mathbf{E}^{d\,(\mathrm{UTD})}(\mathbf{r})) = -\frac{1}{\sqrt{s^d}} \, \mathrm{e}^{\mathrm{i}k\,s^d} \, \hat{\mathbf{z}} \cdot \hat{\boldsymbol{\beta}} \, D_{\mathrm{h}}(\beta_0, \phi_0, \phi, k, s^d) \, \hat{\boldsymbol{\phi}}_0 \cdot \mathbf{E}^{\mathrm{i}}(\mathbf{r}_0) \; , \quad (3.22)$$

which coincides exactly with Eq.(3.4).

It would, therefore, seem that UTD does reproduce the correct fields near the diffraction edge, provided the magnetic field is calculated according to Eq.(3.21), and not Eq.(3.18). This, however, is not an acceptable solution for computing *all components* of the magnetic field. In particular, if we consider again the E-polarization case, taking for simplicity normal incidence ($\beta_0 = \pi/2$), the electric field is directed along the edge (the z-axis) and is given by Eqs. (3.11) and (3.17). In this case, if we evaluate the magnetic field on the surface of the screen, we have $\hat{\mathbf{s}}^d = \hat{\mathbf{x}}$, and Eq.(3.21)

yields the magnetic field in the direction **normal** to the screen, $\hat{s}^d \times \mathbf{E}^{d\,(\text{UTD})} \sim \hat{y}$. Therefore, the resulting electric current (Eq.(3.1)) is exactly **zero**, leading to the incorrect conclusion that soft diffraction generates no scattered field at all; while in reality the current is nonzero, because a tangential magnetic field results from the **normal derivative** of the tangential electric field, and, according to Eq.(3.18), we have $H_x^{d\,(\text{UTD})} = -\mathrm{i}/k\,\partial_y\,E_z^{d\,(\text{UTD})}$.

Behavior of modified UTD (nUTD) fields and currents near diffraction edges

We found above that the conventional UTD does not, in general, reproduce correct near fields and thus surface currents near the diffraction edges.

In this situation we suggest a modification of the UTD procedure to allow for a correct description of all field components, and a reliable computation of surface currents. Here we sketch the modified formulation only for a straight edge of a flat screen; generalization to other cases is more complex but feasible.

Our starting point are the exact half-plane solutions (3.11) and (3.4) for the E- and H-polarization. These solutions can be, without any approximation, represented as

$$E_z^d = -\frac{1}{\sqrt{s}}\,\mathrm{e}^{\mathrm{i}\,k\,s}\,D_s\,E_z^i \;, \tag{3.23a}$$

$$H_z^d = -\frac{1}{\sqrt{s}}\,\mathrm{e}^{\mathrm{i}\,k\,s}\,D_h\,H_z^i \;, \tag{3.23b}$$

where $s \equiv s^d$.

We use Eq.(3.23b) for the z-component of the magnetic field, and express the remaining components of $\mathbf{H}^d$ in terms of H_z^d and E_z^d, by applying the well known formula for the transverse components of the magnetic field in terms of the z-components, valid for solution of Maxwell equation having an exponential z-dependence, in our case $\exp(-\mathrm{i}\,k\,z\,\cos\beta_0)$. We also express the incident fields E_z^i and H_z^i in terms of the incident magnetic field components along the triad of vectors $(\hat{s}^i, \hat{\phi}_0, \hat{\beta}_0)$. Assuming transversality of the incident fields, we have $\mathbf{H}^i = \hat{\phi}_0\,H_\phi^i + \hat{\beta}_0\,H_\beta^i$, and, from Maxwell's equations,

$$E_z^i = \sin\beta_0\,H_\phi^i \;, \qquad H_z^i = -\sin\beta_0\,H_\beta^i \;. \tag{3.24}$$

Finally, we substitute in the resulting expression the relations Eqs. (3.23). In this way we find the total diffracted field as

$$\begin{aligned}
\mathbf{H}^d &= \frac{\mathrm{i}}{k\sin^2\beta_0}\left[\hat{\mathbf{z}}\times\nabla_{\mathrm{T}}\,E_z^d - \cos\beta_0\,\nabla_{\mathrm{T}}\,H_z^d\right] + \hat{\mathbf{z}}\,H_z^d \\
&= -\frac{\mathrm{i}}{k\sin^2\beta_0}\left\{\sin\beta_0\,\hat{\mathbf{z}}\times\nabla_{\mathrm{T}}\,D_s\,H_\phi^i + \cos\beta_0\,\sin\beta_0\,\nabla_{\mathrm{T}}\,D_h\,H_\beta^i\right\}\frac{1}{\sqrt{s}}\,\mathrm{e}^{\mathrm{i}\,k\,s} \\
&\quad + \hat{\mathbf{z}}\,\sin\beta_0\,D_h\,H_\beta^i\,\frac{1}{\sqrt{s}}\,\mathrm{e}^{\mathrm{i}\,k\,s} \;. \tag{3.25}
\end{aligned}$$

We use now

$$\nabla_{\mathrm{T}} = \hat{\rho}\,\sin\beta_0\,\partial_s + \hat{\phi}\,\frac{1}{s\sin\beta_0}\,\partial_\phi \;, \tag{3.26}$$

where

$$\hat{\rho} = \cos\phi\,\hat{\mathbf{x}} + \sin\phi\,\hat{\mathbf{y}} \ . \tag{3.27}$$

To the leading order, the gradients in Eq.(3.25) act only on the factor $\exp(i\,k\,s)$,

$$\nabla_{\mathrm{T}}\,e^{i\,k\,s} = \hat{\rho}\,ik\,\sin\beta_0\,e^{i\,k\,s} \ ; \tag{3.28}$$

this is the same approximation that underlies Eq.(3.21). By using $\hat{\mathbf{z}}\times\hat{\rho} = \hat{\phi}$ and $\cos\beta_0\,\hat{\rho}+\sin\beta_0\,\hat{\mathbf{z}} = \hat{\beta}$, we obtain then the conventional UTD result

$$\mathbf{H}^{\mathrm{d}} \simeq \mathbf{H}^{\mathrm{d\,(UTD)}} \equiv \frac{1}{\sqrt{s}}\,e^{i\,k\,s}\left\{ D_{\mathrm{s}}\,\hat{\phi}\,\hat{\phi}_0\cdot\mathbf{H}^{\mathrm{i}} + D_{\mathrm{h}}\,\hat{\beta}\,\hat{\beta}_0\cdot\mathbf{H}^{\mathrm{i}} \right\} \ , \tag{3.29}$$

analogous to Eq.(3.15).

To obtain the *exact* expression for the diffracted field, we differentiate the diffraction coefficients in Eq.(3.25) using the relation (3.8), and express the result in terms of the unit vectors $\hat{\mathbf{s}}^{\mathrm{d}} \equiv \hat{\mathbf{s}}$, $\hat{\phi}$, and $\hat{\beta}$ by writing $\hat{\rho} = \sin\beta_0\,\hat{\mathbf{s}} + \cos\beta_0\,\hat{\beta}$. We find that exact diffracted field is

$$\mathbf{H}^{\mathrm{d}} = \mathbf{H}^{\mathrm{d\,(UTD)}} + \delta\mathbf{H}^{\mathrm{d}} \ , \tag{3.30}$$

where the additional term $\delta\mathbf{H}^{\mathrm{d}}$ can be represented in terms of a new dyadic diffraction coefficient $\mathcal{D}$ as

$$\delta\mathbf{H}^{\mathrm{d}} = \frac{1}{\sqrt{s}}\,e^{i\,k\,s}\,\mathcal{D}\,\mathbf{H}^{\mathrm{i}} \ . \tag{3.31}$$

Here $\mathcal{D}$ is a dyadic form which can be expressed in terms of the unit vectors associated diffracted and incident rays. In a compact matrix notation it has the form

$$\mathcal{D} = [\hat{\mathbf{s}}\quad\hat{\phi}\quad\hat{\beta}]\begin{bmatrix}\mathcal{D}_{s\phi} & \mathcal{D}_{s\beta}\\ \mathcal{D}_{\phi\phi} & \mathcal{D}_{\phi\beta}\\ \mathcal{D}_{\beta\phi} & \mathcal{D}_{\beta\beta}\end{bmatrix}\begin{bmatrix}\hat{\phi}_0\\ \hat{\beta}_0\end{bmatrix} = [\hat{\mathbf{s}}\quad\hat{\phi}\quad\hat{\beta}]\begin{bmatrix}\sin\beta_0 & 0\\ 0 & 1\\ \cos\beta_0 & 0\end{bmatrix}\begin{bmatrix}\mathcal{D}_{\rho\phi} & \mathcal{D}_{\rho\beta}\\ \mathcal{D}_{\phi\phi} & \mathcal{D}_{\phi\beta}\end{bmatrix}\begin{bmatrix}\hat{\phi}_0\\ \hat{\beta}_0\end{bmatrix} \ , \tag{3.32}$$

where the dyadic coefficients associated with the vectors $\hat{\rho}$ and $\hat{\phi}$ are

$$\mathcal{D}_{\rho\phi} = -C(k,\beta_0)\left\{ \sin\psi_-\left[1 - F\left(\xi_-\right)\right] - \sin\psi_+\left[1 - F\left(\xi_+\right)\right] \right\} \ , \tag{3.33a}$$

$$\mathcal{D}_{\phi\phi} = -C(k,\beta_0)\,\sin^2\beta_0\left\{ \cos\psi_-\left[1 - F\left(\xi_-\right)\right] - \cos\psi_+\left[1 - F\left(\xi_+\right)\right] \right\} \ , \tag{3.33b}$$

$$\mathcal{D}_{\rho\beta} = -C(k,\beta_0)\,\sin^2\beta_0\,\cos\beta_0\left\{ \cos\psi_-\left[1 - F\left(\xi_-\right)\right] + \cos\psi_+\left[1 - F\left(\xi_+\right)\right] \right\} \ , \tag{3.33c}$$

$$\mathcal{D}_{\phi\beta} = \ \ C(k,\beta_0)\,\cos\beta_0\left\{ \sin\psi_-\left[1 - F\left(\xi_-\right)\right] + \sin\psi_+\left[1 - F\left(\xi_+\right)\right] \right\} \ . \tag{3.33d}$$

Here

$$C(k,\beta_0) = \frac{e^{i\,\pi/4}}{\sqrt{2\pi k}\,\sin\beta_0} \ , \tag{3.34}$$

$\psi_{\mp} \equiv \frac{1}{2}(\phi\mp\phi_0)$, and $\xi_{\mp} = 2\,k\,s\,\sin^2\beta_0\,\cos^2\psi_{\mp}$. We note that the diffracted field $\delta\mathbf{H}^{\mathrm{d}}$ is *not transverse* – it contains a longitudinal component proportional to $\hat{\mathbf{s}}$. We also note that all the

24

diffraction coefficients (3.33) are proportional to $[1 - F(\cdots)]$, i.e., they fall off rapidly outside the transition region.

In the special case of normal incidence ($\beta_0 = \pi/2$) the total diffracted field can be written explicitly as

$$\begin{aligned}
\mathbf{H}^{\mathrm{d}}(\rho, \phi) = -e^{i\pi/4}\, e^{ik\rho}\, \frac{1}{2\sqrt{2\pi k\rho}} \Big\{ &\hat{\rho}\, \big[2\sin\psi_-\,[1 - F(\xi_-)] - 2\sin\psi_+\,[1 - F(\xi_+)]\big]\, H^{\mathrm{i}}_\phi \\
&+ \hat{\phi}\, \big[2\cos\psi_-\,[1 - F(\xi_-)] - 2\cos\psi_+\,[1 - F(\xi_+)] \\
&\qquad + \sec\psi_-\, F(\xi_-) - \sec\psi_+\, F(\xi_+)\big]\, H^{\mathrm{i}}_\phi \\
&+ \hat{z}\, \big[\sec\psi_-\, F(\xi_-) + \sec\psi_+\, F(\xi_+)\big]\, H^{\mathrm{i}}_\beta \Big\}\ ,
\end{aligned} \tag{3.35}$$

where now $\xi_\mp = 2\,k\rho \cos^2 \psi_\mp$. The magnetic field discontinuity is then

$$\begin{aligned}
\Delta \mathbf{H}^{\mathrm{d}}(\rho) = &-e^{i\pi/4}\, e^{ik\rho}\, \frac{2}{\sqrt{2\pi k\rho}} \\
&\left\{ -\hat{\rho}\, 2\sin\frac{\phi_0}{2}\left[1 - F\left(2\,k\rho \cos^2\frac{\phi_0}{2}\right)\right] H^{\mathrm{i}}_\phi + \hat{z}\, \sec\frac{\phi_0}{2}\, F\left(2\,k\rho \cos^2\frac{\phi_0}{2}\right) H^{\mathrm{i}}_\beta \right\}\ .
\end{aligned} \tag{3.36}$$

Here the second term, proportional to $\hat{z}$, is the same as in conventional UTD, and is due to "hard diffraction". It represents the magnetic field directed along the edge, giving rise to the current (3.10) in the x-direction,

$$J_x(\rho) \equiv J_x^{(UTD)}(\rho) = -2\,\Delta H_z(\rho)\ , \tag{3.37}$$

normal to the edge. The first term, proportional to $\hat{\rho} = \hat{x}$ is the *new near field contribution* due to our modification of UTD. It is associated with "soft diffraction", and yields a current component

$$J_z(\rho) \equiv \delta J_z(\rho) = 2\,\Delta H_\rho(\rho) \tag{3.38}$$

in the z-direction, i.e., *along the edge*. As expected, this current component behaves for small ρ as $1/\sqrt{\rho}$, and decreases rapidly away from the edge (outside the transition region).

In Fig. 19 we plot real parts of the current components J_x and J_z as functions of $k\rho$, for two values of ϕ_0: 90° and 170°. The plots show that, as ϕ_0 approaches 180° the transition region extends to larger values of $k\rho$, and the current J_z remains sizable over a wider range.

It is of interest to note that the size of our correction $\delta \mathbf{H}^{\mathrm{d}}$ to the diffracted field is of the same order as the difference between the UTD and GTD result (the latter being UTD with all transition functions F replaced by unity), i.e., schematically,

$$\delta \mathbf{H}^{\mathrm{d}} \sim \mathbf{H}^{\mathrm{d}\,(\mathrm{UTD})} - \mathbf{H}^{\mathrm{d}\,(\mathrm{GTD})}\ . \tag{3.39}$$

Indeed, both quantities are sums of terms proportional to $[1 - F(\cdots)]$. For instance, in our example Eqs. (3.37) and (3.38) imply that, assuming unit values of H^{i}_β and H^{i}_ϕ,

$$\delta J_z(\rho) = 2\sin\phi_0\left[J_x^{(UTD)}(\rho) - J_x^{(GTD)}(\rho)\right]\ . \tag{3.40}$$

For a more quantitative estimate we evaluate the integrals of the current components, e.g.,

$$\int_0^\infty d\rho \, \delta J_z(\rho) = i \frac{4\sqrt{2}}{k} \sin \frac{\phi_0}{2} \, g\left(\frac{\cos\phi_0}{1+\cos\phi_0}\right) \,, \tag{3.41}$$

where

$$g(\sigma) = \frac{1}{\sqrt{\pi}} e^{-i\pi/4} \int_0^\infty du \, \frac{1}{\sqrt{u}} e^{iu} \left[1 - F\left(\frac{u}{1-\sigma}\right)\right]$$

$$= 1 + \frac{\sqrt{1-\sigma}}{\sigma} \left\{1 - e^{-i\pi/4} \frac{1}{\sqrt{2(1-\sigma^2)}} \left[\left(\sqrt{1-\sigma^2}+i\sigma\right)^{1/2} + i\left(\sqrt{1-\sigma^2}-i\sigma\right)^{1/2}\right]\right\} \,. \tag{3.42}$$

The function $g(\sigma)$ is defined for $-\infty < \sigma \leq \frac{1}{2}$ with the square-root branch specified by $\text{Im}\,\sigma < 0$, i.e., $\sqrt{1-\sigma^2} = -i\sqrt{\sigma^2-1}$ for $\sigma < -1$. It is real, and is normalized so that $g(0) = \frac{1}{2}$ (corresponding to $\phi_0 = \pi/2$), and $g(-\infty) = 1$ (corresponding to $\phi_0 = \pi$). From its plot (Fig. 20) it is apparent that the size of both δJ_z and $J_x^{(UTD)} - J_x^{(GTD)}$ increases when we approach $\phi_0 = 180°$.
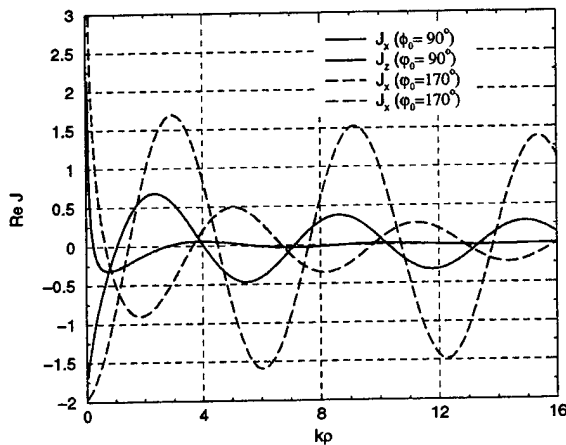
Fig. 19: Real parts of the current components (3.37) and (3.38) as functions of $k\rho$, for $\phi_0 = 90°$ and $\phi_0 = 170°$, assuming unit values of H_β^i and H_ϕ^i.
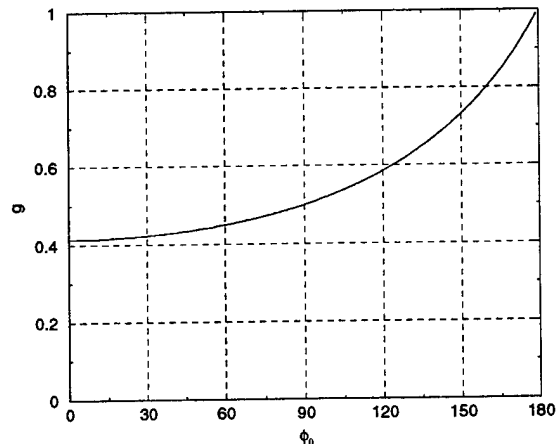
Fig. 20: The factor g of Eq.(3.42) plotted as a function of the angle ϕ_0.

In Section 4 we present examples in which we compare scattering cross-sections obtained using the MoM, with those computed using currents determined from GTD, UTD, and our modified version of UTD. We find there the contributions due to the modification of UTD significantly improve the agreement of asymptotic approximations with the exact results.

26

3.2. Direct field computation

We return now to the problem of determining scattered fields directly form the fields defined on the WFs.

Properties of the WFs reflected from smooth curved surfaces, and surfaces consisting of flat facets, are quite different. In the first case the WF is curved, and the individual rays have also nonzero curvatures. In the second case, meanwhile, the reflected WF consists of flat surface segments, and the rays carry zero curvatures (provided we consider a plane incident WF).

Similarly, WFS diffracted from straight and curved edges behave differently: they are either cylindrical (conical), or spherical waves. In the following we consider thus only the processes which generate *spherical* waves, amenable to direct computation of the scattering cross-section.

By definition, the scattering amplitude is defined as the appropriately normalized asymptotic value of the scattered field. A vector-valued scattering amplitude can be defined in terms of the magnetic fields as the limit

$$\mathcal{A}(\hat{\mathbf{R}}) = \lim_{R \to \infty} 4\pi R \, e^{-ikR} \, \mathbf{H}(\mathbf{R}) \,, \tag{3.43}$$

assuming a **unit strength** incident field, $|\mathbf{H}^{\text{in}}| = 1$, and using the field $\mathbf{H}$ *including* the rapidly varying phase factor (as opposed to the smoothly varying field $\widetilde{\mathbf{H}}$ used in Eq.(3.2)). According to the laws of GO we can calculate the field $\mathbf{H}$ at any observation point $\mathbf{R}$ provided we identify all rays passing through that point. Fig. 21 shows two such rays, originating at points $\mathbf{r}_1$ and $\mathbf{r}_2$ of a certain WF, characterized by the given fixed phase ks (where s denotes the length of the propagation path).
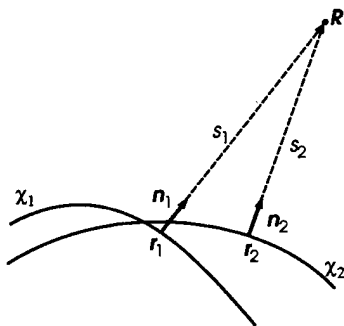
Fig. 21: Contributions to the field at the observation point $\mathbf{R}$ due to two rays originating at points $\mathbf{r}_j$ on segments χ_j of a WF ($j = 1, 2$), and propagating along the normals $\mathbf{n}_j$ towards the observation point.

Since the rays in the regions outside the scatterer evolve according to the laws of GO, the contributions of the fields at points $\mathbf{r}_j$ to the field $\mathbf{H}(\mathbf{R})$ are given by (cf. Eq.(3.2))

$$\mathbf{H}^{(j)}(\mathbf{R}) = \sqrt{\frac{\rho_1^{(j)} \rho_2^{(j)}}{(\rho_1^{(j)} + s_j)(\rho_2^{(j)} + s_j)}} \; e^{iks_j} \, \mathbf{H}(\mathbf{r}_j) \,, \tag{3.44}$$

where $\rho_n^{(j)}$ are the ray's curvatures at the points $\mathbf{r}_j$, and $s_j = |\mathbf{R} - \mathbf{r}_j|$ is the propagation path length. Since, in the limit $R \to \infty$, we have $s_j \simeq R - \hat{\mathbf{R}} \cdot \mathbf{r}_j$, the amplitude (3.43) becomes

$$\mathcal{A}(\hat{\mathbf{R}}) = 4\pi \sum_j \sqrt{\rho_1^{(j)} \rho_2^{(j)}} \, e^{-ik\,\hat{\mathbf{R}} \cdot \mathbf{r}_j} \, \mathbf{H}(\mathbf{r}_j) \; ; \tag{3.45}$$

actually, in practice we apply the GO evolution laws to *real* fields with the common phase $\exp(iks)$ factored out.

The conventionally normalized differential scattering cross-section (per unit solid angle) for scattering in the direction $\hat{\mathbf{R}}$ and for the scattered wave magnetic-field polarization $\mathbf{h}$ is then given by

$$\sigma_e(\hat{\mathbf{R}}) = \frac{1}{4\pi} |\mathbf{h}^* \cdot \mathcal{A}(\hat{\mathbf{R}})|^2 \; . \tag{3.46}$$

According to Eq.(3.45), the scattering amplitude has the correct dimension of length, and the scattering cross-section the dimension of length squared.

The procedure for computing the scattering amplitude $\mathcal{A}(\hat{\mathbf{R}})$ is thus as follows:

1. Select a sufficiently evolved WF characterized by some evolution parameter s.
2. On this WF locate all points $\mathbf{r}_j$ whose normals $\mathbf{n}_j$ coincide with the direction $\hat{\mathbf{R}}$.
3. Sum contributions of these points according to Eq.(3.45).

Having found the vector-valued amplitude $\mathcal{A}(\hat{\mathbf{R}})$, we can then computing the conventional scattering amplitudes by taking scalar products of $\mathcal{A}$ with the magnetic field polarization vectors $\mathbf{h}$ of the scattered wave. Consequently, the differential polarized cross-sections are proportional to the squares of the absolute values of such amplitudes.

Some remarks are in order here:

(A) In the step 1. above by a "sufficiently evolved" WF we mean a WF containing contributions from a sufficient number of reflections (if there are multiple reflections in the problem). In practice, we can compute the scattering amplitudes for a number of WFs, and monitor the convergence of the result. Typically, the convergence is relatively fast, since the consecutive reflections give weaker and weaker contributions to the field.

(B) Since the WF is represented in terms of a finite number of rays, we cannot expect to find normals $\mathbf{n}_j$ pointing *exactly* in the direction $\hat{\mathbf{R}}$. Instead, we have to use an interpolation procedure: We first map the mesh defining the WF onto a unit sphere, on which the nodes are the normals $\mathbf{n}$. On this unit sphere we find then all the mesh faces (triangles) intersected by the direction vector $\mathbf{R}$. Finally, for each such triangle we interpolate the field values associated with the three vertices to the point representing the required direction $\hat{\mathbf{R}}$; for sufficiently small triangles, linear interpolation is adequate. An important element of the procedure is that in the interpolation we use the smoothly varying fields $\tilde{\mathbf{H}}$ (as in Eq.(3.2)), and only then we multiply the result by the appropriate phase factor.

3.3 Surface current computation

The goal of the current-based approach is to obtain equivalent surface currents corresponding to the field of the WF, and use these currents to compute the scattered field, or for other purposes (as we discuss below). For a p.e.c. scatterer the equivalent surface electric current is given by Eq.(3.1), hence the values of the magnetic field on the surface are required.

Besides computing the scattered field (as the Kirchhoff integral of the current), a natural applications of this type of calculations might be to develop an interface to integral-equation methods, in which the unknown quantities are surface currents. There is a need for such an interface in several circumstances:

1. Hybrid methods require input for solving low-frequency integral equations in the form of the initial current generated by the field originating from the high-frequency components of the object. Computation of this current provides, effectively, a coupling between the system components described by low-frequency and asymptotic methods.

2. In an "enhanced" formulation of Physical Optics (PO) the required input for scatterer field computation is the current induced on the scatterer surface by the incident field, and by the fields due to GO reflections (in this case the WF is thus obtained in the GO approximation).

3. The rigorous method of high-frequency asymptotic integral equations considered in [2, 3] requires an Ansatz for the solution for the surface current. This Ansatz is in the form of a linear combination of unknown slowly varying functions multiplying rapidly oscillating functions representing asymptotic high-frequency solutions. These asymptotic solutions, generated by all possible reflection and diffraction processes, can be very naturally extracted from the purely geometrical construction of WFs (even without the need of computing diffracted field by means of UTD or similar methods).

One of the first questions we encounter when trying to determine surface currents is how these currents should be represented and parameterized. At high frequencies it is, clearly, impractical to use a representation of the current in terms of their values at selected points on the surface, since this would require about 10 sampling points per wavelength. A more useful representation is its parameterization as a sum of rapidly oscillating exponential factors multiplied by smoothly varying coefficients. Such parameterizations would be applicable in some surface patches D_j centered around some "current points" R_j. The sizes of the regions D_j is assumed to be of the order of the local ray spacing, and they are required to cover the entire scatterer surface S.

Let us assume for a moment that a set of M distinct rays (originating from different segments of the WF) coalesce at a current point R_j. The conventional WF form of the fields suggest then the representation

$$\mathbf{J}(\mathbf{r}) = \sum_{m=1}^{M} \mathbf{A}_m(\mathbf{r}) \, e^{i \, k \, S_m(\mathbf{r})} \qquad \text{for } \mathbf{r} \in D_j \, , \tag{3.47}$$

i.e., a sum of contributions of distinct rays arriving at $\mathbf{R}_j$. Here S_m's are the phases of the individual rays, defined so that $\nabla S_m(\mathbf{r}) = \mathbf{n}_m$, where $\mathbf{n}_m$ is the unit vector in the direction of the ray propagation. The amplitudes $\mathbf{A}_m$ are parameterized as constant amplitudes multiplied by the conventional ray divergence factors involving the ray evolution parameter and the curvatures.

If the rays arrive at the surface not exactly at the "current point" R_j, but in its vicinity, it is necessary to devise a procedure to interpolate the rays to the point R_j, and then find a parameterization of the phases and coefficients in Eq.(3.47). Such a procedure can be based on WF field interpolation within sets of neighboring rays, similarly to methods using "ray cells" (i.e., prisms formed by the corresponding faces of the meshes on the two consecutive WFs).

Our algorithm can be formulated as a procedure for computing field values at any set of observation points (not necessarily points on the scatterer surface). Currents can be then obtained by applying the algorithm to surface points, and using $J = 2n \times \Delta H$, where ΔH is the discontinuity of the magnetic field across the surface.

Conceptually, the interpolation algorithm can be stated as follows:

1. Specify a set $\mathcal{R}$ of "field points" R_j at which the fields are to be computed; the spacing of these points should be sufficiently small to resolve the variation of the amplitudes of the fields (but not variation of their phases).

2. At every step of the WF evolution find, for each "field point" R_j, a set of nearby rays (within the distance of a few average ray-ray spacings). These rays are selected from the set of rays propagating from the previous WF to the current WF χ (Fig. 22).

3. For each of nearby rays ξ construct a ray ξ_{R_j} passing through the point R_j and parallel to the ray ξ. The length Δs of the ray is set to the distance between the point R_j and the WF, measured along the direction of the ray ξ.

4. By evolving the ray ξ_{R_j} forward in time find its intersection with the WF χ. Identify the WF face f intersected by the ray (Fig. 22). (We note that a continuation of the ray ξ_{R_j} may intersect further segments of the WF, but theses intersections are irrelevant, since we are only computing contributions of the rays evolved up to the WF χ.)

5. Identify the rays ξ_{f1}, ξ_{f2}, and ξ_{f3}, associated with the corners of the face f. Evolve these rays *backward* through the distance Δs to form an image f' of the face f. We refer to the prism built on the faces f and f' as a *ray tube*.

6. Check if the point R_j is located inside the face f'. If it is, continue to the point 7. If it is not, determine the average direction n_{123} of the rays ξ_{fi} ($i = 1, 2, 3$), construct a *new ray* ξ_{R_j} emerging from R_j in the direction of n_{123}, and return to the point 4.

7. Interpolate field values associated with the ends of the rays ξ_{fi} to the point R_j.
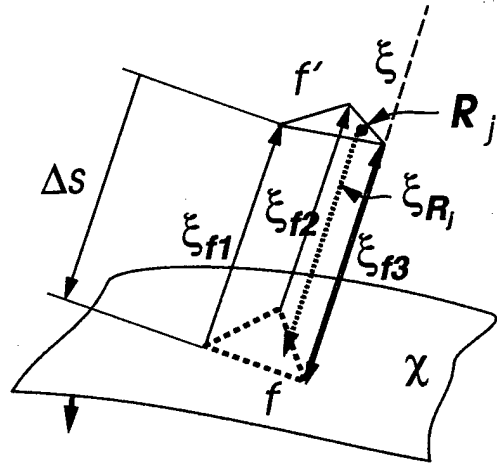
Fig. 22: The algorithm for computing a contribution of a ray to the fields at the observation point $\mathbf{R}_j$, by interpolating between rays ξ_{f1}, ξ_{f2}, and ξ_{f3} associated with a face f on the WF χ. The heavy arrow denotes the direction of WF propagation.

Several remarks and clarifications are in order here:

(a) The steps 3 to 7 are repeated for all rays passing near the observation point $\mathbf{R}_j$. If several near rays yield the same ray tube, only one of them is taken into account. Contributions to the fields from **all distinct ray tubes** are added to the field representation at $\mathbf{R}_j$. The field is represented in analogy to Eq.(3.47), i.e., in the form of constant vector amplitudes and the corresponding wave vectors. Specifically, for each of the ray tubes containing the point $\mathbf{R}_j$, we store the field amplitudes $\mathbf{E}_m(\mathbf{R}_j)$ and the phase $S_m(\mathbf{R}_j)$ evaluated at the observation point, as well as the gradient $\mathbf{n}_{j,m} = \nabla S_m(\mathbf{R}_j)$ at that point. These data provide a local parameterization of the field in the neighborhood of the point $\mathbf{R}_j$ as a sum of plane waves.

(b) If the observation points $\mathbf{R}_j$ are located on the scatterer's surface, it is understood that the WF χ is the WF computed as in the absence of the scatterer, i.e., before the effect of rays' reflections is taken into account. In fact, in our present implementation the WFs are first evolved without reflections, and then transformed by reflecting the rays.

(c) We note that our algorithm for field interpolation differs from the method being used in previous WF approaches, and based on a somewhat different concept of a "ray cell" [5, 6]. In that construction of a ray cell is specified in terms of two consecutive WFs (the "previous" and the "current" ones), while our algorithm employs only one WF (the "current" WF). Our procedure was mainly motivated by applications to diffraction: in this case we may encounter a situation where the "previous" WF simply does not exist, because the current WF, due to a diffraction process, was newly created in the considered evolution step.

(d) In order to compute the induced electric field on an open surface, it is necessary to evaluate the field slightly above and slightly below the surface. In doing that, we have to check which side of the surface is illuminated by the individual rays of the WF, and we have to take into account possible discontinuities of diffracted waves across the surface.

31

(e) In the interpolation of fields associated with the rays we have to take into account the fact that the fields may not be ray-optical (in the UTD transition regions, including the region near the diffraction source).

To summarize, the algorithm for computing the surface current, as described above, is similar to the previous method for computing the asymptotic far field, except that now the observation points are located on the scatterer surface. The resulting complication is that it is necessary to take into account contributions of all WFs during their evolution, rather than only the "far evolved" WFs, after all relevant scattering processes have occurred. In addition, an efficient current representation requires local analytic parameterizations of the current, rather than merely field or current values at some sampling points.

We also note that the above current computation algorithm is applicable both to WFs resulting from reflection as well as diffraction effects. It can be thus used both to generate currents as input for Kirchhoff integral-type computations, and for creating the initial Ansatz (including diffraction) for the solution of rigorous asymptotic surface-current integral equations.

3.4. Assessment of the scattered field computation procedures

From the practical point of view, the main advantage of the direct computation of the scattered fields is the relative simplicity of the algorithm. Its drawbacks, however, are the difficulties which appear near the scattered field caustics (we will see an example of that for scattering on a circular disc), and the fact that the only contribution to the cross-section comes from processes generating asymptotically *spherical waves*. Thus, for example, in scattering on a polyhedral object with flat faces, corner diffraction is the only mechanism generating asymptotically spherical waves, hence, corner diffraction is the only process contributing to the scattered field and to the cross section (edge diffraction generates cylindrical or conical waves). This situation appears rather unnatural, considering the fact that edge diffraction is certainly an important scattering process.

The advantage of the procedure using induced currents to compute the scattered fields is its applicability to all diffraction processes, and the fact that it avoids difficulties due to caustics in the scattered field. (The only difficulty remains if the caustic is located on or intersects the scatterer's surface.) A certain disadvantage of the approach is a relative complexity of the algorithm for current computation.

Below we present results obtained using both procedures for computing the scattered fields.

4. Examples

We give now results of scattered field and cross-section computations for several simple scatterers of various types.

Reflection off a system of spheres

We consider multiple reflection process on a system consisting of two spheres of unit radii, separated by a distance equal to the sphere diameter, as shown schematically in Fig. 23. The incident plane WF approaches the spheres along the negative z-axis, with the electric field along the x-axis. The evolution step length is 0.3. For the cross-section computation we assume the wavelength

32

$\lambda = 0.2$ (i.e., the spheres diameters 10 λ). Fig. 24 shows the differential bistatic cross-section for the vertical (θ-) polarization, compared with the exact result obtained using a LF code (in this case, our integral-equation solver with FMM compression), with the discretization leading to a problem with about 100,000 unknowns. The differential cross-section shown is the conventional dimensionless cross-section $\hat{\sigma} \equiv \sigma/\lambda^2$ normalized to the wavelength squared.

The rapidly oscillating structure in the cross-sections of Fig. 24 is due to interference of reflections from the two spheres. The flat segment in the cross-section results from one sphere obscuring the view of the other, and is due to single reflection from one sphere only. The agreement of the asymptotic (GO) and exact cross-sections is good in the near-back-scattering region, where the main contributions come from single reflections from the individual scatterers. As expected, the cross-sections do not agree near 90° and 180°, where diffraction effects are important.
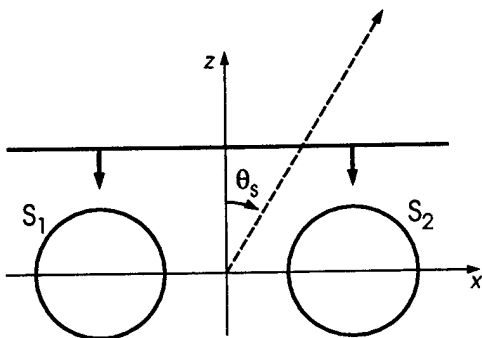
Fig. 23: A multiple-reflection problem with two spheres.
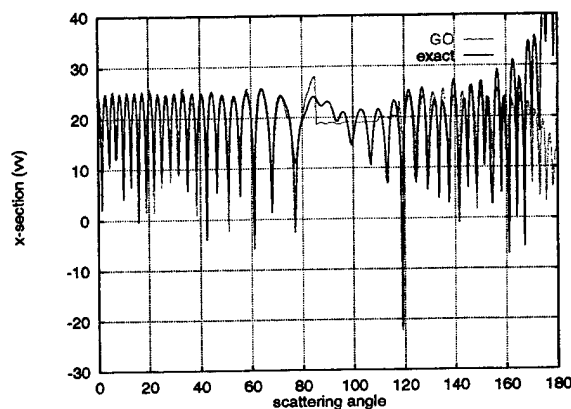
Fig. 24: Comparison of the asymptotic (GO) cross-section with the exact LF code result.

Diffraction on a circular disc

We consider here scattering on a circular disc of radius a, placed in the (x, y) plane, illuminated from above with an incident plane wave, with the electric field along the x axis. For simplicity, we take the normal incidence; in this case the first-order diffraction contribution to the GTD scattering amplitude in the scattering plane $\phi = 0$ is [13, 14]

$$\mathcal{A}(\theta) = 2\sqrt{\frac{2\pi a}{k \sin\theta}} \left[\frac{\cos(ka \sin\theta - \pi/4)}{\cos\theta/2} + i\, \frac{\sin(ka \sin\theta - \pi/4)}{\sin\theta/2} \right]. \tag{4.1}$$

This expression is valid away from the specular reflection direction $\theta = 0$ (which is also a caustic of the reflected and diffracted rays). Eq.(4.1) is due to the interference of two rays diffracted from the opposite points on the disc edge, both located on the x axis. We also note that for computation of the far-field, away from the caustics and transition regions, GTD and UTD give identical results.

33

In Fig. 25 we compare the GTD/UTD cross-section based on Eq.(4.1) with the result of our WF computation (according to Eqs. (3.45) and (3.46)), and with the rigorous MoM result. The computations were done for a disc of radius $a = 5\,\lambda$.

$$\sigma_{vv}$$
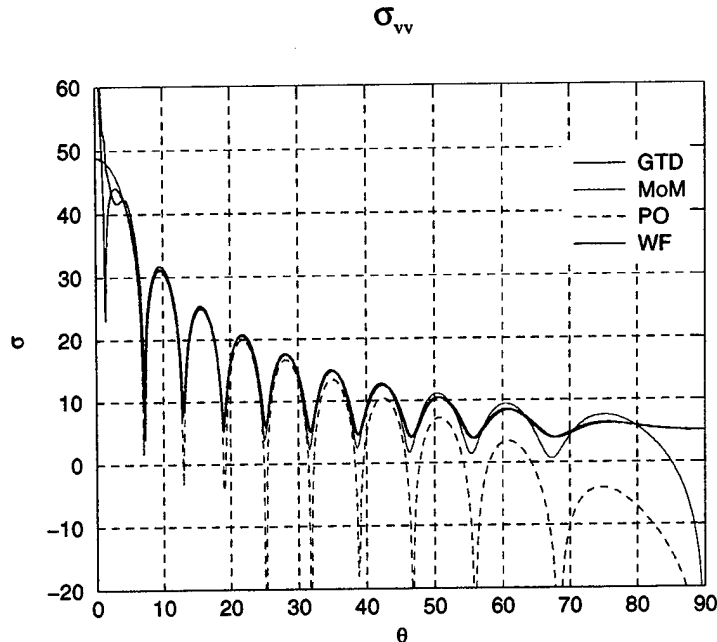
Fig. 25: The differential bistatic cross-section (in dB, normalized to the wavelength squared) for a circular disc, computed using GTD (Eq.(4.1)), the Method of Moments (MoM), Physical Optics (PO), and our WF evolution algorithm.

The comparison shows that the agreement of the WF calculation with GTD (away from the backscattering direction) is very good, except near the first (very narrow) minimum. The discrepancy in this case is likely due to inaccuracies in field interpolation in the range where the field varies very rapidly.

As expected, neither GTD/UTD nor WF computation reproduce correctly the main diffraction peak at $\theta = 0$ (which occurs in the direction of the reflected and diffracted rays caustic). Clearly, GTD/UTD give an infinite cross-section at $\theta = 0$. This deficiency may be corrected by our alternative approach to scattered field computation based on evaluating the surface current distribution (provided the current itself can be reliably calculated in the caustic region.

At the same time, the conventional PO approximation is expected to fail at larger scattering angles (in the bistatic cross-section). This well known fact is confirmed by the plots shown in Fig. 25. Thus, away from the specular reflection and caustic directions, GTD/UTD gives predictions definitely better than PO – unless the latter approximation is improved by adding diffraction contributions to the current itself.

The discrepancies between the exact (MoM) result and GTD/UTD or WF calculations are evidently due to the fact that latter include only the *first-order diffraction*. Repeated multiple diffraction from the edges of the same flat screen can be included in the WF computation, but

requires an extension of the diffraction algorithm described above. The present algorithm is not able to detect an edge as giving rise to diffraction if that edge is illuminated by a ray strictly tangential to the screen; this problem is one of the issues we discuss in Section 5.

Diffraction on a rectangular plate

In this example we consider a $6\lambda \times 6\lambda$ square plate placed in the (x, y) plane, illuminated by a plane wave of vertical (θ) or horizontal (ϕ) polarization, with the incident wave vector in the (x, z) plane ($\phi = 0$). Here we evaluate the scattered field by first computing the induced current on the scatterer surface, using the algorithm described in Section 3.3. In evaluating the current we use either only the incident wave (is equivalent to the PO approximation), or include contributions from single edge diffraction utilizing GTD, UTD, and "near-field UTD" (nUTD), as described in Section 3.

Figs. 26 and 27 show the results for the vertical-polarization bistatic cross-section as the function of the scattering angle θ, for two incidence angles: normal incidence ($\theta_i = 0°$) and near-grazing incidence ($\theta_i = 80°$).

In the normal incidence case for the vertical polarization (Fig. 26a) the cross-section resulting from the PO current is much too low for *theta* approaching 90°. The GTD current yields a better result, while the UTD and nUTD currents give rise to cross-sections almost indistinguishable from the MoM. For the horizontal polarization (Fig. 26b), on the other hand, PO, GTD, and UTD currents yield almost identical cross-sections, which, however, do not agree with the MoM result neat $\theta = 90°$. The modified UTD, nUTD, provides a much better agreement with the MoM.
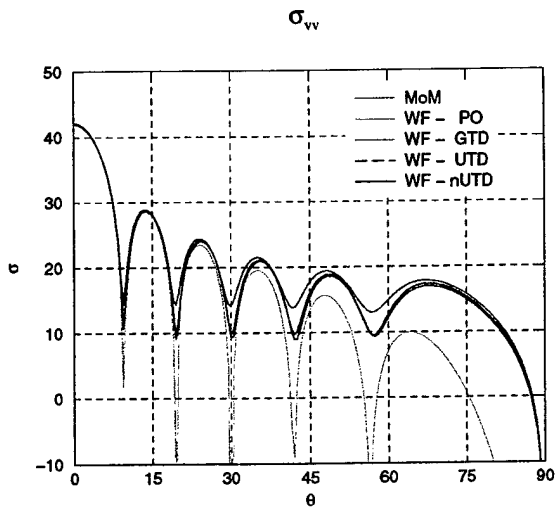
Fig. 26a: The differential bistatic cross section (in dB, normalized to the wavelength squared) for the $6\lambda \times 6\lambda$ plate at normal incidence ($\theta_i = 0°$) and for vertical polarization, computed by using the MoM and our current-based algorithm utilizing PO, GTD, UTD, and nUTD currents.
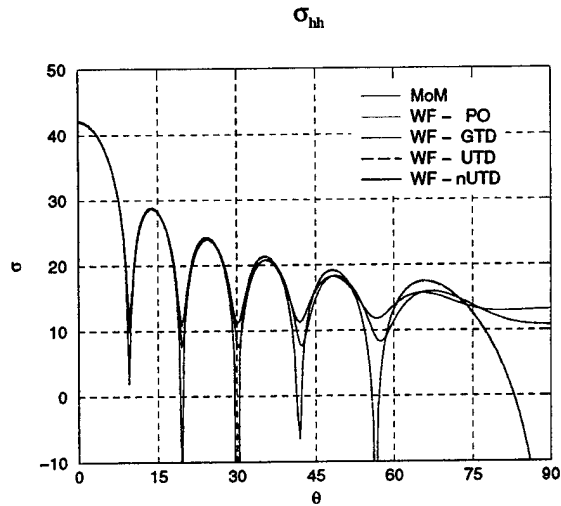
Fig. 26b: Same as Fig. 26a, but for horizontal polarization.

In the near-grazing incidence case for the vertical polarization (Fig. 27a) the PO current gives a poor agreement with the MoM for all scattering angles. The GTD current results in an even worse approximation. The remaining procedures (UTD and nUTD) provide, on the other hand, very good agreement with the MoM. In the horizontal polarization case (Fig. 27b) the PO, GTD, and UTD currents give fairly close results, but all strongly disagree with the MoM. The nUTD provides a much better agreement.

We also note a very poor agreement of the GTD result for vertical polarization (Fig. 27a), due to the incorrect behavior of the GTD fields in the transition region (which, for near-grazing incidence, extends over a large area of the plate).

36
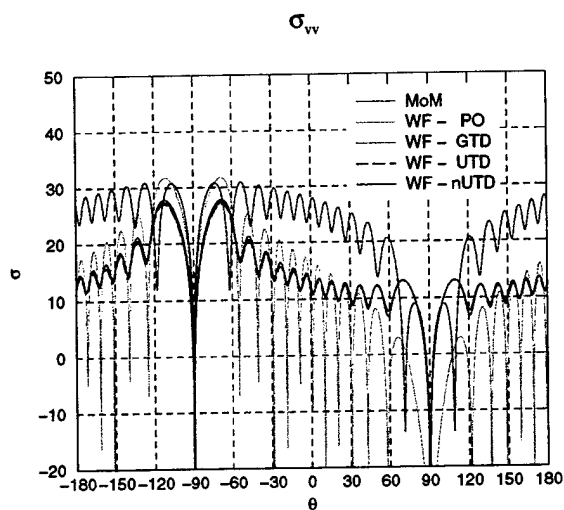
Fig. 27a: The differential bistatic cross section for the $6\lambda \times 6\lambda$ plate at near-grazing incidence ($\theta_i = 80°$) and for vertical polarization, computed by using the MoM and our current-based algorithm utilizing PO, GTD, UTD, and nUTD currents.
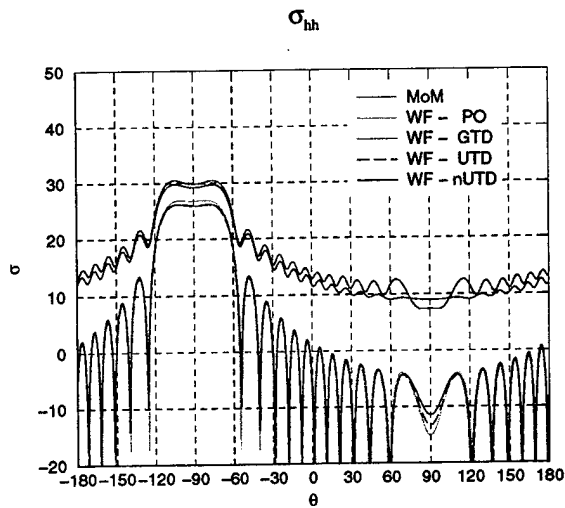
Fig. 27b: Same as Fig. 27a, but for horizontal polarization.

Results for the back-scattering cross-section are shown in Fig. 28. The features of the various approximations are here similar to those seen for bistatic cross-sections. We note, in addition, the discontinuity of the GTD vertical-polarization cross-section near $\theta = 90°$, due to the nonuniform behavior of the GTD diffraction coefficients in the transition region.
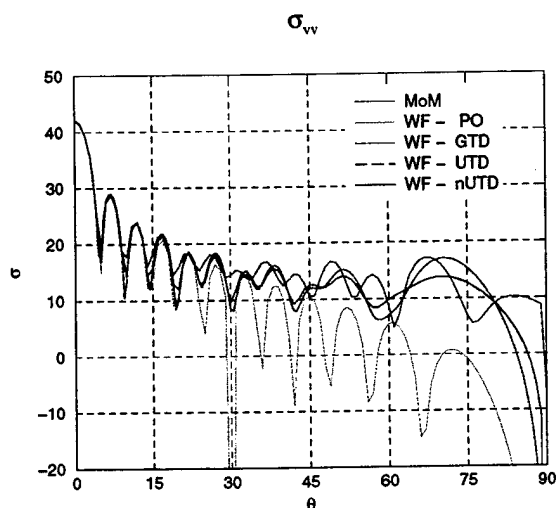
Fig. 28a: The differential back-scattering cross section for the $6\,\lambda \times 6\,\lambda$ plate, for vertical polarization, computed by using the MoM and our current-based algorithm utilizing PO, GTD, UTD, and nUTD currents.
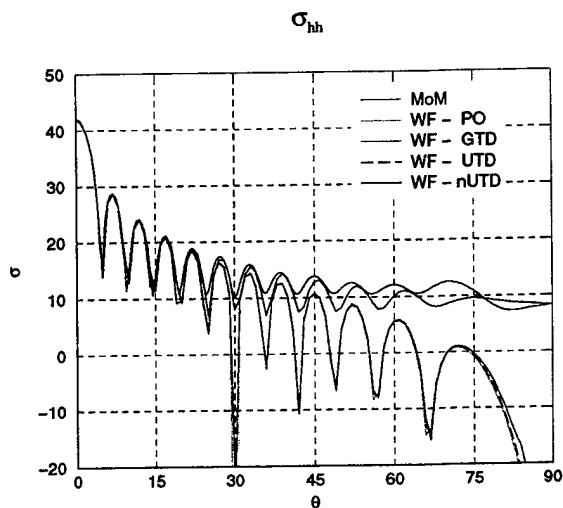
Fig. 28b: Same as Fig. 28a, but for horizontal polarization.

As a further illustration we show in Fig. 29a the distribution of the induced current $\mathrm{Re}\,J_x$ (computed using nUTD) for the case of the near-grazing incidence of Fig. 27b, with the v-polarized incident wave.
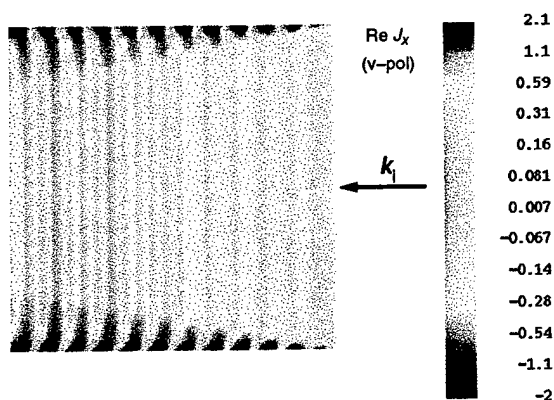
Fig. 29a: Distribution of the current component $\mathrm{Re}\,J_x$ for a v-polarized wave at the incidence angle $\theta_{\mathrm{i}} = 80°$.
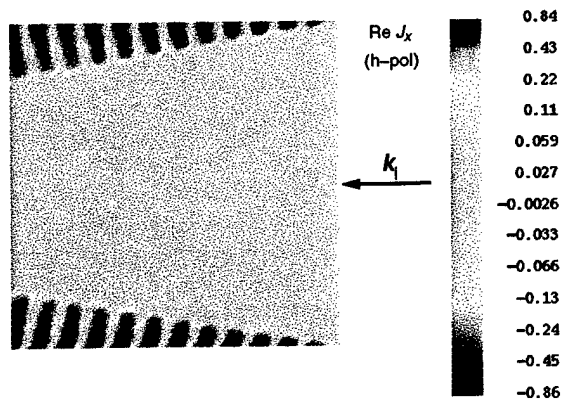
Fig. 29b: The same as Fig. 29a, but for an h-polarized incident wave.

The current J_x consists of the incident wave (PO) and diffraction contributions; the latter is mainly due to diffraction on the "trailing edge", and results in the enhancement (compared to PO) of the back-scattering cross-section at near-grazing angles, as seen in Fig. 28. (That enhancement is commonly termed the "surface wave" contribution.)

38

For comparison, Fig. 29b shows the distribution of the same current component as Fig. 29a, but for an h- (ϕ-) polarized incident wave. In this case the contributions to Re J_x come exclusively from diffraction on the edges parallel to the x-axis; it can be seen that the currents are nonzero only inside the relevant diffraction cones.

The features of the approximate cross-sections in Figs. 26 and 27 can also be understood by analyzing the behavior of the induced currents. In particular, the large difference between the nUTD and the remaining approximate results in Figs. 26b and 27b is due to the fact that only nUTD correctly reproduces the behavior of the currents flowing in the y-direction near the edges aligned with the y-axis.

We have analyzed many other cases of scattering on plates (for other cross-section cuts, and other incidence angles) and we found that the currents computed using nUTD consistently provide an improvement relative to both GTD and conventional UTD. Nevertheless, the agreement with the rigorous results is often not as good as that shown in Figs. 26 – 28.

There are many possible sources of disagreement between the MoM currents and currents evaluated using an asymptotic theory. We stress here that nUTD applied to a rectangular plate reproduces *exactly* the solutions of canonical (half-plane) problems for the four plate edges. Therefore, the most likely missing diffraction mechanism is *corner diffraction*, understood not only as a term in the asymptotic expansion of the Kirchhoff integral, but also as due to specific physical diffraction processes occurring in the presence of a corner. Unfortunately, the known solutions of the canonical problem (a plane angular sector) are only given as a rather complicated series of Lamé functions in the sphero-conal coordinate system [17, 18, 19]. For this reason, the corner diffraction problem has not yet been completely solved, although asymptotic forms of the corner-diffracted field (corner diffraction coefficients) have been obtained under some conjectures about the solution [20, 21], or for the rigorous solution in some special cases [22]. The latter work suggests that, physically, corner diffraction manifests itself mainly in the appearance of "edge wave currents" – waves emanating from the edges and propagating along the two edges forming the corner. We also observe such behavior in our MoM solutions for the currents.

We plan to analyze the problem of corner diffraction more thoroughly, and we expect that, as more complete calculations of corner diffraction coefficients become available, they will improve the agreement of the asymptotic theory with the rigorous results.

Diffraction on a system of rectangular plates

We discuss here our preliminary results for a system of two square plates: the plate A of size $10\lambda \times 10\lambda$, and the plate B of size $8\lambda \times 8\lambda$, located one above the other, as shown in Fig. 30. The plates are illuminated by a vertically incident v-polarized wave (with the electric field along the x-axis).
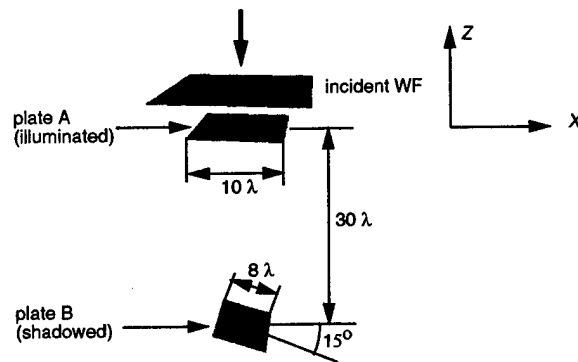
Fig. 30: A system of two plates (A and B) illuminated from above by an incident plane WF, so that plate B is in the shadow of plate A.

For this configuration, our present WF algorithm includes, as scattering mechanisms,

(a) reflection on plate A,

(b) diffraction on plate A,

(c) diffraction on plate A, reflection on plate B,

(d) diffraction on plate A, diffraction on plate B.

We evolve the WF through two relatively long steps. The first step creates WFs reflected and diffracted from the plate A (Fig. 31a). During the second step the diffracted wave arrives at the plate B and generates there secondary reflected and diffracted WFs (Fig. 31b).

(a)   (b)
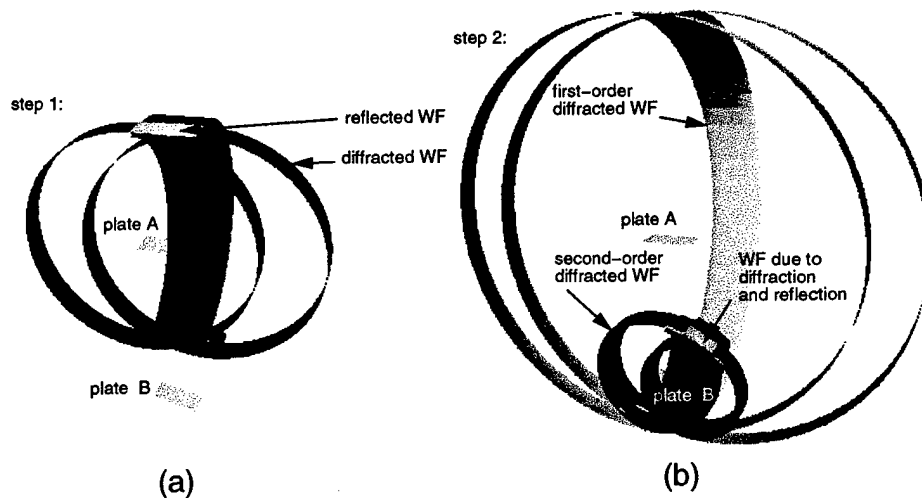
Fig. 31: WFs for the two-plate system after the first (a) and second (b) evolution steps. For clarity, the scatterer and the WFs are cut along the symmetry plane, and only one-half of the configuration is shown.

The scattered field is obtained by integrating the currents induced on both plates. The contribution to the cross-section resulting from the current on the plate B includes then effectively scattering mechanisms (c) and (d) listed above ((c) expected to be dominant). Since the plate B is

40

inclined, these processes are expected to generate a certain asymmetry in the cross-section, more specifically, an enhancement around $\theta = 30°$ due to reflection off the plate B. Indeed, some enhancement is seen in Fig. 32, where we compare the WF computation with the MoM result for plate A only and for both plates. However, compared to the rigorous (MoM) result, the enhancement is definitely too small.
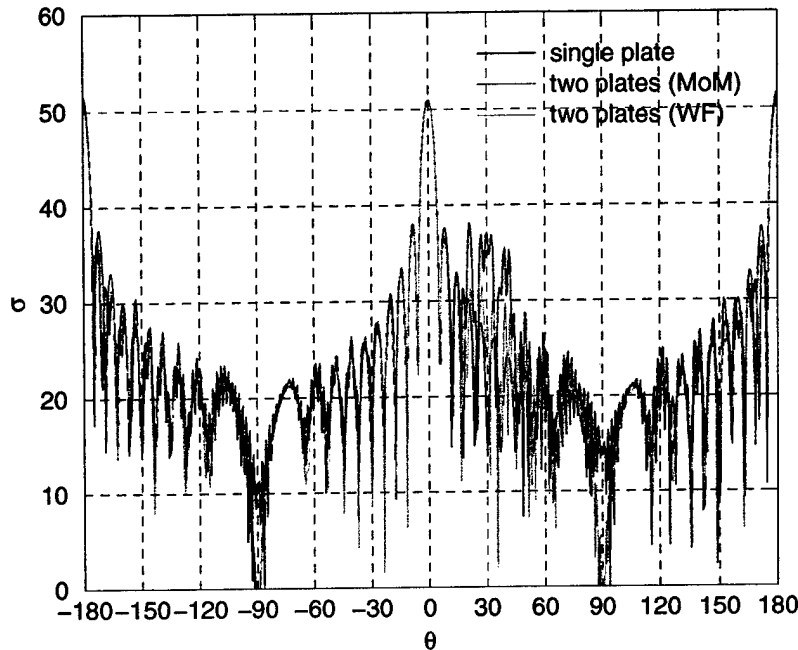
Fig. 32: The differential bistatic cross section (in dB, normalized to λ^2) for a single plate (plate A) and the system of two plates, computed by using the Method of Moments (MoM) and our WF evolution algorithm.

In Fig. 33 we compare current distributions on the plates, obtained using the MoM and our WF algorithm. Currents on the plate B show symmetric and rather intricate distributions; however, the WF computation definitely predicts too small currents there. That fact may be due to the lack of corner diffraction in our present WF algorithm.

We also note that the WF result shows no effect of plate B on the current distribution on A (while some effect is seen in the MoM current distribution). The reason is that in this particular computation the WFs reflected and scattered from plate B have not yet reached plate A (Fig. 31).
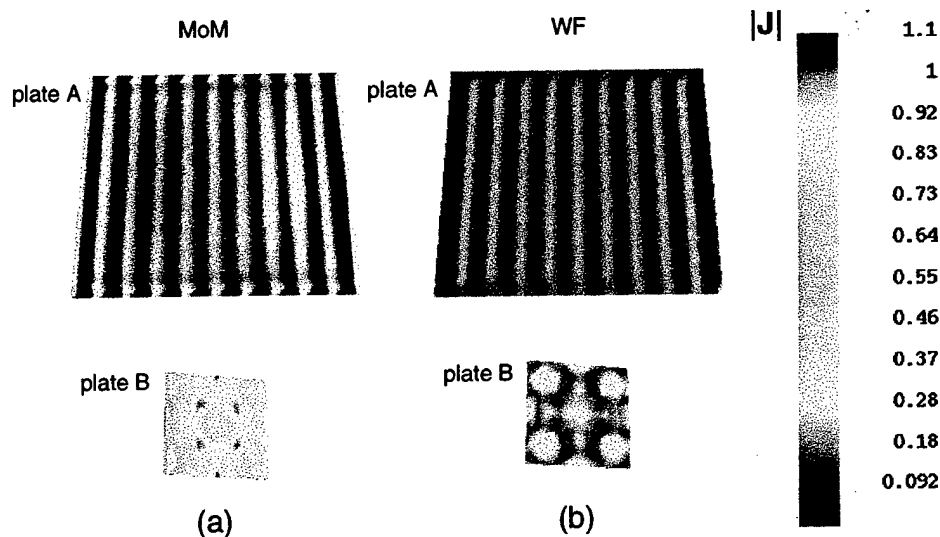
Fig. 33: Distributions of the absolute values of the induced current on the plates A and B, computed using the MoM (a) and our present WF evolution algorithm (b).

5. Algorithm elements requiring further development

When describing our WF algorithm we also mentioned its current inadequacies and shortcomings. Here we discuss improvements that can be introduced in the further algorithm development:

1. *Detection of diffraction edges.* As we described in Section 2, the present algorithm identifies diffraction edges by finding intersections of rays with scatterer faces. This procedure is not applicable in the case when the rays are exactly tangential to the (flat) scatterer surface – a situation arising in multiple diffraction on a flat screen or on a polyhedral scatterer. The present algorithm may also miss edges of very thin wedges, it the wedge width is less than the typical ray-ray spacing h.

   A remedy to these problems is to preprocess the scatterer geometry and mark all edges that may be sources of diffraction. Then, in the WF evolution process we can check proximity of the rays to the marked edges, by effectively testing ray intersections with cylinders built around the edges (the cylinder radius being comparable to the minimal ray-ray spacing). This algorithm modification corrects also the problem of missing small end parts of the WF (Fig. 15).

2. *Detection of corners.* The present algorithms, both for reflections and diffraction, detects edges of scatterer faces by testing intersections of rays with faces, and creates new rays hitting the detected edges by interpolating between existing rays along the edges of the WF mesh. While this procedure works well for sufficiently smooth edges, it may result, in the vicinity of sharp corners, in localization errors of order of the ray-spacing.

   This algorithm deficiency can also be corrected by localizing corners in the geometry preprocessing stage, and then testing ray intersections with spheres centered at the corners.

3. **Multiple reflections and diffractions in a single evolution step.** The present algorithm implements partially multiple ray reflections in a single evolution step, but does not allow computation of induced currents in this situation. Neither does it allow multiple diffraction in a single step. The difficulty in algorithm implementation stems from the fact that neighboring rays may undergo different numbers of reflections or diffractions, i.e., have different evolution histories; such as situation precludes straightforward field interpolation required in evaluation of the current.

   To correct this deficiency, we plan to modify the description of ray evolution between the consecutive WFs: instead of evolving individual rays, we will evolve *ray tubes*, a ray tube being a triplets of rays constituting vertices of a WF mesh face. In a multiple reflection or diffraction process these ray tubes will be split, until all rays in a given tube have the same evolution history, and interpolation becomes possible.

4. **Continuity of the diffracted WF generated in consecutive evolution steps.** In the present algorithm implementation there may appear gaps between the segments created in consecutive evolution steps (Fig. 16).

   This problem can be also corrected by describing ray evolution in terms of ray tubes rather than individual rays. In this context a ray tube provides an additional connectivity information, and "memory" preserved between the evolution steps.

Other algorithm modifications are extensions to include additional scattering mechanisms:

5. **Corner and tip diffraction.** These diffraction mechanisms can be implemented in conjunction with the corner detection procedure mentioned in point 2. However, as we discussed in Section 2, the corner and tip diffraction coefficients are presently available only for some special cases, or in approximate forms.

6. **Gap and crack diffraction.** Although these processes can be, in principle, described as multiple diffraction, it will be more convenient and economical to model them as separate diffraction mechanisms characterized by specific diffraction coefficients [23].

7. **Smooth-surface diffraction.** Diffraction on smooth surfaces constitutes a major extension of the present algorithm. We have developed a general idea of the smooth-surface diffraction algorithm, involving splitting of "ray tubes" incident on the scatterer surface near the shadow boundary. Its implementation would be, however, rather complex.

8. **Treatment of caustics.** Problems associated with caustics in the scattered field have been partly alleviated by utilizing the procedure of evaluating radar signatures from surface currents. Caustics, however, may also appear on the surface of the scatterer. In that case it might be necessary, in the last diffraction process, to avoid using the stationary-point approximation altogether, and describe the diffraction process in terms of one of "incremental" diffraction theory approaches [24, 25, 23, 26, 27].

In addition, performance of the present, preliminary, algorithm implementation is inadequate, and has to be improved in at least two areas:

9. **WF mesh complexification and simplification.** Improvement of this algorithm is relatively straightforward. It requires performing operations on the WF mesh in a way as local as possible, i.e., only in regions where the mesh has been modified or has to be modified.

10. *Current computation.* Efficiency requires that the present algorithm (Sections 3.2 and 3.3) be thoroughly revised. We plan to reverse the procedure by finding current points contained in specific ray cells, rather than finding ray cells containing specified current points.

6. Assessment of the Phase I results

As the main result of the Phase I effort, we developed and constructed preliminary implementations of the following algorithms:

1. Algorithm for free-space WFs evolution.
2. Algorithm for creating WFs according to the laws of Geometrical Optics (GO), and for evaluating fields due to GO processes.
3. Algorithm for creating geometry of the WFs due to edge diffraction according to prescriptions of the Geometrical Theory of Diffraction
4. Algorithm for evaluating fields due to edge diffraction, according to a modified version of Uniform Geometrical Theory of Diffraction (UTD).
5. Algorithm for direct evaluation of scattered fields in terms of WF fields.
6. Algorithm for evaluating surface currents based on the computed WF field values.

The algorithms for geometrical WF construction are applicable in both frequency and time domains. Our current implementation of UTD field computation algorithms has been carried out in frequency domain; it can be, however, extended to time domain in a rather straightforward way by incorporating the time-domain UTD being developed at the ElectroScience Laboratory of Ohio State University [28, 29, 31, 32].

The modification of UTD mentioned in point 4, in its present implementation, provides the correct behavior of diffracted fields at all distances (including those small compared with the wavelength) for screen-edge problems. By a correct behavior we mean here coinciding with the exact solution for the corresponding canonical problem, in this case the half-plane. The construction can be generalized in a straightforward way to the perfectly conducting wedge problem [1].

As another comment, relevant to the point 6, we mention that computation of surface currents may either yield the scattered fields (in a more general and robust way than the direct evaluation mentioned in point 5), or, alternatively, it can be used to construct a solution Ansatz to be subsequently used in solving rigorous asymptotic high-frequency integral equations [2, 3]. We stress that in the latter application only the geometrical construction of WF and rays is involved, and we avoid difficulties associated with the computation of field values (such as caustics).

The description of our WF approach, presented in this report, indicates that many aspects of the algorithm are fairly complex both in formulation and in implementation. Also, as we discussed in the preceding Section, many algorithm elements require further development and substantial modifications. Nevertheless, the results obtained confirm the two most important features of our approach:

(i) correct high-frequency scaling (number of rays and thus computational cost independent of frequency); and

44

(ii) algorithm ability to treat multiple reflections and diffraction in a consistent way (in agreement with reciprocity).

In view of these findings, we believe that the Phase I results do provide a solid basis for development of an efficient software package capable of consistent and accurate modeling of a wide variety of high-frequency electromagnetic scattering processes. It would constitute a significant improvement compared to presently available codes which typically do not incorporate features (i) and (ii) just mentioned.

7. References

1. E. Bleszynski, M. Bleszynski, and T. Jaroszewicz, "Uniform asymptotic solution for near fields in edge diffraction", paper in preparation.

2. O. Bruno, A. Sei, and M. Caponi, "High-order high-frequency solutions for rough surface scattering problems", Caltech preprint, 2000, submitted to *J. Comput. Phys.*.

3. E. Bleszynski, M. Bleszynski, and T. Jaroszewicz, "Development of new algorithms for high frequency electromagnetic scattering", to appear in *CMES Journal*, 2003.

4. V. Vinje, E. Iversen, and H. Gjöystdal, "Traveltime and amplitude estimation using wavefront construction", *Geophysics*, Vol. 58, pp. 1157-1166, 1993.

5. V. Vinje, E. Iversen, K. Astebol, and H. Gjöystdal, "Estimation of multivalued arrivals in 3D models using wavefront construction - Part I", *Geophysical Prospecting*, Vol. 44, pp. 819-842, 1996.

6. V. Vinje, E. Iversen, K. Astebol, and H. Gjöystdal, "Estimation of multivalued arrivals in 3D models using wavefront construction - Part II", *Geophysical Prospecting*, Vol. 44, pp. 843-858, 1996.

7. G. Lambare, P.S. Lucio, and A. Hanyga, "Two-dimensional multivalued traveltime and amplitude maps by uniform sampling of a ray field", *Geophys. J. Internet*, Vol. 125, pp. 584-598, 1996.

8. S. Hildebrand, C. Aprea, and M. Fehler, "Wavefront construction: a differential geometry approach", 69th SEG Meeting Expanded Abstracts, Houston, 1999.

9. J. Steinhoff, M. Fan, and L. Wang, "A new Eulerian method for the computation of propagating short acoustic and electromagnetic pulses", *J. Comput. Phys.*, Vol. 157, pp. 683-706, 2000.

10. S.J. Ruuth, B. Merriman, and S. Osher, "A fixed grid method for capturing the motion of self-intersecting interfaces and related PDEs", *J. Comput. Phys.*, Vol. 163, pp. 1-21, 2000.

11. S. Osher and R.P. Fedkiw, "The level set method and dynamic implicit surfaces", Springer Verlag, New York, 2002.

12. J.B. Keller, "Geometrical theory of diffraction", *J. Opt. Soc. Am.*, Vol. 52, pp. 116-130, 1962.

13. J.B. Keller, "Diffraction by an aperture", *J. Appl. Phys.*, Vol. 28, pp. 426-444, 1957.

14. R.G. Kouyoumjian and P.H. Pathak, "A uniform geometrical theory of diffraction for an edge in a perfectly conducting surface", *Proc. IEEE*, Vol. 62, pp. 1448-1461, 1974.

15. P.H. Pathak, W.D. Burnside, and R.J. Marhefka, "A uniform GTD analysis of the diffraction of electromagnetic waves by a smooth convex surface", *IEEE Trans. Antenn. Propagat.*, Vol. AP-28, pp. 631-642, 1980.

16. G.L. James, "Geometrical theory of diffraction for electromagnetic waves", Peter Peregrinus Ltd., London, 1986.

17. R.S. Satterwhite, "Diffraction by a plane angular sector", Ph.D. dissertation, Dept. of Electrical Engineering, Ohio State Univ., Columbus, Ohio, 1969.

18. R.S. Satterwhite, "Diffraction by a quarter plane, the exact solution, and some numerical results", *IEEE Trans. Antenn. Propagat.*, Vol. AP-2, pp. 500-503, 1974.

19. T.B. Hansen, "Diffraction by a plane angular sector, a new derivation", *IEEE Trans. Antenn. Propagat.*, Vol. AP-38, pp. 1892-1894, 1990.

20. F.A. Sikta, W.D. Burnside, T.T. Chu, and L. Peters, Jr., "First-order equivalent current and corner diffraction scattering from flat plate structures", *IEEE Trans. Antenn. Propagat.*, Vol. AP-31, pp. 584-589, 1983.

21. K.C. Hill, "A UTD solution to the EM scattering by the vertex of a perfectly conducting plane angular sector", Ph.D. dissertation, Dept. of Electrical Engineering, Ohio State Univ., Columbus, Ohio, 1990.

22. T.B. Hansen, "Corner diffraction coefficients for the quarter plane", *IEEE Trans. Antenn. Propagat.*, Vol. AP-39, pp. 976-984, 1991.

23. R.A. Shore and A.D. Yaghjian, "Incremental diffraction coefficients for planar surfaces", *IEEE Trans. Antenn. Propagat.*, Vol. AP-36, pp. 55-70, 1988; and "Corrections to 'Incremental diffraction coefficients for planar surfaces'", *IEEE Trans. Antenn. Propagat.*, Vol. AP-37, pp. 1342, 1989.

24. K.M. Mitzner, "Incremental length diffraction coefficients", *Tech. Rep. AFAL-TR-73-296*, Northrop Corporation, Aircraft Division, April 1974.

25. R. Tiberio, S. Maci, and A. Toccafondi, "An incremental theory of diffraction: electromagnetic formulation", *IEEE Trans. Antenn. Propagat.*, Vol. AP-43, pp. 87-96, 1995.

26. A.D. Yaghjian, R.A. Shore, and M.B. Woodworth, "Shadow boundary incremental length diffraction coefficients for perfectly conducting smooth, convex surfaces", *Radio Sci.*, Vol. 32, p. 673, 1997.

27. R.A. Shore and A.D. Yaghjian, "Shadow boundary incremental length diffraction coefficients applied to scattering from 3-d bodies", *IEEE Trans. Antenn. Propagat.*, Vol. AP-49, pp. 200-210, 2001.

28. P.R. Rousseau and P.H. Pathak, "Time-domain uniform geometrical theory of diffraction for a curved wedge", *IEEE Transactions on Antennas and Propagation*, Vol. 43, pp.1375-1382, 1995.

29. P.R. Rousseau and P.H. Pathak, "A time domain uniform geometrical theory of slope diffraction for a curved wedge", (invited paper) *Turk. J. Elec. Engin.*, Vol. 10, pp. 385-398, 2002 (Special Issue).

30. P.R. Rousseau, P.H. Pathak, and H.-T. Chou, "A TD-UTD for diffraction by a perfectly conducting, arbitrary smooth convex surface", paper in preparation.

31. H.-T. Chou, P.H. Pathak, and P.R. Rousseau, "A TD-UTD for the transient radiation by pulsed antennas on a perfectly conducting, arbitrary smooth convex surface", paper in preparation.

32. H.-T. Chou, P.H. Pathak, and P.R. Rousseau, "A TD-UTD for transient mutual coupling between pulsed antennas on a perfectly conducting, arbitrary smooth convex surface", paper in preparation.

Some Frequency and Time Domain Ray Solutions for Use in a Wavefront Evolution Algorithm for the Efficient Analysis of Large Electromagnetic Problems

P.H. Pathak and K. Tap
The Ohio State University

ElectroScience Laboratory

Department of Electrical Engineering
1320 Kinnear Road
Columbus, Ohio 43212

5027272-101

REPORT DOCUMENTATION PAGE	1. REPORT NO.	2.	3. Recipient's Accession No.
4. Title and Subtitle Some Frequency and Time Domain Ray Solutions for use in a Wavefront Evolution Algorithm for the Efficient Analysis of Large Electromagnetic Problems			**5. Report Date** November 2002
			6.
7. Author(s) P.H. Pathak and K. Tap			**8. Performing Org. Rept. No.** 742135
9. Performing Organization Name and Address The Ohio State University ElectroScience Laboratory 1320 Kinnear Road Columbus, OH 43212			**10. Project/Task/Work Unit No.**
			11. Contract (C) or Grant (G) No. (C) Contract No. AFO1T0009
12. Sponsoring Organization Name and Address Monopole Research 739 Calle Sequoia Thousand Oaks, CA 91360			**13. Report Type/Period Covered** Final Report
			14.

15. Supplementary Notes

16. Abstract (Limit: 200 words)

Some basic frequency domain based uniform geometrical theory of diffraction (FD-UTD) and corresponding time domain (TD-UTD) solutions are briefly reviewed. These solutions have been chosen initially for implementation within the Wavefront Evolution (WE) algorithm being developed by Monopole Research for efficiently analyzing electromagnetic radiation, scattering and coupling problems associated with relatively large complex structures of practical interest. The UTD ray solutions involve the edge and slope edge diffraction by curved wedges, as well as the scattering, radiation and mutual coupling associated with smooth convex surfaces, respectively. The FD-UTD solutions have been obtained in the past. Also, the TD-UTD solutions, except for the last two cases, have been developed more recently. However, the TD-UTD for the last two cases constitute new solutions which have been completed under the present contract.

17. Document Analysis

a. Descriptors

b. Identifiers/Open-Ended Terms

c. COSATI Field/Group

18. Availability Statement Approved for public release; distribution is unlimited	**19. Security Class (This report)** Unclassified	**21. No. of Pages** 54
	20. Security Class (This page) Unclassified	**22. Price**

(See ANSI-Z39.18) *See Instructions on Reverse* OPTIONAL FORM 272 (4-77)
Department of Commerce

ii

1. Introduction

This report provides a brief summary of the technical support made available by the Ohio State University ElectroScience Lab (OSU-ESL), to Monopole Research in their development of a Wavefront Evaluation (WE) Algorithm for the efficient ray based analysis of electromagnetic (EM) radiation and scattering from electrically large objects of practical interest.

Part of these contributions involved providing Monopole Research with some basic and important ray field expressions based on the uniform geometrical theory of diffraction (UTD) [1-3], and also providing associated computer subroutines for calculating these field expressions within the WE algorithm. The UTD solutions which have been provided are in the frequency domain (FD), as well as in the time domain (TD). Thus, both FD-UTD and TD-UTD type solutions and their associated subroutines have been included in this work. Additionally, two new TD-UTD solutions have been developed which are expected to be particularly useful in electromagnetic compatibility (EMC) and electromagnetic pulse (EMP) applications; however, the computer subroutines for calculating the TD-UTD fields in these two new cases have not been written as yet in a user friendly manner. It is hoped that the latter, as well as additional FD-UTD and TD-UTD solutions of importance (some of which have not been developed to date) could be included within the WE framework in the future phases of this study.

The WE algorithm [4], which is being developed by Monopole Research, will allow one to track ray fields more efficiently than via other commonly used ray shooting methods. This is possible because in the WE approach, one simultaneously tracks a grid of rays rather than tracking a single ray at a time. The latter is possible since the WE method exploits the intimate relation between a family of rays and their associated wavefront. In a numerical sense, a discrete set of rays can be employed to approximately define a wavefront patch, and vice versa. Once an initial wavefront patch is chosen on the illuminating or incident field, one can then track this initial wavefront (or phasefront) patch as it evolves via reflection and/or diffraction from the radiating /scattering object, to arrive at observer locations of interest. The completion of the EM solution to the radiation, scattering and diffraction of waves from electrically large complex objects via the WE approach then requires one to assign field values to the discrete rays defining a

3

wavefront patch, as the latter evolves in a given problem configuration. The set of wavefront patches defining the part of the incident or excitation wavefront that interact with the radiating/scattering object must satisfy certain connectivity requirements. In this regard, it is noted that the wavefront patches could split at sharp edges due to the process of diffraction. The sum total of the fields associated with all the discrete set of rays on each of the patches as they evolve finally provides the required solution. Of course one may need to interpolate field values between the discrete set of adjacent rays in order to have a knowledge of the field at any point on the wavefront patch or patches. Since a discussion of the WE approach may be found in [4], the present report will focus on briefly describing some of the types of ray fields that need to be coupled into the WE algorithm during the initial phases of its development. Other types of ray fields may be included during later phases of this study to make the WE algorithm more versatile. Specifically, the type of ray fields considered for use in the initial WE algorithm being prepared by Monopole Research are those that are needed to account for some of the basic first order diffraction mechanisms that are generally present in large complex structures which can be built up from a combination of smooth convex surfaces and edges. The ray field expressions, and their associated computer subroutines which have been delivered to Monopole Research for calculating such ray fields are based on the UTD [1-3] as stated earlier. The UTD extends the original geometrical theory of diffraction (GTD) [5] to avoid the singularities of the GTD fields at the ray optical shadow boundaries. The accuracy and efficiency of the FD-UTD has been established over the last two decades via numerous scale model measurements and other independent approaches. On the other hand, the TD-UTD is a recent development [6,7]. A TD-UTD solution is generally obtained by inverting the corresponding FD-UTD solution which is assumed to be available. The analytical inversion of the FD-UTD into the TD-UTD is accomplished via the Analytic Time Transform (ATT) [6,9] which has many useful properties that make it particularly attractive for inverting ray solutions from the frequency to time domain. The latter properties of the ATT are also discussed in [6,7].

The motivation for the TD-UTD development stems from several factors some of which are enumerated as follows. Exact TD solutions are available only for a handful of relatively simple radiating objects/configurations. Furthermore, it is more natural to study

4

transient EM wave phenomena directly in the time domain as opposed to a less physically appealing and less efficient numerical inversion of the frequency domain solutions into the time domain via the Fast Fourier Transform (FFT) Algorithm. Since TD-UTD solutions employ the same rays as the FD-UTD, it retains and therefore exhibits the same advantages as the well established FD-UTD; namely, the TD-UTD is expected to remain relatively simple to use and also provide a simple ray picture for EM radiation and scattering. Hence, the TD-UTD has the potential, when developed to the same extent as the FD-UTD, to efficiently solve large, complex problems for which exact analytical solutions may not be possible. While the FD-UTD offers localization of wave effects in space via the use of rays, the TD-UTD offers localization of wave effects in both space and time via space-time rays which traverse the same paths as the FD-UTD rays. The latter could make the TD-UTD approach useful in target identification (ID) application as well; in this regard, one notes that the time domain data needed for target ID studies is expected to be less affected by noise than the frequency domain data.

The FD-UTD solutions (and associated computer subroutines) which have been provided for integration into the WE algorithm in order to describe some basic and important wave diffraction mechanisms are enumerated in section 2.1. All the corresponding TD-UTD solutions (and their associated computer subroutines) , which have also been provided for integration into a time domain version of the WE analysis of the radiation and scattering of EM waves from large complex structures, are enumerated next in section 2.2. It is noted that computer subroutines for all but two of the TD-UTD mechanisms are not available for integration into the WE algorithm at this time, because the development of these latter two TD-UTD solutions have only recently been completed as discussed in section 3 dealing with new TD-UTD solutions. The computer subroutines for the latter two new TD-UTD solutions will be submitted to Monopole Research in future phases of this study since they are presently not in a user friendly form.

An $e^{+j\omega t}$ time convention is assumed and suppressed for all the FD-UTD fields discussed below.

2. Brief Description of FD-UTD and TD-UTD Fields for Implementation in the initial WE Algorithm

In general, a UTD ray analysis of the radiation/scattering from complex structures gets broken down into a set of simpler events such as incidence, reflection and diffraction which may be calculated in terms of fields that propagate along ray paths, in a sequential manner, from the source to the observer via these events on the complex structure. The actual incident, reflection and diffraction events are often referred to as occurring at flash points on the radiating/scattering object. To a first order of ray interactions, these flash points are points of reflection and diffraction on the structure; these exist in addition to direct rays from the source to the observer. It is assumed in the present work that the structure is impenetrable and perfectly–conducting. Other multiple ray interactions such as multiple reflection, reflection-diffraction effects, and multiple diffraction effects can also be calculated within the UTD framework; however, a discussion of the latter is not presented here for it is addressed in [10] for the FD-UTD. Multiple effects (other than multiple reflection) have not been analyzed yet within the TD-UTD framework and hence such a study also forms a topic of future investigation to elevate TD-UTD to the same level of applicability as the FD-UTD. The points of reflection that are considered in this work are associated with such points when they occur on smooth surfaces that may terminate at edges, while diffraction points are allowed to be on edges and at grazing incidence on smooth convex surfaces, respectively.

2.1 FD-UTD for Edge and Surface Diffraction

As stated above, a brief summary of the relevant FD-UTD based ray field expressions that are to be incorporated initially into the WE algorithm is given here. These expressions allow one to solve the radiation/scattering of EM waves by objects that can be built up from a contribution of arbitrary smooth convex surfaces, and curved surfaces containing arbitrary curved edges. Many practical shapes fall into this category of objects which can be modeled as a collection of curved surfaces and edges (e.g. aircraft, missile, satellite structures, etc.). Other important effects which can involve diffraction from tips (or corners), coupling between edge and smooth surface diffraction, double diffraction, diffraction by non-conducting surfaces etc. also need to be considered; however, the latter can be incorporated during the future phases of the WE algorithm development.

First, the edge diffraction effect is summarized, and then the smooth convex surface diffraction effect is treated likewise.

2.1.1 FD-UTD for Edge Diffraction

The geometry for edge diffraction is shown in Fig.1, where a source illuminates an arbitrary curved wedge which is assumed here to be perfectly conducting.
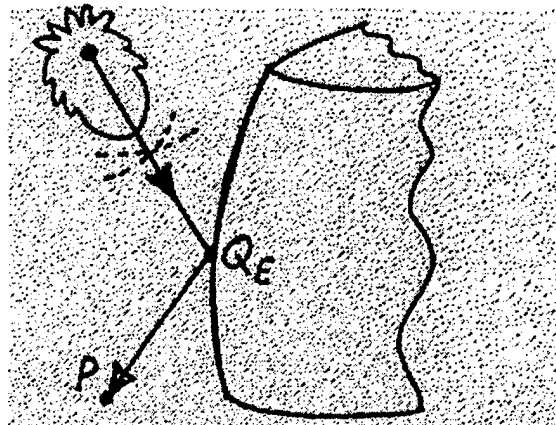
Fig.1 : Diffraction by an Arbitrary Curved PEC Wedge

In Fig.1, the pattern of the source/antenna is assumed to be relatively slowly varying at the point of edge diffraction. A corresponding ray tube picture illustrating how a small incident wavefront patch can transform into a edge diffracted wavefront patch is shown in Fig.2. The edge diffracted rays lie on the Keller cone of diffracted rays as is well

known [5,1]. The Keller law of edge diffraction states that the half angle of the Keller cone of edge diffraction at any point of edge diffraction, Q_E exactly equals the angle that the incident ray makes with the edge tangent at Q_E. Thus, $\beta_0 = \beta_0'$ as shown in Fig.2.

$$s_0^d = |\overline{P_0P}|$$
$$s^d = |\overline{Q_EP}|$$

$$(\beta_0' = \beta_0)$$
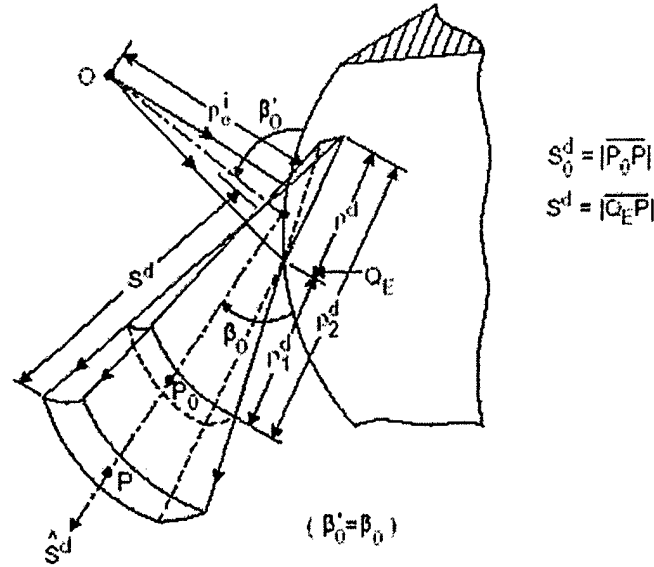
Fig.2 : Edge-diffracted ray tube. Radius of the incident wavefront where it intersects the edge = ρ_e^i

The electric field at a point P anywhere on the Keller cone at a distance s^d from Q_E, where $ks^d >> 1$ and k = wave number of free space which surrounds the curved wedge, is given by

$$\overline{E}^d(P) \approx \overline{E}^i(Q_E) \cdot \overline{\overline{D}} A(s^d) \ e^{-jks^d} \tag{1}$$

In (1), the $\overline{E}^d(P)$ and $\overline{E}^i(Q_E)$ represent the edge diffracted electric field at P, and the incident electric field at Q_E, respectively. The UTD coefficient for edge diffraction is denoted by $\overline{\overline{D}}$ [1,3] and it depends on the frequency of the incident wave as well as the angles of incidence and diffraction, and also the incident wave polarization as discussed in [1-3]. $A(s^d)$ is the spatial spread, (or divergence) factor of the edge diffracted ray (from Q_E to P) which indicates how the energy spreads in space after diffracting from the edge. $A(s^d)$ can also be obtained from a conservation of power in a diffracted ray tube; this conservation law is valid outside the incident and reflected ray shadow boundary transition regions [   ]. The $\overline{\overline{D}}$ contains Fresnel transition functions which not only keep

$\overline{\overline{D}}$ bounded, but also provide the $\overline{\overline{D}}$ with the appropriate behaviour to keep the total high frequency field continuous at the shadow boundaries where the geometrical optics incident and reflected fields become discontinuous The latter discontinuity results from the shadow boundaries for the incident and reflected rays, which are created by the presence of the edge (in a perfectly conducting or non-penetrable surface).
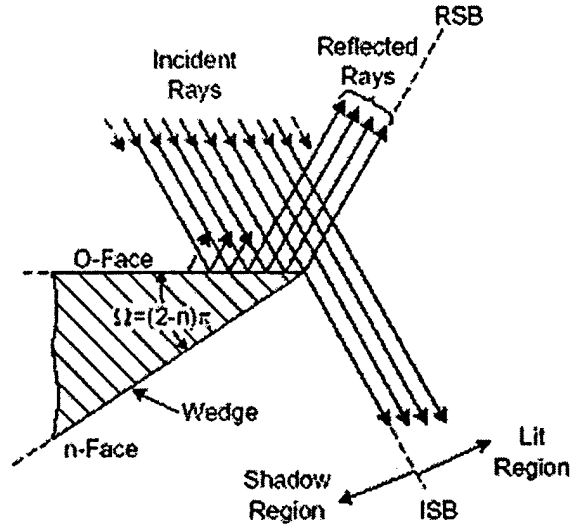
Fig.3 : Incident and Reflection Shadow Boundaries ISB and RSB, respectively for diffraction by a PEC wedge illuminated by a plane wave

Fig.3 illustrates these shadow boundaries for a simple wedge configuration when it is illuminated by an incident plane wave. A boundary layer exists adjacent to the shadow boundaries and it is referred to as a transition region whose size (or angular extent on either side of the boundaries) depends on the frequency as well as the source and observer locations[1-3]. The transition region becomes smaller with increase in frequency. The Fresnel integrals within $\overline{\overline{D}}$ play an important role within the incident and reflection shadow boundary transition regions to keep $\overline{\overline{D}}$ uniformly valid across these shadow boundaries.

In (1), the s^d denotes the distance from Q_E to P (i.e. $s^d = \left| \overline{Q_E P} \right|$) as in Fig.2. If the edge is curved so that the edge radius of curvature is negative (concave rather than convexly curved edge), then the diffracted rays can go through a diffracted ray caustic before arriving to P. Also, the field incident on the edge at Q_E need not arrive from a distant antenna (here shown by a point source with a pattern), but more generally it can

9

represent an incident wavefront (created possibly by an earlier reflection or diffraction elsewhere in the case of a previous interaction before arriving to Q_E). Consequently, the incident wavefront could arrive at Q_E after passing through one or more caustics. For the case when there is a diffracted ray caustic between Q_E and P, the $A(s^d)$ becomes

$$A(s^d) = |A(s^d)| \ j^{n^d} \qquad (2)$$

where n^d is the number of caustics between Q_E and P with $j = \sqrt{-1}$. Typically, $n^d = 1$.

Also, e^{-jks^d} is the exponential phase delay along the diffracted ray propagation path from Q_E to P. Since the details on the derivation of $\overline{\overline{D}}$ in (1) are available in [1], no further discussion on the $\overline{\overline{D}}$ is provided here. It is noted that the subroutines required to calculate $\overline{\overline{D}}$ for edge diffraction have been made available to Monopole Research. Finally, it is noted that the magnetic field along the diffracted ray at P can be found via local plane wave conditions, $\overline{H}^d(P) \approx Y_0 \hat{s}^d \times \overline{E}^d$

where $Y_0 = Z_0^{-1}$ and $Z_0 =$ intrinsic free space wave impedance.

2.1.2 FD-UTD for Slope Edge Diffraction
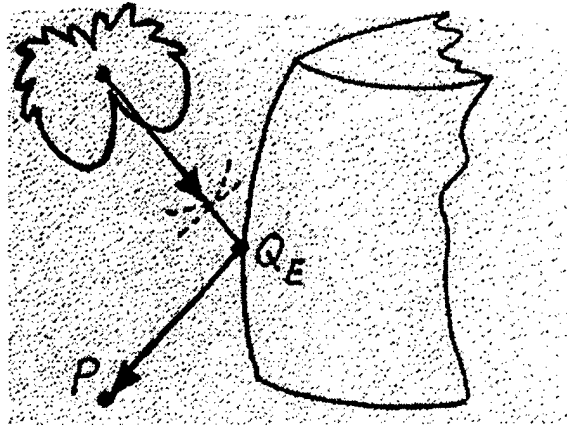
Fig. 4 : Slope Diffraction by an Arbitrary Curved PEC Wedge

When the incident field is rapidly varying at any point of edge diffraction, Q_E as shown in Fig. 4, then the result in (1) for $\overline{E}^d(P)$ must be augmented by a slope

diffracted field contribution $\overline{E}^{sd}(P)$. The $\overline{E}^{sd}(P)$ is required to make the slope of the total field continuous across incident and reflection shadow boundaries, because $\overline{E}^{d}(P)$ is valid only for non-rapidly varying incident fields at Q_E. One notes that (1) can be expressed in matrix form as

$$
\begin{bmatrix} E^d_{\beta_0} \\ E^d_{\phi} \end{bmatrix} = \begin{bmatrix} -D_s & 0 \\ 0 & -D_h \end{bmatrix} \begin{bmatrix} E^i_{\beta_0}{}' \\ E^i_{\phi'} \end{bmatrix} A(s^d)\ e^{-jks^d} \tag{3}
$$

where the incident and diffracted fields are expressed in terms of unit vectors fixed in the incident and diffracted rays, and in particular in the edge fixed planes of incidence and diffraction as defined in [1-3]. One employs these special set of unit vectors so that $\overline{\overline{D}}$ then reduces to a two term dyad [1]. Thus,

$$
\overline{E}^d(P) = \hat{\beta}_0 E^d_{\beta_0} + \hat{\phi} E^d_\phi \quad ; \quad \hat{\beta}_0 \times \hat{\phi} = \hat{s}^d \tag{4}
$$

$$
\overline{E}^i(P) = \hat{\beta}_0{}' E^i_{\beta_0}{}' + \hat{\phi}'\ E^i_{\phi'} \quad ; \quad \hat{\beta}_0{}' \times \hat{\phi}' = \hat{s}^i \quad , \tag{5}
$$

$$
\overline{\overline{D}} = -\hat{\beta}_0{}' \hat{\beta}_0\ D_s - \hat{\phi}'\hat{\phi}\ D_h \tag{6}
$$

One notes that the $(\hat{\beta}_0, \hat{\phi})$ are perpendicular to each other and to $\hat{s}^d$, while $(\hat{\beta}_0', \hat{\phi}')$ are perpendicular to each other and to the incident ray direction, $\hat{s}^i$.

The slope diffracted field $\overline{E}^{sd}(P)$ for a perfectly conducting wedge can be expressed more conveniently in matrix form as

$$
\begin{bmatrix} E^{sd}_{\beta_0} \\ E^{sd}_{\phi} \end{bmatrix} = \begin{bmatrix} -D^{si}\dfrac{\partial}{\partial n^i} E^i_{\beta_0}{}' & -D^{sr}_s \dfrac{\partial}{\partial n^r} E^r_{\beta_r}{}' \\ -D^{si}\dfrac{\partial}{\partial n^i} E^i_{\phi'} & -D^{sr}_h \dfrac{\partial}{\partial n^r} E^r_{\phi_r}{}' \end{bmatrix} A(s^d)\ e^{-jks^d} \tag{7}
$$

Again, the unit vectors $\hat{\beta}_0{}'$, $\hat{\beta}_0, \hat{\phi}'$ and $\hat{\phi}$ are as defined in [1], whereas, $\hat{\beta}_r'$ and $\hat{\phi}_r'$ are the corresponding unit vectors fixed on the reflected ray and in the edge fixed plane of reflection as defined in [1]. Also, the slope diffraction coefficients D^{si}, D^{sr} and D_h^{sr} are defined in [2]; they contain slope transition functions that are of the type

$$
2jx(1 - F(x)) \tag{8}
$$

where the ordinary transition function *F(x)* occurs directly in the ordinary UTD edge diffraction coefficient $\overline{\overline{D}}$ (or in D_s and D_h, respectively). Here *F(x)* contains the Fresnel integral alluded to earlier; in particular,

$$F(x) = 2j\sqrt{x}\ e^{jx} \int\limits_{\sqrt{x}}^{\infty} e^{-j\tau^2} d\tau \tag{9}$$

Within the transition region x is small and close to the shadow boundary so $F(x) \approx \sqrt{\pi j x}$, whereas outside the transition region x is large (usually x>3) so that $F(x) \cong 1$. More details on this slope diffracted field $\overline{E}^{sd}$ may be found in [2] and also in Appendix 1. Also, the computer subroutines for calculating the slope transition function of (8) and hence the UTD slope diffraction coefficient have been made available to Monopole Research. Finally, one notes that the slope diffracted field allows for the incident and reflected fields to vary rapidly along the directions normal to the edge fixed planes of incidence and reflection, respectively; i.e. along $\hat{n}^i$ and $\hat{n}^r$ as is evident from the normal derivatives given by $\hat{n}^i \cdot \nabla$ and $\hat{n}^r \cdot \nabla$ in (7).

2.1.3 FD-UTD for Surface Diffraction
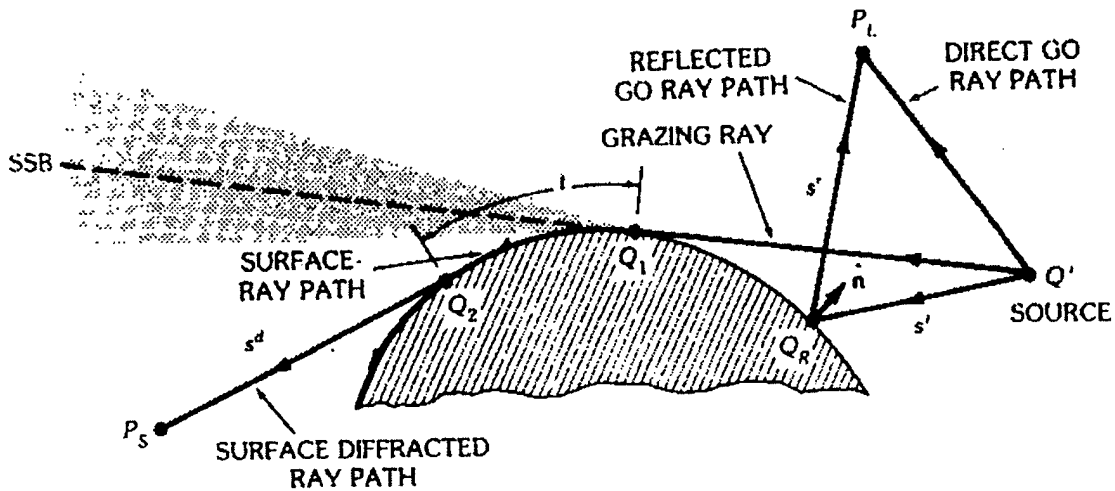
Fig. 5(a) : Diffraction at a Smooth Convex Surface

When an incident ray grazes a smooth perfectly conducting convex surface at Q_l, it launches a surface ray, which propagates along a geodesic path into the shadow region of the convex object as shown in Fig.5 (a) and Fig. 5(b).

12
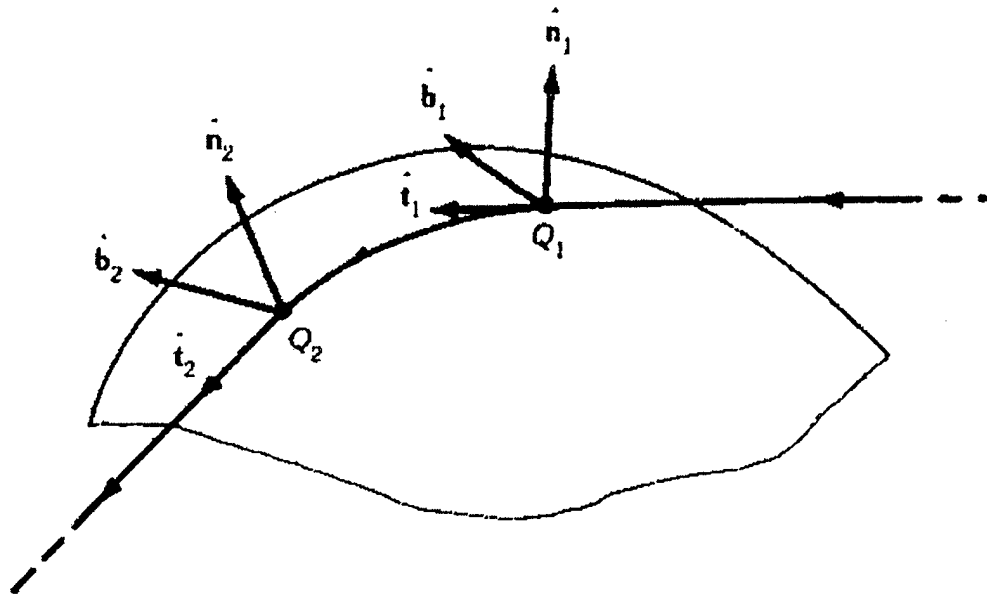
Fig. 5(b) : Unit Vectors fixed in the Surface Diffracted Ray

Furthermore, the field along the ray geodesic path is exponentially attenuated because energy is shed from the surface ray along its forward tangent. This energy, which is shed from the surface ray, travels a surface diffracted ray path to arrive at an observer at P_s in the shadow region of the smooth convex object as shown in Figs. 5(a) and 5(b). The surface diffracted ray arrives at P from the point of surface diffraction on geodesic surface ray at Q_2. The path from point of launching of the surface ray at the point of grazing incidence Q_1 to the point Q_2 is the surface ray path which is a surface geodesic. A surface ray strip and its associated surface diffracted ray tube are depicted in Fig.6 in the general case when an astigmatic ray tube is incident at grazing on a smooth convex surface. If the smooth convex body is a closed, as it usually is in practice, the surface ray can also traverse around the body; hence, it can produce surface diffracted rays which can also reach an observer in the lit region at P_L where the incident ray field is directly visible. In the lit region, the total field at P_L consists of the incident and reflected

13

geometrical optics field as well as surface diffracted ray fields for closed bodies. In the shadow region, the total field at P_s consists of only the surface diffracted ray fields.
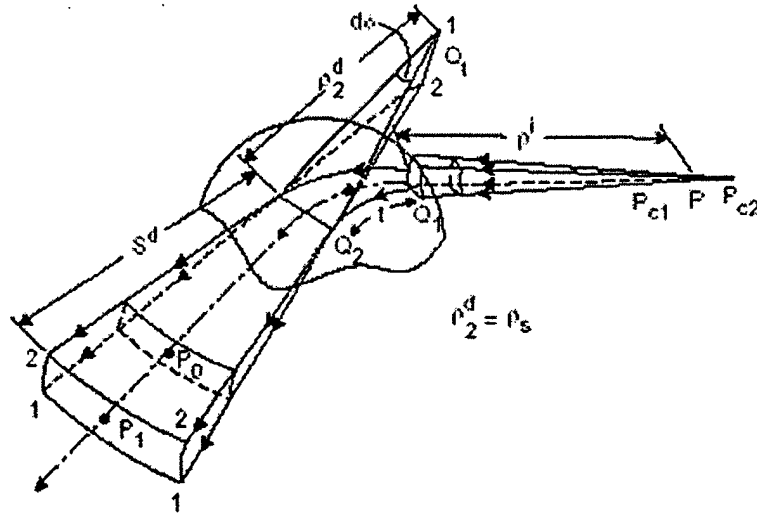
Fig. 6 : Surface-diffracted ray tube. Radius of the incident wavefront where
it grazes the surface at Q_1 is ρ^i

In the smooth convexly curved body, the incident and reflected ray directions merge along grazing incidence to define the surface shadow boundary (SSB). The SSB is an extension of the incident ray past grazing. A boundary layer exists adjacent to SSB; this layer is referred to as the SSB transition region. On the lit side which is outside this transition region, the field consists of ordinary geometrical optics incident and reflected ray fields for a given incident ray field illumination. In addition, one or more surface diffracted ray field contributions can also be present in the lit region as mentioned previously. The latter occur if the surface rays, which continuously shed surface diffracted rays, encircle the body one or more times. Effects of multiple surface ray encirclements may be ignored if the closed convex body is electrically large, because the surface ray field in this case becomes exponentially weak (due to continental shedding of energy) to the point where it can be neglected. On the other hand, the ordinary geometrical optics reflected field vanishes along the SSB; however, there is a diffraction effect present which modifies the reflected field at and near the SSB (i.e. on the lit side of the SSB). Hence, the UTD electric field at a point P_L (see Fig.5 (a)) on the lit side of the SSB is

$$\overline{E}(P_L) \approx \overline{E}^i(P_L) + \overline{E}^{gr}(P_L) + \overline{E}^d(P_L) \tag{10}$$

14

where $\bar{E}^d(P_L)$ results from single or multiple encirclements, and can be ignored if the closed convex body is large as mentioned before. The $\bar{E}^{gr}(P_L) \to \bar{E}^r(P_L)$ in the lit region outside the SSB transition zone, and $\bar{E}^r(P_L)$ is the conventional geometrical optics reflected field. Hence $\bar{E}^{gr}(P_L)$ is the generalized reflected field which contains diffraction separate from that in $\bar{E}^d(P_L)$ due to encirclements. One notes that $\bar{E}^{gr}(P_L)$ is far more significant than $\bar{E}^d(P_L)$ in the lit zone.

At a point P_s on the shadow side of the SSB, the total field is simply the surface diffracted field $\bar{E}^d(P_s)$, i.e.,

$$\bar{E}(P_s) \approx \bar{E}^d(P_s) \tag{11}$$

Additional contributions to $\bar{E}^d(P_s)$ from encircling rays can also be present at P_S; however; their contribution is negligible for large convex bodies.

The fields $\bar{E}^i(P_L)$, $\bar{E}^{gr}(P_L)$ and $\bar{E}^d(P_s)$ indicated in (10) and (11) are given in detail in [11,12]. The form of $\bar{E}^d(P_L)$ is the same as $\bar{E}^d(P_s)$. The general forms of $\bar{E}^{gr}(P_L)$ and $\bar{E}^d(P_s)$ are [11,12] :

$$\bar{E}^{gr}(P_L) \approx \bar{E}^i(Q_R) \cdot \bar{\bar{R}} \ A_r(s^r) \ e^{-jks^r} \tag{12}$$

$$\bar{E}^d(P_s) \approx \bar{E}^i(Q_1) \cdot \bar{\bar{D}} \ A_d(s^d) \ e^{-jks^d} \tag{13}$$

Outside the transition on the lit side region, $\bar{\bar{R}} \to \bar{\bar{R}}$, where $\bar{\bar{R}}$ is the dyadic geometrical optics reflection coefficient. Likewise, outside the transition region on the shadow side, $\bar{\bar{D}}$ reduces to Keller's field description in terms of GTD surface diffraction coefficients at Q_1 and Q_2, respectively together with a complex propagation constant along the geodesic path from Q_1 to Q_2 [13]. Within the transition regions, both, $\bar{\bar{R}}$ and $\bar{\bar{D}}$ in the UTD solution contain an F type transition function as in (9) and a $\tilde{P}_{s,h}$,Fock type transition function, which keep the total field bounded and continuous across the SSB, respectively. From [11,12], one can write $\bar{\bar{D}}$ as

$$\bar{\bar{D}} = \left(\tilde{D}_s \hat{b}_1 \hat{b}_2 + \tilde{D}_h \hat{n}_1 \hat{n}_2 \right) \sqrt{\frac{d\eta(Q_1)}{d\eta(Q_2)}} e^{-jkt} \tag{14}$$

where $\left(\hat{n}_1, \hat{b}_1\right)$ are the normal and binormal unit vectors to the surface ray geodesic at the launch point, Q_1, while $\left(\hat{n}_2, \hat{b}_2\right)$ are the corresponding unit vectors at the point of shedding, Q_2 as in Fig. 5(b). The unit vectors $\left(\hat{t}_1, \hat{t}_2\right)$ are along the forward tangents to the surface ray at at Q_1 and Q_2, respectively. One notes that $\hat{b}_1 = \hat{t}_1 \times \hat{n}_1$. Also, t in (14) is the geodesic surface ray arc length from Q_1 to Q_2. Furthermore, $A_r\left(s^r\right)$ and $A_d\left(s^d\right)$ are the spatial spreading (or divergence) factors associated with the reflected ray (from Q_R to P_L) and with the surface diffracted ray (from Q_2 to P_s). The $d\eta\left(Q_{1,2}\right)$ in (14) represents the width of the surface ray strip at $Q_{1,2}$ as in Fig. 6 and hence the square root in (14) represents the spreading of energy in a surface ray strip along a geodesic ray path. Finally, s_r and s_d are the reflected and surface diffracted ray distances ($\left|\overline{Q_R P_L}\right|$)and ($\left|\overline{Q_2 P_s}\right|$) respectively.

It is noted that the UTD dyadic transition functions in (12) and (13) can be computed via the subroutines that have been made available to Monopole Research.

2.1.4 FD-UTD for the Radiation from a Source on a Smooth Convex Surface

When a source/antenna is placed on a smooth convex surface, which is perfectly conducting, then the near and far field radiated by this source at Q' can be shown to be associated with a direct ray to a point P_L in the lit region (where the source is directly visible), and a surface diffracted ray to a point P_s in the shadow region. These rays are depicted in Figs. 7(a) and 7(b), respectively, for a non closed smooth convex body. If the convex body is closed, as is usually the case in practice, then additional oppositely encircling surface rays can also contribute via surface diffraction to the point P_L. These additional contributions can also be present at P_s. Here, these additional contributions are assumed to be negligible as is true for large convex bodies.
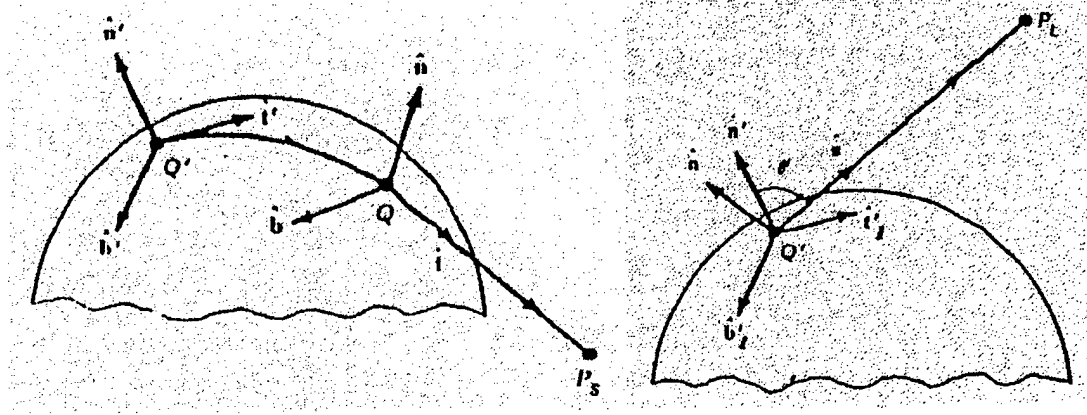
7 (a)   7(b)

Fig. 7 : Radiation by a Source on a Smooth Convex Surface

As shown in [14], the electric fields $d\overline{E}_{m,e}(P_L)$ and $d\overline{E}_{m,e}(Ps)$ radiated by an infinitesimal magnetic (m) or electric (e) current moment $d\overline{p}_{m,e}(Q')$ at Q' can be expressed symbolically as

$$d\overline{E}_{m,e}(P_L) \approx d\overline{p}_{m,e}(Q') \cdot \overline{\overline{T}}^t_{m,e} A_d(s^d) \; e^{-jks^d} \tag{15}$$

and

$$d\overline{E}_{m,e}(P_s) \approx d\overline{p}_{m,e}(Q') \cdot \overline{\overline{T}}_{m,e} A_d(s^d) \sqrt{\frac{d\psi_o}{d\eta(Q)}} \; e^{-jks^d} \tag{16}$$

where $A(s)$ ($= 1/s$) and $A_d(s^d)$ constitute the spreading of the rays along the direct path along s $\left(=\left|\overline{Q'P_L}\right|\right)$, and the surface diffracted path s^d $\left(=\left|\overline{QP_s}\right|\right)$, respectively. One notes that the ray path from at Q' to Q (before it sheds from Q to P_s) is a surface geodesic. Also, the surface ray divergence factor from Q' to Q is given by the square root term in (16); the $d\psi_o$ and $d\eta(Q)$ in (16) are shown in Fig. 8. The dyadic radiation and diffraction functions $\overline{\overline{T}}^t_{m,e}$ and $\overline{\overline{T}}_{m,e}$, respectively, are given in terms of UTD transition functions involving the radiation Fock functions g and $\tilde{g}$ [14,15]. The unit vectors $(\hat{t}',\hat{n}',\hat{b}')$ at Q' and $(\hat{t},\hat{n},\hat{b})$ at Q, respectively, are fixed in the surface diffracted ray as in Fig. 7(a); the $\overline{\overline{T}}_{m,e}$ then shows how a given orientation of $d\overline{p}_{m,e}$ at Q' (i.e. $\hat{t}',\hat{n}'$ or $\hat{b}'$) produces the

17

polarization type ($\hat{n}, \hat{b}$) for $d\overline{E}(P_s)$ at P_s. Likewise, $\overline{\overline{T}}^{\ell}_{m,e}$ indicates how the ($\hat{t}'_\ell, \hat{b}'_\ell$ and $\hat{n}'$)

components of $d\overline{p}_{m,e}(Q')$ at Q' produce the ($\hat{n}, \hat{b}$) polarized fields $d\overline{E}(P_L)$ at P_L. Thus,

$\overline{\overline{T}}^{\ell}_{m,e}$ and $\overline{\overline{T}}_{m,e}$ are the UTD transition or transfer functions (containing the Fock functions $g, \tilde{g}$) that link the source to the fields produced by the source; they also keep the total field continuous as one goes from P_L on the lit side, to P_s on the shadow side of the surface shadow boundary. These UTD dyadic transition functions in (15) and (16) can be computed via the subroutines made available to Monopole Research.
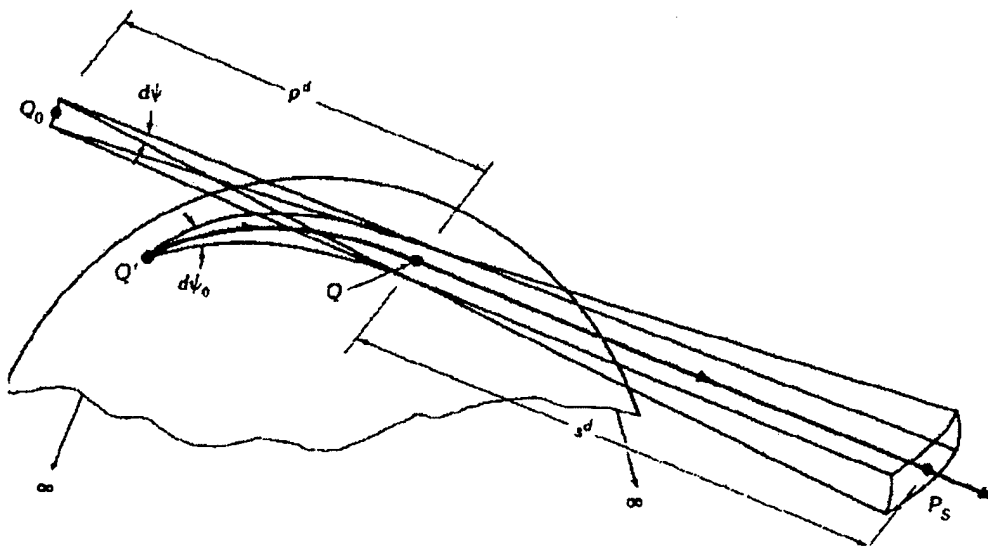
Fig. 8 : Surface Diffracted Ray Tube excited by a Source at Q' on a Smooth Convex PEC Surface

The response $\overline{E}_{m,e}(P_L)$ and $\overline{E}_{m,e}(P_s)$ due to any physical, finitely distributed equivalent magnetic (m) or electric (e) sources can be obtained by integrating $d\overline{E}_{m,e}(P_L)$ and $d\overline{E}_{m,e}(P_s)$ over these sources [14]. Although, the results in (15) and (16) provide the fields radiated by an infinitesimal source on a smooth convex surface, they can also, by the reciprocity theorem, provide the surface charge density (e case) or the surface current density (m case) at Q' which is induced by a wave incident at Q' from a distant source at P_L or P_s, respectively. The latter is of interest in electromagnetic pulse (EMP) and

18

scattering problems, while the solutions in (15) and (16) given for the direct problem are useful for predicting the radiation by conformal antennas and arrays on smooth convex surfaces.

2.1.5 FD-UTD for the Mutual Coupling between Antennas on a Smooth Convex Surface

Fig. 9(a) : Surface ray from Q' to Q
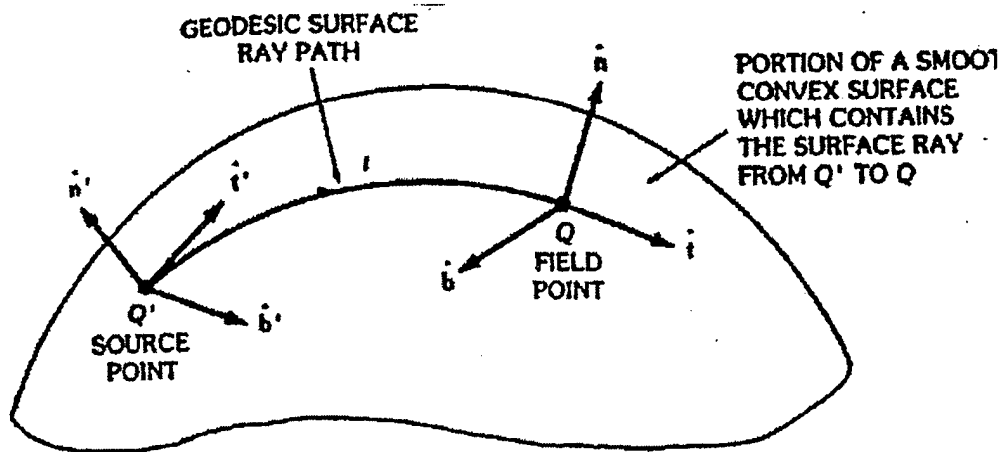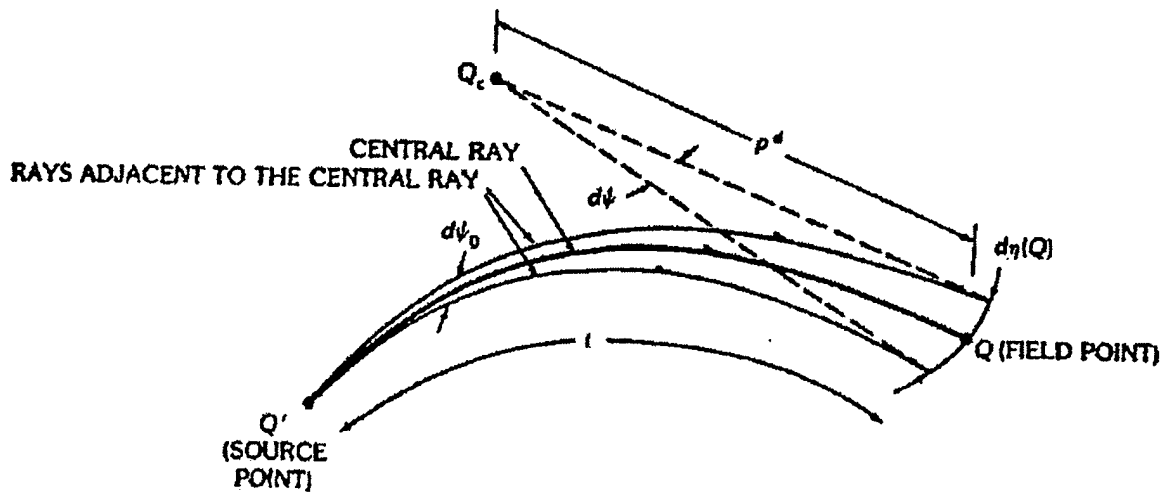
Fig.9(b) : Surface-ray strip (or tube)

The surface ray field at any point Q on a smooth, perfectly conducting convex surface which is produced by a source at Q' on the same surface must again follow a geodesic path connecting Q' to Q. The ray geometry for this problem is sketched in Figs 9(a) and 9(b).

The electric and magnetic surface fields $d\overline{E}_{m,e}$ and $d\overline{H}_{m,e}$ at Q may be expressed via the development in [16] as follows:

$$dE_{e,m}(Q) \approx d\overline{p}_{e,m}(Q') \cdot \overline{\overline{\Gamma}}^e_{e,m} \sqrt{\frac{d\psi_o}{d\eta(Q)}} A(s) \ e^{-jks^d} \qquad (17)$$

and

$$d\overline{H}_{e,m}(Q) \approx d\overline{p}_{e,m}(Q') \cdot \overline{\overline{\Gamma}}^h_{e,m} \sqrt{\frac{d\psi_o}{d\eta(Q)}} A(s) \ e^{-jks^d} \qquad (18)$$

The $d\psi_o$ and $d\eta(Q)$, both of which appear in (17) and (18), respectively, have the same meaning as in (16); these quantities are also depicted in Fig. 8(b). The surface ray field dyadics $\overline{\overline{\Gamma}}^e_{e,m}$ and $\overline{\overline{\Gamma}}^h_{e,m}$ indicate the type of surface field polarization ($\hat{t}, \hat{n}$ or $\hat{b}$), which is produced at Q by any particular component ($\hat{t}', \hat{n}'$ or $\hat{b}'$) of the source $d\overline{p}_{m,e}(Q')$ at Q'. A detailed description of $\overline{\overline{\Gamma}}^e_{e,m}$ and $\overline{\overline{\Gamma}}^h_{e,m}$ are available in [16]. The $A(s) = \frac{1}{\sqrt{s}}$ in (17) and (18), where s is the geodesic arc length from Q' to Q as sketched in Fig 9(a).

The UTD dyadic transfer or transition functions in (17) and (18) contain the surface Fock functions U and V, respectively [16,15]; these UTD transition functions can be computed via the subroutines made available to Monopole Research.

2.1.6 An Application of FD-UTD To Airborne Antenna Pattern Prediction
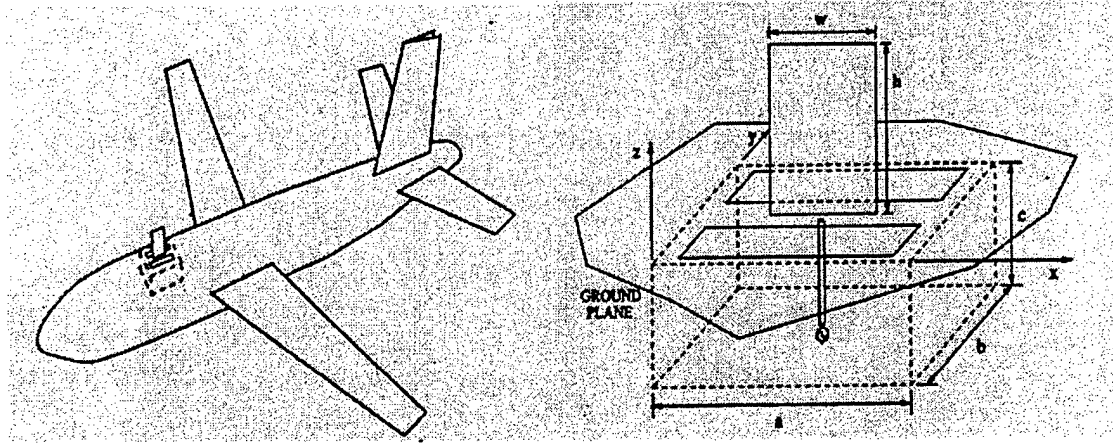
Fig 10 : Slot-Blade Cavity Antenna Geometry

As indicated previously, the FD-UTD has been utilized extensively to analyze the radiation from complex shapes. The FD-UTD results have been tested numerous times with scale model measurements or by other independent numerical approaches where possible. An example analyzed here via the FD-UTD is indicated below to illustrate the versatility of this ray approach. Specifically, a complex cavity backed slot-blade antenna, which is analyzed via the moment method (MM) solution of the governing integral equation is placed on F-16 fighter jet in this example. The pattern of this antenna on F-16 is analyzed via the Ohio State Univ. (OSU) NEWAIR code which is based on the FD-UTD [17]. The antenna geometry, as well as the NEWAIR FD-UTD model of F-16, and the patterns calculated from that code are illustrated in Figs. 10, 11 and 12, respectively. It is important to note that the FD-UTD patterns in Fig.12 have been computed based primarily on the FD-UTD formulas given in item 2.1.1 and item 2.1.4 above.

21
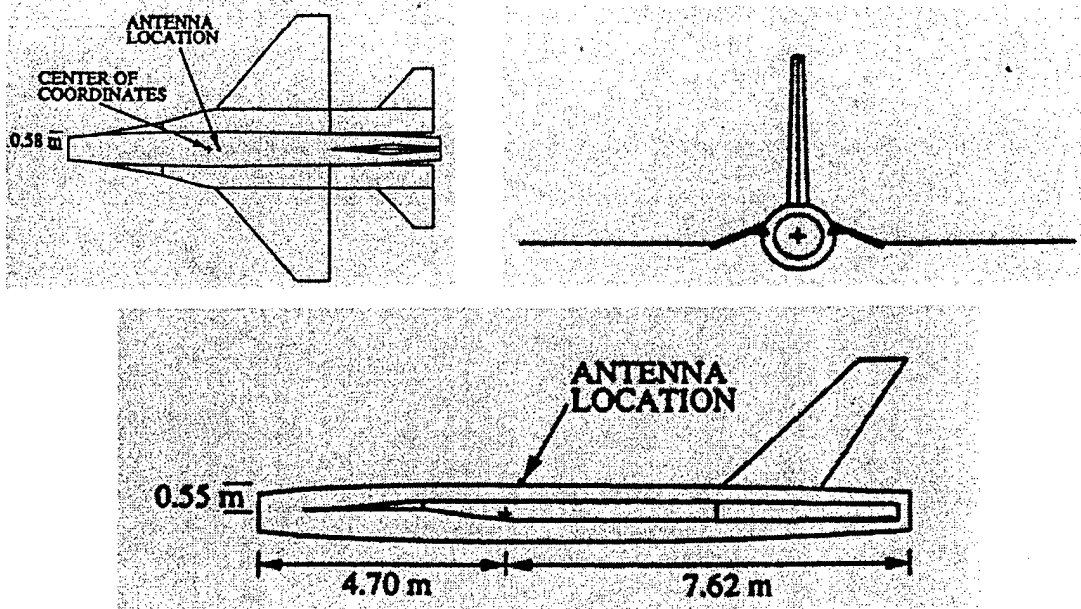
Fig.11 : F-16 Model Based om FD-UTD

It would be of interest, for the reasons mentioned in section 1, to develop a corresponding TD-UTD which would allow one to analyze the radiation /scattering of transient EM waves from complex objects to the same level as the FD-UTD. The recent TD-UTD developments are described next in sections 2.2 and 2.3.
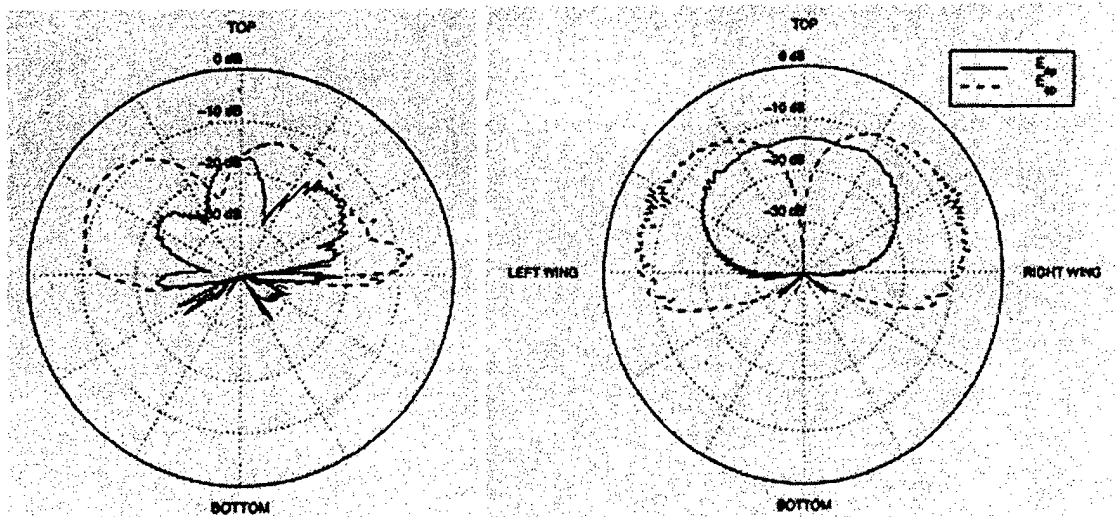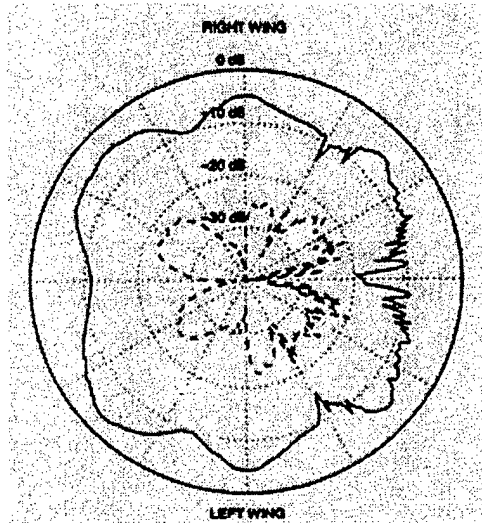
Fig. 12 : FD-UTD Radiation Patterns of the Antenna in Fig. 10 when placed on the aircraft of Fig. 11

2.2 TD-UTD for Edge and Surface Diffraction

The motivation for the development of a TD-UTD to efficiently analyze the transient radiation /scattering from complex objects which are excited by short pulses has been discussed earlier in section 1. The TD-UTD employs the same rays as the FD-UTD and hence retains all of the advantages of the FD-UTD since one constructs a TD-UTD solution from an analytic inversion into the time domain of the corresponding FD-UTD. The TD-UTD solutions which have been developed recently, but prior to the start of the present contract with monopole Research, are summarized below. The particular transform used in the TD-UTD development which converts the FD-UTD into the time domain is the Analytic Time Transform (ATT). The ATT is utilized because it has several advantages for this particular application. Specifically, the ATT is convenient for inverting the FD-UTD fields which may have traversed through ray caustics, and which may exhibit a general elliptic polarization.

The ATT is defined for positive frequencies (i.e., for $\omega > 0$) as follows:

$$\overset{+}{f}(t) = \frac{1}{\pi} \int_0^\infty F(\omega) e^{j\omega t} d\omega \qquad ; \quad \mathrm{Im}\, t > \alpha \quad , \tag{19}$$

where $\overset{+}{f}(t)$ is the ATT of the frequency domain function $F(\omega)$. $\overset{+}{f}(t)$ is analytic for $\mathrm{Im}\, t > \alpha$ with $|F(\omega)| \approx c e^{\alpha\omega}$ as $\omega \to \infty$. The $f(t)$ is obtained from $\overset{+}{f}(t)$ via

23

$$f(t) = \operatorname{Re} \overset{+}{f}(t) \qquad\qquad ; \quad \operatorname{Im} t = 0 \quad , \tag{20}$$

Note that $f(t)$ is the inverse Fourier transform of $F(\omega)$. Also,

$$\overset{+}{f}(t) = f(t) + jHf(t) \qquad\qquad ; \quad \operatorname{Im} t = 0 \quad , \tag{21}$$

in which $Hf(t)$ is the Hilbert transform of $f(t)$.

The analytic delta function is defined as

$$\overset{+}{\delta}(t) = \begin{cases} \dfrac{j}{\pi t} & , \operatorname{Im} t > 0 \\[2mm] \delta(t) + pv \dfrac{j}{\pi t} & , \operatorname{Im} t = 0 \end{cases} \tag{22}$$

where pv signifies the Cauchy principal value when integrating over the function. Hence $\overset{+}{\delta}(t)$ is a distribution for $\operatorname{Im} t = 0$; it may be used as an input or excitation with a time impulsive behaviour for the transient TD-UTD solution that is to be constructed. The TD-UTD response to a $\overset{+}{\delta}(t)$ type excitation is generally easier to obtain; it then allows one to construct the response to any realistic finite bandwidth excitation via an efficient convolution procedure. For example, if a realistic excitation pulse $\overline{E_0^i}(\omega)$ can be represented in the frequency (ω) domain by a sum of handful of exponential functions as

$$\overline{E}_o^i(\omega) = \hat{p} \sum_{n=1}^{N} A_n e^{-\alpha_n \omega} \qquad\qquad , \omega > 0 \tag{23}$$

then

$$\overset{+}{\overline{e}}_o^i(t) = \hat{p} \sum_{n=1}^{N} \frac{A_N}{t + j\alpha_n} \qquad\qquad , \operatorname{Im} t > -\alpha_n \tag{24}$$

Now, if $\overset{+}{\overline{e}}_I(t)$ denotes the TD-UTD response to an analytic delta (impulse) function i.e. to a $\hat{p}\overset{+}{\delta}(t)$ time dependence, then the TD-UTD response, $\overset{+}{e}(t)$ is given via convolution as

$$\overset{+}{\overline{e}}(t) = \frac{1}{2} \sum_{n=1}^{N} \frac{A_N}{t + j\alpha_n} \ast \overset{+}{\overline{e}}_I(t) \tag{25}$$

or

24

$$\overset{+}{e}(t) = \frac{-j}{2\pi}\sum_{n=1}^{N} A_n \int_{-\infty+j\varepsilon}^{\infty+j\varepsilon} \overset{+}{e}_I(t') \frac{1}{t'-t-j\alpha_n} dt' \qquad ; \quad \begin{cases} \varepsilon > 0 \\ \mathrm{Im}\,t > \alpha \end{cases} \qquad (26)$$

Since $\overset{+}{e}_I(t')$ may be assumed to be analytic for $\mathrm{Im}\,t' > \alpha$ and the poles of $\dfrac{A_n}{t+j\alpha_n}$

reside in the same half space, it follows that

$$\overset{+}{e}(t) = \sum_{n=1}^{N} A_n \overline{e}_I(t + j\alpha_n) \qquad (27)$$

As long as $\mathrm{Re}\,\alpha_n > 0$ for all n, the $\overset{+}{e}(t)$ will be analytic on the real time axis ($\mathrm{Im}\,t = 0$) so one can obtain the desired TD-UTD response $\overline{e}(t)$ in a straight forward manner via

$$\overline{e}(t) = \mathrm{Re}\,\overset{+}{e}(t) \qquad ; \quad \mathrm{Im}\,t = 0 \qquad . \qquad (28)$$

Consider a typical waveform shown in Fig. 13 whose frequency (ω) domain behaviour is shown in Fig. 14. The behaviour in Fig.14 can be synthesized with only three terms of the type in (23); consequently, the response in (27) and hence that in (28) can be found by summing (24) over just three terms. The attractive property that allows one to go from (26) to a simple result for the convolution in (27) is another reason to employ the ATT rather than the conventional Fourier or Laplace transforms in the TD-UTD development.

Some TD-UTD results available from the recent past are reviewed next.
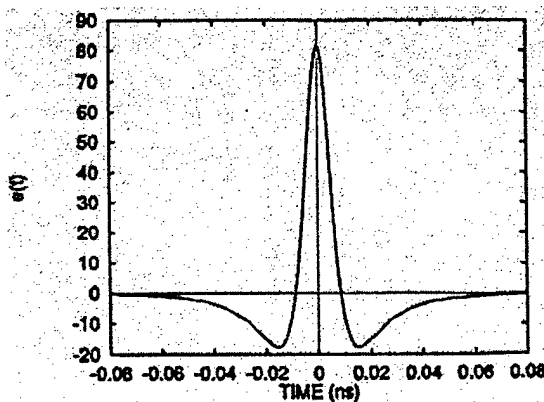
Fig. 13: The waveform in Time Domain   Fig. 14 : Frequency Domain Behaviour
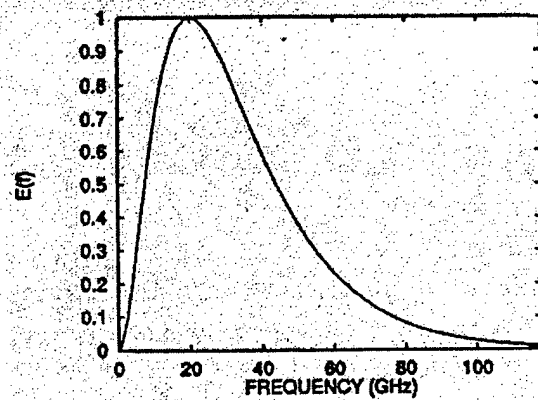
2.2.1 TD-UTD for Edge Diffraction

The geometry for edge diffraction is shown in Fig.1 as before for the FD-UTD case. The TD-UTD field for diffraction by an arbitrary curved conducting wedge can be found by taking the ATT of (1) for a general astigmatic wave illumination. The case of the astigmatic wave illumination in the FD-UTD case leads to a time impulsive $(\overset{+}{\delta})$ astigmatic wave illumination for the corresponding TD-UTD case. Hence, the impulsive response $\overset{+}{\overline{e}_I^d}(t)$ for the wedge diffraction has been obtained from the ATT of (1) for this situation as [6,7]

$$\overset{+}{\overline{e}_I^d}(t) \approx \overline{E}_o^i(Q_E) \cdot \overset{+}{\overline{\overline{d}}}(\tau_d) A(s^d) \tag{29}$$

where

$$\tau_d = t - \frac{s^i}{c} - \frac{s^d}{c} \tag{30}$$

in which s_i and s_d are the distances from O to Q_E (i.e $s^i = |\overline{OQ_E}|$) and Q_E to P (i.e $s^d = |\overline{Q_EP}|$ as before). Also, c = speed of the EM wave in free space which surrounds the wedge. Since the details of the development leading to (29) are available in [,], no further details will be provided here, except to state that the $\overset{+}{\overline{\overline{d}}}(\tau_d)$ of the TD-UTD turns out to be actually simpler than the corresponding $\overline{\overline{D}}$ of (1) for the FD-UTD. Subroutines for computing (29) have been made available to Monopole Research.

2.2.2 TD-UTD for Slope Edge Diffraction

For the case of an incident wave which exhibits a rapid spatial variation at the point of edge diffraction, a slope diffracted field contribution had to be added to (1) as indicated in 2.1.2. The details of the TD-UTD development from the corresponding FD-UTD given in (7) are also available in [6]. However, a paper on this subject has been written on the present contract [18] and it is also included as Appendix 1 of this report for the sake of completeness. Thus, no further details about a TD-UTD for slope edge

diffraction are provided here. The computer subroutines for calculating TD-UTD slope diffracted field have been made available to Monopole Research.

2.2.3 TD-UTD Surface Diffraction

The geometry of this surface diffraction problem is found in Fig. 5 for the corresponding FD-UTD case. The TD-UTD solution for a time impulsive ($\overset{+}{\delta}$) astigmatic wave excitation can be found by taking the ATT of (10)-(13) for the corresponding FD-UTD case of an astigmatic ray optical field illumination of the smooth convex conducting surface as described in [6]. A paper describing this TD-UTD development is in preparation as a part of the present work for Monopole Research [19]. The desired TD-UTD solution is given as

$$\overset{+}{\overline{e}_I}(t) = \begin{cases} \overset{+}{\overline{e}_I^{\,i}}(t) + \overset{+}{\overline{e}_I^{\,gr}}(t) & , \; lit \, side \, of \, SSB \\[2em] \overset{+}{\overline{e}_I^{\,d}}(t) & , \; shadow \, side \, of \, SSB \end{cases} \tag{31}$$

where

$$\overset{+}{\overline{e}_I^{\,i}}(t) = \overline{E_O^i} A_i(s^i) \overset{+}{\delta}\left(t - \frac{s^i}{c}\right) \tag{32}$$

$$\overset{+}{\overline{e}_I^{\,gr}}(t) = \overline{E_O^i} \cdot \overset{+}{\widetilde{\overline{\overline{R}}}} A_r(s^r) A_i(s^i) \tag{33}$$

and

$$\overset{+}{\overline{e}}(t) = \overline{E_O^i} \cdot \overset{+}{\widetilde{\overline{\overline{D}}}} A_d(s^d) A_i(s^i) \tag{34}$$

The $\overset{+}{\widetilde{\overline{\overline{R}}}}$ and $\overset{+}{\widetilde{\overline{\overline{D}}}}$ are the ATT of the transition functions involving the F and $\widetilde{P}_{s,h}$ type integrals in (10)-(13).

As mentioned above, the details concerning the application of the ATT leading to (31)-(34) are available in [6], and will soon appear in [19]. Computer subroutines for calculating (31)-(33) have been made available to Monopole Research.

27

3. Summary of Two New TD-UTD Solutions

The TD-UTD solutions for the radiation from antennas on a smooth convex surface, and the mutual coupling between a pair of antennas on a smooth convex surface, respectively, have been completed under the present contract. These new TD-UTD solutions are developed via the application of the ATT to the general expressions indicated in sections 2.1.4, and 2.1.5, respectively, for the corresponding FD-UTD solutions; these solutions are summarized below together with the some numerical results illustrating their accuracy.

3.1 TD-UTD for the Radiation from a Source on a Smooth Convex Surface

The geometry of the problem in question is the same as that in Fig. 7(a). The FD-UTD for this problem is given separately for the lit and shadow regions as in (15) and (16), respectively.

The ATT of (15) or the more detailed version in [12] yields the TD-UTD solution for the lit side as:

$$d \overset{+}{\overline{E}}_{m,e}(t) = d\overline{p}^o_{m,e} \bullet \overset{=i,\ell}{\overline{T}}_{m,e}\left(t - \frac{s}{c}\right)\frac{1}{s} \tag{35}$$

with

$$\overset{=i,\ell}{\overline{T}}_m(t) = \frac{-1}{4\pi c}\left[\hat{b}'_\ell\hat{n}\overset{+}{A} + \hat{t}'_\ell\hat{b}\overset{+}{B} + \hat{b}'_\ell\hat{b}\overset{+}{C} + \hat{t}'_\ell\hat{n}\overset{+}{D}\right] \tag{36}$$

$$\overset{=i,\ell}{\overline{T}}_e(t) = \frac{-Z_0}{4\pi c}\left[\hat{n}'_\ell\hat{n}\overset{+}{M} + \hat{t}'_\ell\hat{n}\overset{+}{N}\right] \tag{37}$$

where   .

$$\overset{+}{A} = \overset{+}{H}_\ell + T_0^2\overset{+}{\Gamma}\cos\theta_i \tag{38}$$

$$\overset{+}{B} = \overset{+}{S}_\ell - T_0^2\overset{+}{\Gamma}\cos^2\theta_i \tag{39}$$

$$\overset{+}{C} = T_0\overset{+}{\Gamma} \tag{40}$$

$$\overset{+}{D} = T_0\overset{+}{\Gamma}\cos\theta_i \tag{41}$$

28

$$\overset{+}{M} = \sin\theta_i \left[\overset{+}{H}_\ell + T_0^2 \overset{+}{\Gamma} \cos\theta_i \right] \tag{42}$$

$$\overset{+}{N} = \sin\theta_i T_0 \overset{+}{\Gamma} \tag{43}$$

with

$$\overset{+}{\Gamma} = \frac{\overset{+}{S}_\ell - \overset{+}{H}_\ell \cos\theta_i}{\left[1 + T_0^2 \cos\theta_i\right]} \tag{44}$$

and

$$\overset{+}{H}_\ell(\Xi_\ell, t) = ATT\left[H^\ell(\omega, \xi_\ell)\right] \tag{45}$$

$$\overset{+}{S}_\ell(\Xi_\ell, t, M_\ell) = ATT\left[S^\ell(\omega, \xi_\ell, m_\ell)\right] \tag{46}$$

The parameters in the lit region are given by

$$M_\ell(\bullet) = \frac{M(\bullet)}{\left[1 + T_0^2 \cos^2\theta_i\right]^{1/2}} \tag{47}$$

$$\Xi_\ell = -M_\ell(\bullet)\cos\theta_i \tag{48}$$

One can also take the ATT of (16) the more detailed version in [12] to obtain the TD-UTD solution for the shadow side as:

$$d\overset{+}{E}_{m,e}(t) = d\overline{p}^o_{m,e} \bullet \overset{=\ell}{T}_{m,e} \left(t - \frac{s_\ell}{c} - \frac{s}{c}\right)\sqrt{\frac{\rho_c}{s(\rho_c + s)}} \tag{49}$$

with

$$\overset{=\ell}{T}_m = \frac{-1}{4\pi c} \left[\hat{b}'\hat{n}T_1(Q')\overset{+}{H} + \hat{t}'\hat{b}T_2(Q')\overset{+}{S} + \hat{b}'\hat{b}T_3(Q')\overset{+}{S} + \hat{t}'\hat{n}T_4(Q')\overset{+}{H}\right]\sqrt{\frac{d\psi_0}{d\eta(Q)}}\left[\frac{\rho_g(Q)}{\rho_g(Q')}\right]^{1/6} \tag{50}$$

and

$$\overset{=\ell}{T}_e = \frac{-Z_0}{4\pi c} \left[\hat{n}'\hat{n}T_5(Q')\overset{+}{H} + \hat{n}'\hat{b}T_6(Q')\overset{+}{S}\right]\sqrt{\frac{d\psi_0}{d\eta(Q)}}\left[\frac{\rho_g(Q)}{\rho_g(Q')}\right]^{1/6} \tag{51}$$

where

$$\overset{+}{H}(\Xi, t) = ATT\left[H(\omega, \xi)\right] \tag{52}$$

$$\overset{+}{S}(\Xi, t, M) = ATT\left[S(\omega, \xi, m)\right] \tag{53}$$

and

$$M(\bullet) = \left(\frac{\rho_g(\bullet)}{2c}\right)^{1/3}$$ (54)

$$\Xi = \int \frac{M(\ell')}{\rho_g(\ell')} d\ell'$$ (55)

The T_O in the above equations is referred to as the torsion factor [12] which characterizes torsional surface rays.

Algorithms have been developed to calculate the ATT of the relevant radiation Fock functions g and $\tilde{g}$ which appear in the above TD-UTD solutions. These subroutines are presently not written in a user friendly form. It is planned to make these subroutines user friendly in the future phases of this study. The details of this new TD-UTD solution will be submitted for publication soon [20]. It is noted that the above TD-UTD solutions have been obtained for an excitation $\bar{J}$ or $\bar{M}$ which is $d\bar{p}_{e,m}\delta(\bar{r}-\bar{r}')U(t-t')$ where U is a step function, and $\bar{J}$ or $\bar{M}$ are the source current densities at Q'. The fields radiated by a time impulsive source at Q' may be found by differentiating the step response which is more easily obtained first.

Some numerical results are illustrated in Figs. 15-20 for a source at Q' on a circular cylinder, where the transient pulse excitation at Q' is the same as in Fig. 13; The results for this pulsed excitation are found via an ATT based, essentially closed form, convolution as discussed at the beginning of section 2.2. The circular cylinder geometry is chosen because an exact frequency domain eigenfunction solution can be constructed for this case and transformed into the time domain for comparison. The results in the far zone at a given angle ϕ are shown for both $\hat{z}$ (axial) directed as well as $\hat{\phi}$ (circumferentially directed) magnetic current sources at ($x = a$, $y = 0$, $z = 0$) where a is the radius of the cylinder. Here, $a = 1$ meter. The agreement between the TD-UTD and the reference solution (referred here simply as eigen solution) is very good.

$$d\overline{p}_m(t) = \hat{z}dp_m(t) \qquad\qquad \overline{E} = \hat{\phi}E_\phi(\phi = 35°)$$
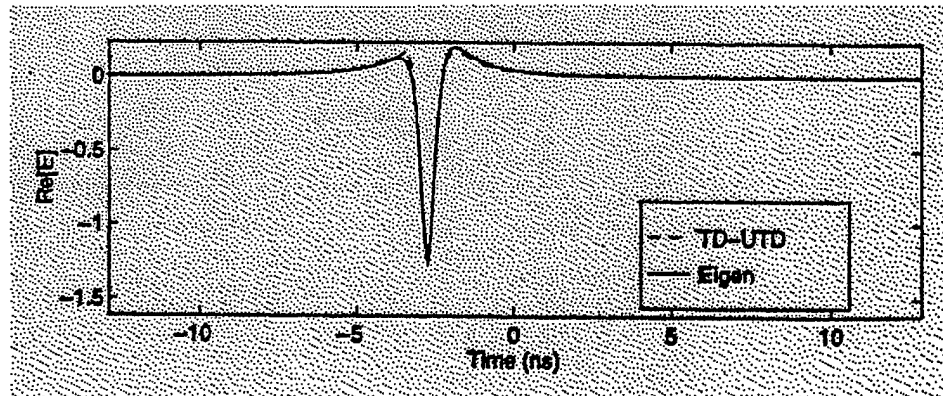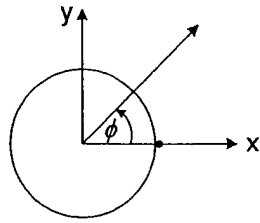
Fig. 15: TD-UTD Radiation from a Source on a Circular Cylinder, which is evaluated in the far zone in the direction ϕ.
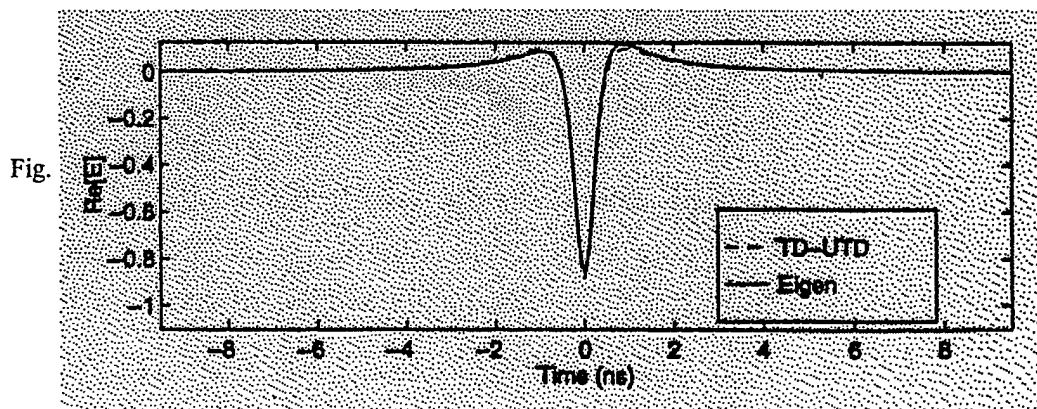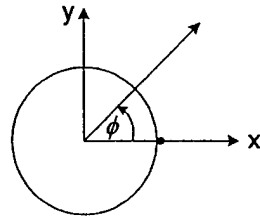
$$d\overline{p}_m(t) = \hat{z}dp_m(t) \qquad \overline{E} = \hat{\phi}E_\phi(\phi = 90°)$$

Fig. 16: TD-UTD Radiation from a Source on a Circular Cylinder, which is evaluated in the far zone in the direction ϕ.

31

$$d\overline{p}_m(t) = \hat{z}dp_m(t) \qquad \overline{E} = \hat{\phi}E_\phi(\phi = 135°)$$
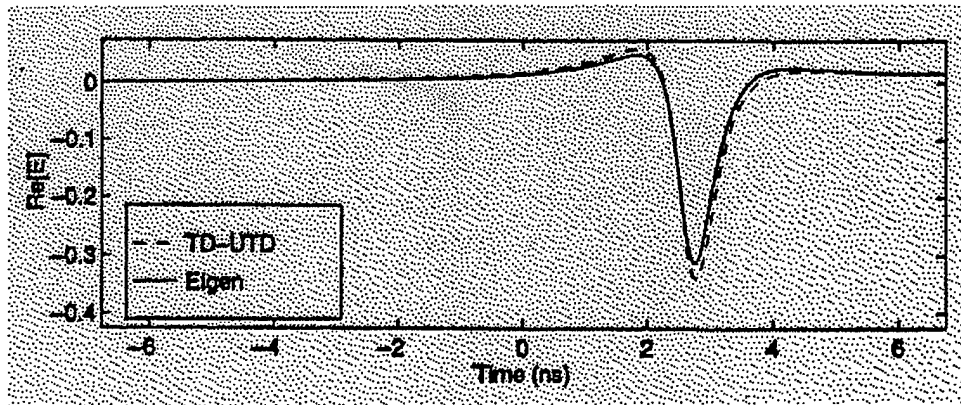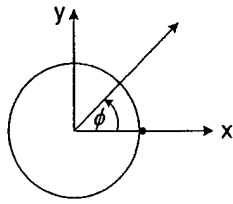
Fig. 17: TD-UTD Radiation from a Source on a Circular Cylinder, which is evaluated in the far zone in the direction φ.
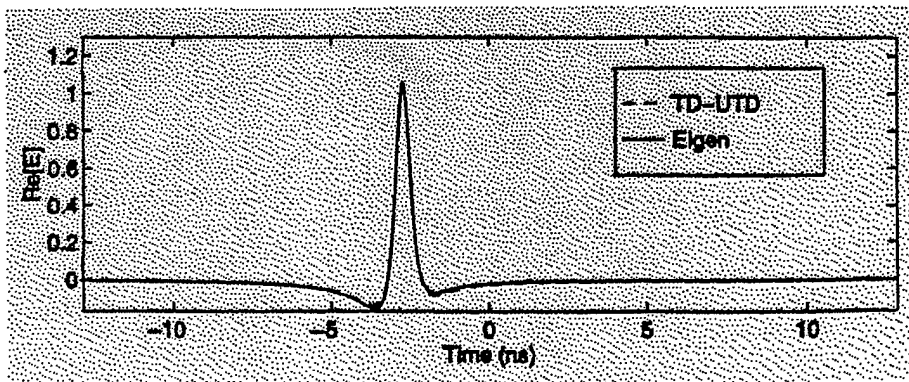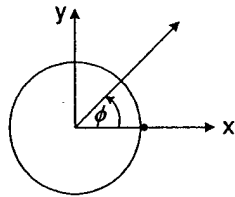
$$d\overline{p}_m(t) = \hat{\phi}dp_m(t) \qquad \overline{E} = \hat{\phi}E_\phi(\phi = 35°)$$

Fig. 18: TD-UTD Radiation from a Source on a Circular Cylinder, which is evaluated in the far zone in the direction φ.

32

$$dp_m(t) = \hat{\phi} dp_m(t)$$

$$\overline{E} = \hat{\phi} E_\phi (\phi = 90°)$$
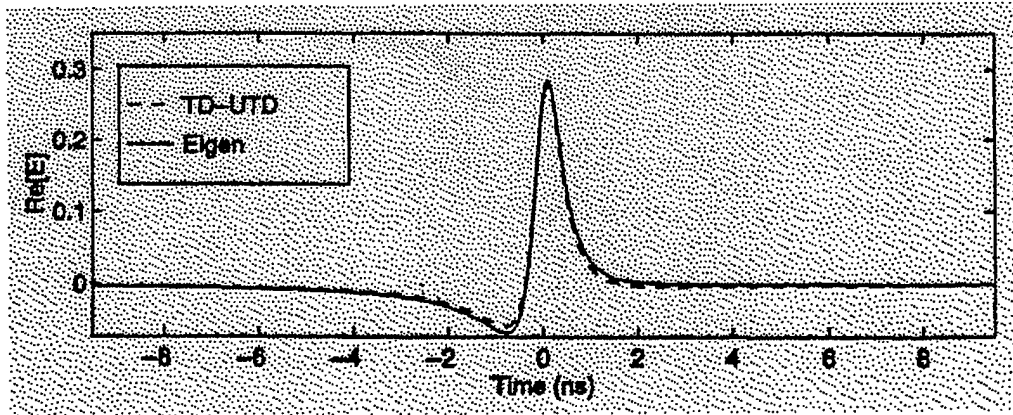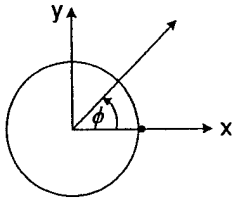
Fig. 19: TD-UTD Radiation from a Source on a Circular Cylinder, which is evaluated in the far zone in the direction φ.

$$dp_m(t) = \hat{\phi} dp_m(t)$$

$$\overline{E} = \hat{\phi} E_\phi (\phi = 135°)$$
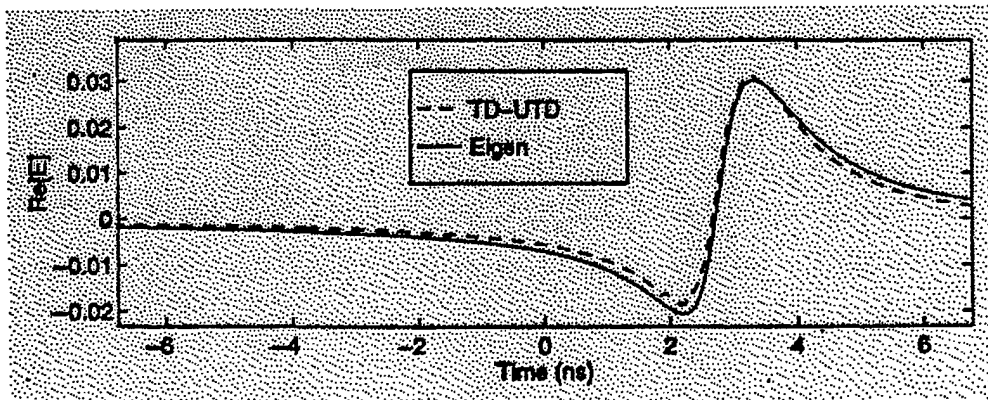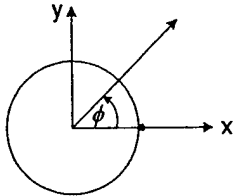
Fig. 20: TD-UTD Radiation from a Source on a Circular Cylinder, which is evaluated in the far zone in the direction φ.

33

$$d \overset{+}{\vec{H}}_m(t) = \frac{-1}{4\pi c} d\overline{p}_e^o \bullet \left\{ 2Z_0 \left(\hat{n}'\hat{n} \left[\overset{+}{\tilde{V}}_0 + \left(\frac{c}{s} \right) \overset{+}{\tilde{V}}_1 + \left(\frac{c}{s} \right)^2 \left(\Lambda_s \overset{+}{\tilde{V}}_2 + \Lambda_c \overset{+}{\tilde{U}}_2 \right) \right. \right.$$

$$\left. \left. \left. - \tilde{T}_0^2 \left(\frac{c}{s} \right) \left(\overset{+}{\tilde{U}}_1 - \overset{+}{\tilde{V}}_1 \right) \right] \right) \right\} \frac{D}{s} \overset{+}{\delta} \left(t - \frac{s}{c} \right) \tag{59}$$

where

$$\overset{+}{\tilde{U}}_m \equiv ATT \left\{ \frac{\tilde{U}(\varepsilon)}{(j\omega)^m} \right\} \tag{60}$$

$$\overset{+}{\tilde{V}}_m \equiv ATT \left\{ \frac{\tilde{V}(\varepsilon)}{(j\omega)^m} \right\} \tag{61}$$

The convolution with $\overset{+}{\delta}\left(t - \frac{s}{c} \right)$ in the above formulas will simply cause a time delay due to surface ray propagation along the geodesic path length s from Q' to Q.

Algorithms have been developed to calculate the ATT of the relevant surface Fock functions $\overset{+}{\tilde{U}}$ and $\overset{+}{\tilde{V}}$ which appear in the above TD-UTD solution; however, they are not presently available in a user friendly form but they will be made available in the future phases of this study. The details of this TD-UTD solution will be submitted for publication soon [21]. Some numerical results are shown in Figs. 21-22 for a source at Q' (x = a, y = 0, z = 0) on a circular cylinder where the source excited by a transient pulse which is the same as in Fig. 13. The circular cylinder is chosen because an exact solution for this case can be obtained as a reference solution for comparison just as in the previous radiation problem case. These results in Figs. 21-22 are obtained via an ATT based convolution of the pulse with a step or impulse response, and the TD-UTD based results are compared with the corresponding exact eigen function based frequency domain results which have been converted into the time domain. The results indicate the surface fields at a given location Q (specified by the angle ϕ). The agreement between the TD-UTD and eigen function based results is very good.

35

$$d\overline{p}_m(t) = \hat{z}dp_m(t) \qquad \overline{E} = \hat{\rho}E_\rho(\phi = 90^\circ)$$
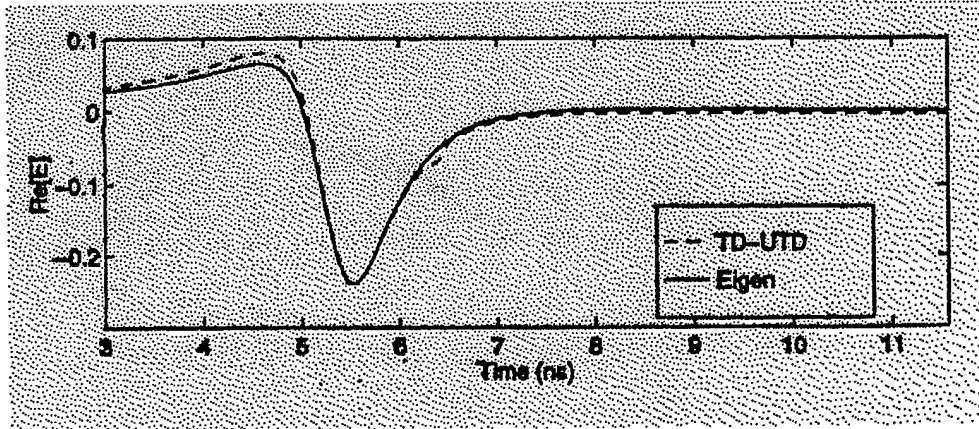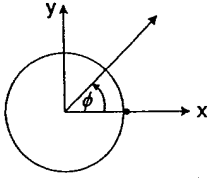
Fig. 21: TD-UTD Surface Field at Q ($\rho = a$, ϕ,z = 0) on a circular cylinder due to a source

at Q' (x = a, y = 0, z = 0)

$$d\overline{p}_m(t) = \hat{\phi}dp_m(t) \qquad \overline{E} = \hat{\rho}E_\rho(\phi = 175^\circ)$$
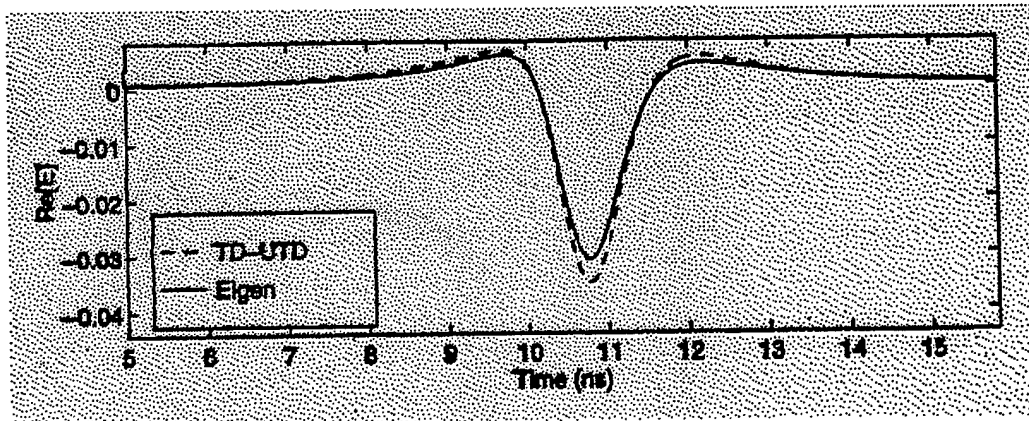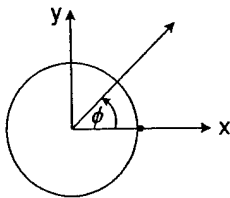
Fig. 22: TD-UTD Surface Field at Q ($\rho = a$, ϕ,z = 0) on a circular cylinder due to a source

at Q' (x = a, y = 0, z = 0)

4 Discussion

A set of five FD-UTD solutions is briefly reviewed in this report; these have been chosen to be initially incorporated into the WE algorithm which is being developed by Monopole Research. The subroutines for computing the FD-UTD transition functions and hence the diffraction functions have been made available to Monopole Research. The corresponding five TD-UTD solutions are also briefly discussed. These five solutions in each, the FD-UTD, and also the corresponding TD-UTD representations, involve the diffraction at an arbitrary curved wedge, the slope diffraction at an arbitrary curved wedge, the surface diffraction by a smooth convex surface, the radiation by a source on a smooth convex surface, and the mutual coupling between antennas on a smooth convex surface, respectively. It is noted that the latter two constitute new solutions in the TD-UTD case which have been completed under this contract. These FD-UTD and corresponding TD-UTD solutions when implemented within the WE algorithm can efficiently analyze the radiation/scattering /coupling of waves in complex structures. Hence, these solutions are very basic and useful in the analysis of scattering, radiation and EMC/EMP problems of practical interest. Additional important FD-UTD results are planned to be included within the WE algorithm in the future phases of this study to make the WE algorithm more versatile in applications to realistic problems; the corresponding TD-UTD solutions will also be developed in the future phases.

5 References

[1] R. G. Kouyoumjian and P. H. Pathak, "A uniform geometrical theory of diffraction for an edge in a perfectly conducting surface," Proc. IEEE, vol. 62, pp. 1448-1461, Nov. 1974.

[2] P. H. Pathak, "Techniques for high frequency problems," in Antenna Handbook, Theory Application and Design, Y. T. Lo and S. W. Lee, Eds. New York: Van Nostrand Reinhold, 1988.

[3] P. H. Pathak, (invited paper). "High frequency techniques for antenna analysis," Proc. IEEE, vol. 80, no.1, pp. 44-65, Jan. 1992.

[4] E. Bleszynski, M. Bleszynski and T. Jaroszewicz, "Development of Wavefront Evaluation Methods for High Frequency Electromagnetic Scattering," paper in DRAFT form, 2002.

[5] J. B. Keller, "Geometrical theory of diffraction," J. Opt. Soc. Amer., vol. 52, pp. 116-130, 1962.

[6] P. R. Rousseau, " Time domain version of the geometrical theory of diffraction," Ph.D. Dissertation, Dept. of Electrical Engineering, The Ohio State Univ., 1995.

[7] P. Rousseau and P. H. Pathak, "Time domain uniform geometrical theory of diffraction (TD-UTD) for a curved wedge," IEEE Trans. Antennas Propagat., vol. 43, no. 12, pp. 1375-1382, Dec. 1995.

[8] E. Beltrami and M. Wohlers, Distributions and the Boundary Values of Analytic Functions, Academic Press, 1966

[9] E. Heyman and L. Felsen, "Weakly Dispersive Spectral Theory of Transients (STT), Part 1," IEEE Trans. AP-35, pp. 80-86, Jan. 1987.

[10] W. D. Burnside and R. J. Marhefka, "Antennas on Aircraft, Ships, or any Large Complex Environment," in Antenna Handbook, Theory Application and Design, Y. T. Lo and S. W. Lee, Eds. , New York: Van Nostrand Reinhold, 1988.

[11] P. H. Pathak, " An asymptotic result for the scattering of a plane wave by smooth convex cylinder," Radio Sci., vol. 14, no. 3, pp. 419-435, May-June 1979.

[12] P. H. Pathak, W. D. Burnside, and R. J. Marhefka, "A uniform UTD analysis of the diffraction of electromagnetic waves by a smooth convex surface," IEEE Trans. Antennas Propagat. Vol. AP-28, pp.609-622, Sept. 1980.

[13] B. R. Levy and J. B. Keller, "Diffraction by a smooth object," Comm. Pure Appl. Math., vol. 12, pp. 159-209, Feb. 1959.

[14] P. H. Pathak, N. Wang, W. D. Burnside and R. G. Kouyumjian, "A uniform GTD solution for the radiation from sources on convex surface," IEEE Trans. Antennas Propagat., vol. AP-29, pp. 609-621, July 1981.

[15] N. A. Logan and K. S. Yee, "A mathematical model for diffraction by convex surfaces," in Electromagnetic Waves, R. Langer, Ed., Madison, WI: Univ. Wisconsin Press, 1962.

[16] P. H. Pathak and N. Wang, "Ray analysis of mutual coupling between antennas on a convex surface," IEEE Trans. Propagat., vol. AP-29, Nov. 1981.

[17] J. J. Kim and W. D. Burnside, "Simulation and analysis of antennas radiating in a complex environment," IEEE Trans. Antennas Propagat., vol. AP-34, pp. 554-562, Apr. 1986.

[18] P. R. Rousseau and P. H. Pathak, "A Time Domain Uniform Geometrical Theory of Slope Diffraction for a Curved Wedge," (Invited paper) Turk. J. Elec. Engin., vol. 10, no. 2, pp. 385-398, 2002 (issue commemorating the 75th birthday of Prof. L. Felsen)

[19] P. R. Rousseau, P. H. Pathak and H.-T. Chou, "A TD-UTD for Diffraction by a Perfectly Conducting, Arbitrary Smooth Convex Surface," to be submitted to IEEE Trans. AP.

[20] H.-T. Chou, P. H. Pathak and P. R. Rousseau, "A TD-UTD for the Transient Radiation by Pulsed Antennas on a Perfectly Conducting, Arbitrary Smooth Convex Surface," to be submitted to IEEE Trans. AP.

[21] H.-T. Chou, P. H. Pathak and P. R. Rousseau, "A TD-UTD for Transient Mutual Coupling between Pulsed Antennas on a Perfectly Conducting, Arbitrary Smooth Convex Surface," to be submitted to IEEE Trans. AP.